Fabrication of Graphene-based Nanocomposite Membranes for Treatment of Process-affected Water

By

Amin Karkooti

A thesis submitted in partial fulfillment of the requirements for the degree of

Doctor of Philosophy

in

Chemical Engineering

Department of Chemical and Materials Engineering

University of Alberta

Abstract

Membrane separation processes are extensively used for separation of solutes such as ions, colloids, macromolecules, and organic matter from water. Among various membrane technologies, ultrafiltration (UF) and nanofiltration (NF) are progressively being employed for elimination of organic matter and macromolecules for wastewater treatment in a single or multiple filtration stage. Fouling is a commonly problematic phenomenon that negatively affects permeate flux, membrane lifespan, and energy consumption in membrane processes. However, fouling on membrane can be reduced by modifying membrane surface properties. In the present research, we fabricated and characterized high-performance nanocomposite membranes by incorporation of graphene-based nanomaterials to a polymeric membrane to enhance its antifouling properties. First different quantities of graphene oxide (GO) derivatives were added to the casting solution and nanocomposite membranes were prepared via non-solvent induced phase separation (NIPS) method. The GO derivatives employed have different shapes and oxidation states with the potential to increase permeation flux and fouling resistance properties of the membrane through controlled pore size, surface charge, and hydrophilicity of the surface. The results revealed that all graphene-based nanocomposite membranes in low quantities showed better permeation and contaminant rejection compared to unmodified PES membrane. In the second stage of the research, extended DLVO (XDLVO) analysis, flux recovery ratio (FRR), and QCM-D were employed to characterize the adsorption behavior of organic foulant on three fabricated mixed-matrix UF membranes. In the third part of this research, we fabricated electro-conductive membranes by depositing a thin layer of polyaniline (PANI)-reduced graphene oxide (rGO) on a polyethersulfone (PES) support. The results showed that the application of an external electric field reduced the organic fouling in both cathode and anode setting.

Keywords: Graphene oxide, Graphene nanoribbon, nanocomposite membranes, oil sands, SAGD, produced water treatment, phase inversion, Extended DLVO, QCM-D, electro-conductive membrane, rGO-PANI nanocomposite

Dedicated to my parents,

Maryam and Fereidoun

For their endless love and support.

I always Love you.

Acknowledgment

I am using this opportunity to express my profound gratitude to my supervisors, Dr. Mohtada Sadrzadeh and Dr. Neda Nazemifard. They have kindly supported me and guided me throughout the period of this work. I am also thankful to my committee member, Dr. Qi Liu for his guidance.

I am really fortunate to have really good colleagues and friends in the Advanced Water Research Laboratory (AWRL) and the University of Alberta. Special thanks to Dr. Masoud Rastgar for being a great assistance during the experimental steps of this work. I would also acknowledge my other friends: Dr. Hadi Nazaripoor, Dr. Hamidreza Sohrabi, Pooria Karami, Farhad Ismail, Dr. Behnam Khorshidi, Ali Mohammadtabar, Simin Shabani, Dr. Ishita Biswas, Dr. Hassan Hosseini, Asad Asad, Laleh Shamaei, Zayed Almansoori, Adham Riad, Farshad Mohammadtabar, Dr. Nandini Debnath, Dr. Ayda Razi, Debanik Bhattacharjee, Sadaf Noamani, Nusrat Hellali, Sadegh Aghapour, Dr. Parmiss Mojir Shaibani, and Dr. Rouholluh Shokri; they were helping me at numerous occasions and making my research experience and living in Edmonton most enjoyable. My special thanks to Lily Laser for her energetic and kind supports during these years. In addition, I am very grateful to Ni Yang for her continuous lab assistance.

Also, I appreciate the financial support from Canada's Oil Sands Innovation Alliance (COSIA), Suncor Energy Company, and Devon Energy Company during my program.

Last but not least, my deepest love and gratitude goes to my family members. They were always supportive and were encouraging me to continue my education. Undoubtedly, without their help, the fulfillment of this study was impossible.

Contents

List of Figures

List of Tables

Chapter 1

Introduction

1 Introduction

1.1 Water scarcity

Over the last century, the world witnessed rapid industrial development and high growth in world's population. Such quick growth imposed great pressure on water resources. In addition, climate change, the pollution of the existing freshwater, and overdrawing of surface and groundwater resources has turned the issue into a water crisis. Water crises are being mentioned every year in Global Risks Report by World Economic Forum as one of the leading threats to the environmental, economic, and social success of most countries in Africa, the middle east, and Asia [1]. So to deal with high demand for water and to have sustainable growth, the management of water resources and the treatment of polluted water are of high-priority. The improved water usage efficiency has accelerated efforts toward improving the current treatment processes and creating new techniques for water treatment that enable meeting the growing demand for freshwater in the future.

Although Canada has one-fifth of the world's freshwater (according to the Canadian Geographic Atlas), there are still concerns associated with water management and sustainability. The oil sands industry in Alberta is an example which needs serious enhancement in water management as it uses roughly 0.2 to 0.3 barrel of freshwater per barrel of bitumen produced in steam-assisted gravity drainage (SAGD) operation. SAGD is an in-situ heavy oil extraction method, which is extensively used for bitumen production in Alberta, Canada. In this process, steam is injected into the oil-bearing formation through a horizontal well to warm up the bituminous material and lower its viscosity to allow flows down by gravity toward the production well. The position of production well is underneath the injection well. A mixture of bitumen and steam condensate water eventually is pumped to the surface where the bitumen and oil-contaminated water is separated. The produced water in this method cannot be released into freshwater streams due to high concentration of organic matter and solid particles; it must be stored in tailings ponds. Therefore, the sustainability of the Alberta oil sands industry necessitates the recycling of process-affected water to decrease environmental impact by reducing the volume of freshwater consumption and waste generated for bitumen production.

In a typical SAGD surface treatment plant (Figure 1.1), at first, the oil-contaminated water is processed in a series of gravity separation vessels to separate the accompanied gases, the bitumen and water. Next, the de-oiled produced water combines with make-up water, as well as recycled boiler blow-down (BBD) stream. The mixture is then directed to a warm lime softener (WLS) vessel to remove silica [2]. Afterward, the de-oiled produced water goes through a conventional water treatment process consists of ion exchanger (IX) and warm lime softener (WLS) to remove silica and divalent ions such as Ca^{+2} and Mg^{+2}. Afterward, the treated water, so-called boiler feed water (BFW), is sent to steam generators. The most steam generators in SAGD are once-through steam generator (OTSG), which can endure relatively high amounts of organic matter and dissolved solids. The OTSG typically produce low-quality steam (75-80%) and resulting in a large volume of BBD. The generated steam is injected into well for further bitumen production. A portion of the BBD is recycled back to the WLS and the rest is sent to disposal.

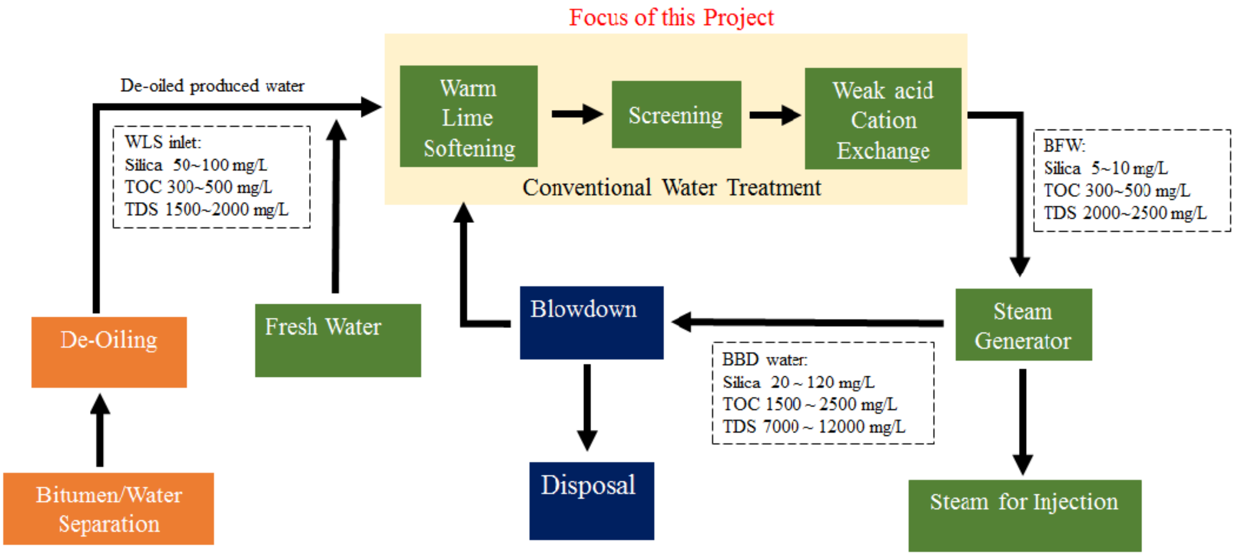

Figure 1.1. Process flow diagram of a SAGD process

The common warm lime softening-weak acid cation exchange (WLS-IX) treatment is not able to completely eliminate the dissolved organic matter (DOM), and only eliminate part of the dissolved silica, therefore a large amount of DOM and TDS remains in the OTSG feed water. Consequently, remaining DOM and TDS cause many operational complications because of formation of fouling and scaling of on the equipment and the pipeline surfaces [3,4]. Therefore, the output BFW from WLS unit requires careful management to reduce fouling formation. In addition, in order to get higher quality steam or reduce the amount of disposal water other types of evaporators should be used. However, energy consumption in evaporators is high and chemical cleaning for maintenance is costly. Consequently, the cost associated with higher-quality steam and lower volume of BBD would be higher in available conventional methods. In view of the above, the oil sands industry is considering alternatives for the current WLS-IX water treatment process. The membrane processes are able to separate almost all silica and divalent ions and retain more than 90% of TDS and DOM in a single or multiple stages while consuming less energy than if desalination evaporators were used.

1.3 Membrane technology for wastewater treatment

Nowadays, considerable number of studies are in progress to improve oil sands water treatment processes focusing on recycling larger amount of water and lower energy usage related to these processes. Membrane separation processes are emerging technologies for oil sands produced water purification owning to their advantages over conventional processes such as lime softening, ion exchange, distillation, and evaporation that includes high filtrate quality, lower operating expenses, and compact design [5]. In addition, membrane separation processes have smaller environmental footprints and require less energy comparing to some of the traditional processes. The required driving force for the filtration in a membrane process can be classified as pressure, external electric field, concentration gradient, and temperature. Among membrane processes, pressure-driven membrane processes are extensively applied for the treatment of the liquids from dissolved/dispersed contaminations. Nowadays, industrial water treatment processes use either porous microfiltration (MF)/ultrafiltration (UF) or dense nanofiltration (NF)/and reverse osmosis (RO) membranes depending on the size of solutes required to be rejected. The MF membranes possess an average pore size in the range of 0.05 μm to 10 μm and can retain large particulate and colloidal, organic matter. Typical pore diameters in the top-layer of a UF membrane are generally in the ranges of 100 nm to 10 μm and are extensively used to eliminate bacteria, organic molecules, and macromolecules such as proteins. NF membranes have an average pore size in the range of 1 to 10 nm. These membranes are typically used for water softening or separating divalent ions from wastewater. Lastly, the RO membrane possesses a pore size of less than 1 nm and is considered the densest membranes [6]. The RO membranes are primarily implemented for separating monovalent ions to produce high-quality drinking water from seawater.

Another classification of membranes is based on their internal structure. Membranes are divided into symmetric and asymmetric. Symmetric membranes have the same pore size distribution across the cross-section of the membrane. On the other hand, asymmetric membranes, have a denser layer on the top with a thickness of less than 500 nm, usually referred to as a skin layer and a more porous sublayer structure underneath with a thickness about 200 µm. Asymmetric membranes usually yield a higher permeation rate compared to the symmetric membrane of comparable thickness [6]. The permeation rate of a membrane is inversely related to the membrane thickness. High permeation rate is particularly desirable to reduce energy consumption; therefore, an ideal membrane should be as thin as possible without forfeiting the quality of permeate [7].

Based on morphology, membranes can be divided into the dense and porous membrane. The transport mechanism across a porous and a dense membrane is different. In porous MF/UF membranes, the transport mechanism is based on pressure-driven convective flow through the pores. and the exclusion based on the size of species, so-called molecular sieving mechanism, is the main reason for separation [7]. In contrast, the transport of solute and solvent in a dense NF/RO membrane occurs based on the solution-diffusion mechanism in which the molecule of solute and solvent first adsorbed onto the active surface of membrane, then diffuse through the membrane, and finally desorbed at the permeate side [7]. The exclusion in the NF/RO membranes is based on the difference in solubility and diffusivity of the components within the membrane.

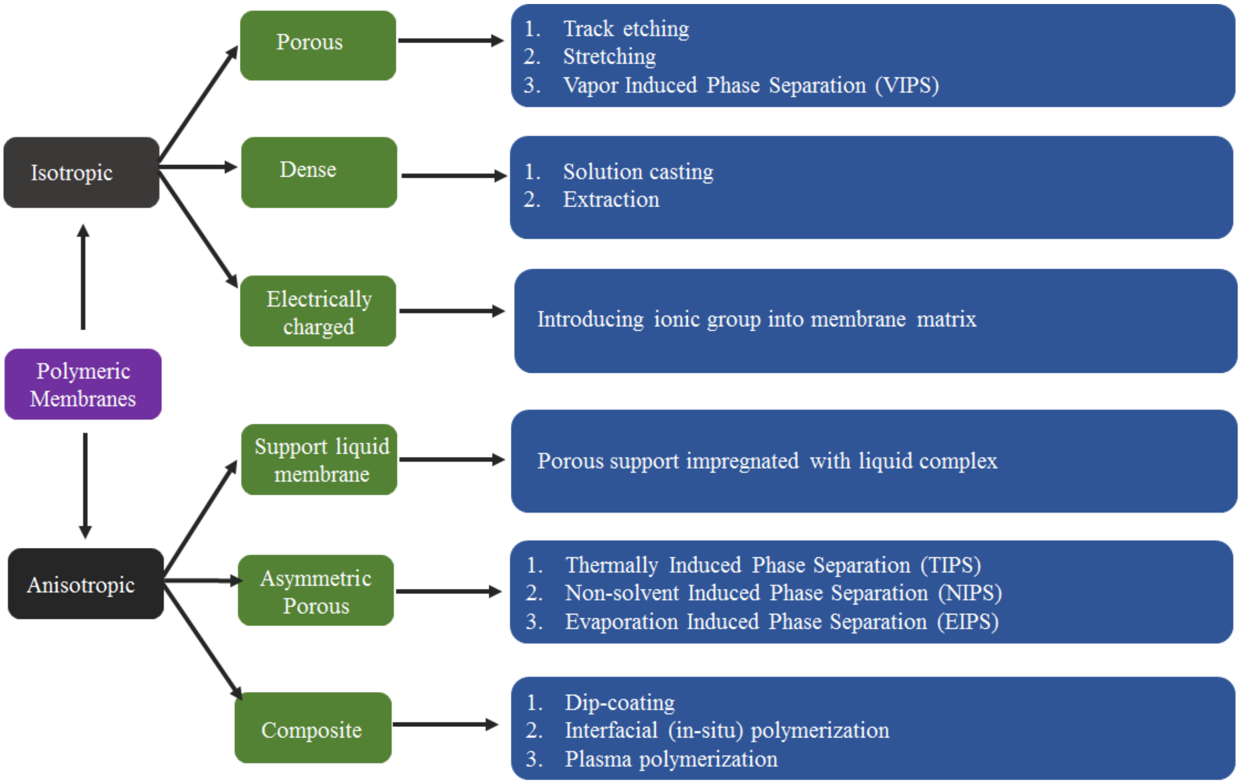

Figure 1.2. Fabrication techniques for preparation of the polymeric membranes

1.4 Fabrication techniques of porous and dense membranes

There are different techniques to fabricate polymeric membranes (Figure 1.2). The desired properties of the resulting membranes determine the proper fabrication technique. The technique that is most commonly used to prepare porous membrane is phase inversion. This process depends on the separation of solvent and non-solvent in a polymer solution, resulting in a porous polymer film. During the phase inversion process, a thermodynamically stable polymer solution faces a liquid-liquid demixing and then is divided into two phases, a polymer-rich that eventually construct membrane matrix and a polymer lean phase that construct membrane pores [8].

Phase inversion process can be achieved by multiple methods including (i) immersion of cast polymer film into nonsolvent bath (NIPS), (ii) immersion of the polymer film in a non-solvent vapor phase (VIPS), (iii) evaporation of the volatile solvent from the cast polymer film (EIPS), and finally (iv) lowering the temperature of the casting solution below a critical threshold (TIPS) [6]. NIPS is the most broadly used method to fabricate porous membrane. In this method, a homogenous polymer solution is cast on a flat surface and then put into a container filled with a nonsolvent (coagulation bath). The phase inversion process is controlled by diffusion of low molecular weight constituents, which are solvent and nonsolvent (mostly water). During phase inversion, the solvent in the polymer solution is replaced with non-solvent in the coagulation bath which leads to changes in the composition of the polymer film, until the composition of the polymer-rich phase reaches the glass transition composition that ends up solidification. Subsequently, the film's structure is fixed at that point and polymer membrane with porous or dense structure forms [9].

1.5 Theoretical background on transport phenomena in membrane

Membrane processes are used for separation because the membrane has the ability to transport one component more readily than another. The theory of mass transport through the membrane is determined by the thermodynamics theories. For instance, the permeation of a component through the membrane is because of its chemical potential gradient and is given by the following equation:

$$J_i = -L_i \frac{d\mu_i}{dx} \tag{1.1}$$

Where $\frac{d\mu_i}{dx}$ is the chemical potential gradient through the membrane of thickness x and L_i is a proportionality coefficient. The driving forces for membrane processes (i.e., pressure, concentration, electrical potential, and temperature differences) are associated with the chemical potential gradient.

For pressure-assisted membrane processes Equation 1.2 can be written as follows (Darcy's law for flow in porous media):

$$J_i = -K' c_i \frac{dp}{dx} \tag{1.2}$$

where $\frac{dp}{dx}$ is the pressure gradient across the membrane, K' is a coefficient representing the nature of medium and c_i is the concentration of component i. Darcy's law [6,10,11] can be re-written as :

$$J_w = \frac{\Delta P}{\mu R_m} \tag{1.3}$$

where ΔP is the transmembrane pressure (Pa) and, μ is the dynamic viscosity of the permeate (Pa. s), and R_m is the hydrodynamic resistance of the membrane itself, in the absence of foulants. R_m, membrane hydrodynamic resistance is determined by measuring pure water permeation, and pressure over time through the membrane, and then, calculating the pure water flux (J_w, $m^3/(m^2.s)$) using the above Darcy's law.

For MF/UF membranes, the hydrodynamic resistance of membrane can also be obtained by the Hagen-Poiseuille equation:

$$R_m = \frac{8\delta_m}{n_p \pi r_p^4} \tag{1.4}$$

where δ_m is the thickness of membranes, n_p is the number of pores per unit membrane area, and r_p is the pore radius. According to Equation 1.4, transport through the membranes is directly proportional to the fourth power of the pore radius.

The resistance against water crossing across these membranes is composed of three major constituents, namely (i) the hydrodynamic resistance of the membrane in absent of foulants, (ii) the resistance due to accumulation of foulants at the membrane surface (fouling, cake formation), (iii) the resistance due to the accumulation of low molecular weight solutes at the membrane surface (concentration polarization) [10]. The resistance because of concentration polarization is diagnosed by the generated transmembrane osmotic pressure ($\Delta\pi$). $\Delta\pi$ reduces the effective pressure driving force for solvent transport and Darcy's law for the fouling experiment is written as follows:

$$J = \frac{\Delta P_t - \Delta\pi}{\mu\, R_t} \tag{1.5}$$

where J is the flux in fouling experiment, and R_t is the total resistance against mass transfer. In UF, the osmotic pressure term, $\Delta\pi$ is often neglected since the main contribution to osmotic pressure is from the low molecular weight solutes that pass through UF membrane and the concentration is the same in the feed and permeate side [6].

R_t, the total resistance in Equation 1.7, is described as follows:

$$R_t = R_m + R_c + R_{cp} + \cdots \tag{1.6}$$

where R_c is the resistance of the cake layer deposited on the membrane surface, and R_{cp} is the resistance caused by concentration polarization.

Another important parameter that is used to determine membrane separation performance is its rejection. The intrinsic (real) rejection of a membrane is expressed as:

$$R_j = 1 - \frac{C_{i,p}}{C_{i,f}} \tag{1.7}$$

where $C_{i,p}$ and $C_{i,f}$ (mol/m^3) are the solute concentration in the permeate and feed solutions, respectively. The ratio of the diffusion coefficient and the thickness of the boundary layer (D/δ) is called the mass transfer coefficient k_i , m/s and can be determined by utilizing the van't Hoff equation and film theory. Figure 1.3 demonstrates the schematic diagram of the CP layer established on the membrane surface. Applying the mass balance equation on a control volume in this figure results in the following equation [6]:

$$J.C_i - J.C_{i,p} + D\frac{dC_i}{dx} = 0 \tag{1.8}$$

Suitable boundary conditions are as follows:

$$x = 0 \qquad C_i = C_{i,f}$$

$$x = \delta \qquad C_i = C_{i,m}$$

where δ is the thickness of the mass boundary layer. Using these boundary conditions, the boundary layer film model is derived as:

$$\frac{C_{i,m} - C_{i,p}}{C_{i,f} - C_{i,p}} = \exp\left(\frac{J.\delta}{D_i}\right) = \exp(\frac{J}{k_i}) \tag{1.9}$$

where k_i and D_i are the mass transfer coefficient and diffusion coefficient of solute in water, respectively, and $C_{i,m}$ is the solute concentration at the membrane surface. The van’t Hoff equation provides the osmotic pressure difference for solute as:

$$\Delta\pi = RT\left(C_{i,m} - C_{i,p}\right) \tag{1.10}$$

where T (K) is the absolute temperature and R is the universal gas constant $(J/mol\,.K)$.

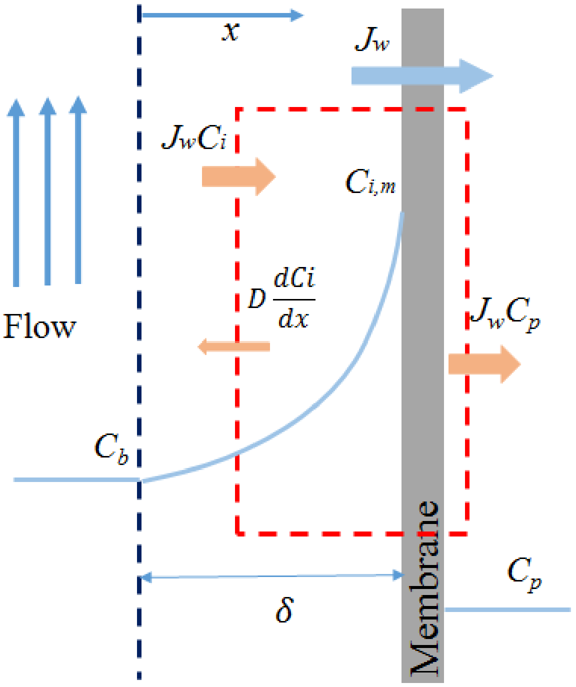

Figure 1.3. Schematic diagram of the CP layer

Replacing $C_{i,m} - C_{i,p}$ from Equation 1.10 into Equation 1.11 leads to:

$$\Delta\pi = RT(C_{i,f} - C_{i,p})\exp(\frac{J}{k_i}) \tag{1.11}$$

Finally, $\Delta\pi$ can be calculated by replacing $C_{i,f} - C_{i,p}$ using Equation 5 as following:

$$\Delta\pi = RTC_{i,f}R_j\exp(\frac{J}{k_i}) \tag{1.12}$$

The cake layer hydrodynamic resistance R_j, which is occurred by the accumulation of organic solute and colloidal particles at the membrane surface can be determined by the film theory. Considering R_c, the permeate flux can be written as:

$$J = \frac{\Delta P_c}{\mu R_c} = \frac{\Delta P_m}{\mu R_m} = \frac{\Delta P_t - \Delta\pi_m}{\mu(R_m + R_c)} \tag{1.13}$$

where ΔP_t , ΔP_c , and ΔP_m (Pa) are the total, trans-cake, and trans-membrane hydraulic pressures, respectively. The total applied pressure (ΔP_t as the driving force of transport through the membrane) includes the trans-cake hydraulic pressure (ΔP_c), the trans-membrane pressure (ΔP_m), and the transmembrane concentration polarization ($\Delta \pi_m$).

1.6 Filtration configurations

There are two process modes for a membranes filtration setup: dead-end and cross-flow filtration, as shown in Figure 1.4. In dead-end filtration, the feed stream is perpendicular to the membrane surface; therefore the retained particles built up and form a cake layer at the membrane surface. The thickness of the cake layer grows with filtration time, and as a result, the permeation rate reduces with increasing cake layer thickness. On the other hand, in cross-flow filtration, the feed flow is parallel to membrane surface so, there are several advantages for the cross-flow mode comparing to the dead-end mode such as improved fouling tolerance, higher sustainable flux, less requirement for cleaning, an extended membrane lifetime.

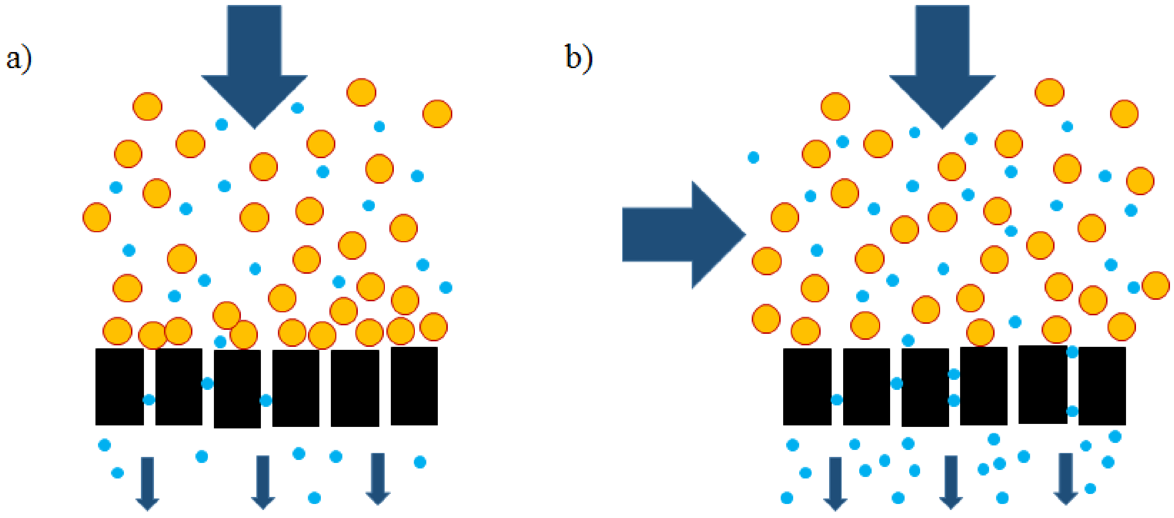

Figure 1.4. Filtration configurations, a) Dead-end, b) Crossflow

1.7 Membrane Fouling

Organic fouling on the membrane is a complex phenomenon [12]. Fouling is the result of specific and non-specific interactions between foulants and membrane surface. Specific interaction refers to covalent bonding and coordination interactions between specific functional groups such as metal-carboxyl and amino-carboxyl. Nonspecific interactions refer to van der Waals interactions, hydrophobic interaction and hydrogen bonding and electrostatic interactions [11]. The fouling on the membrane can be affected by a number of physical and chemical parameters including [13]:

- Membrane properties: surface roughness, charge, hydrophobicity/hydrophilicity, surface functional groups, pore size distribution
- Feed-water compositions: foulants type, concentration, pH, ionic strength
- Hydrodynamic conditions (operational conditions): cross-flow velocity, temperature, flux, transmembrane pressure

In this research, the focus of fouling mitigation is by modifying membrane surface properties. High vulnerability of porous membranes to pore blocking, as an irreversible fouling mechanism results in a dramatic loss of membrane permeation flux [14]. The use of functionalized nanomaterials to synthesize mixed matrix membranes with the aim of changing the physicochemical and antifouling properties of membranes has been suggested to resolve this problem [15–17].

1.8 Polyethersulfone Polymer

Polyethersulfone (PES) is a popular amorphous polymer for its excellent thermal stability, toughness, moderate chemical resistance against many alkalis and mineral acids, and approved for use with food, water, and medical applications [18]. These properties make PES as an attractive material for the preparation of porous MF and UF membranes. PES hold repeated units of ether and sulfone linkage alternating between benzene rings [19]. The main disadvantage of PES is the inherent hydrophobic property [20], which limits its application in membrane water treatment process due to fouling. For this reason, the modification of PES membrane is necessary for reducing the membrane fouling.

1.9 Literature review

Since the first synthesis of the membrane in 1907, the field of membranes has foreseen a continuous growth due to their enormous practical applications. A considerable amount of study has been in progress to enhance the performance of membranes in terms of solute rejection, water permeation, and fouling resistance. Generally speaking, there is a trade-off relationship between permeability and selectivity of conventional membranes that means high water flux membranes display a low rejection result and vice versa. On the other hand, as mentioned in section 1.7, fouling may be impeded through enhanced membrane surface properties. Thus, one of the objectives of the research in the field of membranes has consistently been to fabricate high flux membranes with high separation efficiency and low fouling propensity.

The new improvement in membrane technology was predominately toward (i) improving the membrane fabrication protocols[21,22], (ii) developing nanocomposite membranes by the addition of multifunctional nanomaterials to improve surface properties of membranes [23–26], (iii) developing new polymeric material for the selective thin film and support layers [27] and (iv) improving the surface properties of the thin film composite membrane [28,29].

The use of functionalized nanomaterials to synthesize mixed matrix membranes with the aim of changing the physicochemical and antifouling properties of membranes has been widely investigated [30–32]. However, most of these studies have been focused on the integration of single-element oxide nanoparticles, e.g., Al_2O_3, Fe_3O_4, TiO_2, and SiO_2, into the porous membranes [32]. Yan et al. [33] has reported significant improvement on PVDF membranes by addition of nano-sized Al_2O_3 particle. Ghaemi [34] and coworkers investigated blending surface modified Fe_3O_4 nanoparticles with PES polymer and an increase in hydrophilicity and pure water flux of membrane was reported. Luo et al. [35] developed and characterized anti-fouling composite TiO_2-PES membrane and reported good separation performance. It was reported that TiO_2 nanoparticles produce very oxidizing hydroxyl radicals which easily attack and decompose organic contaminants in water [36]. Blending rod-shaped TiO_2 with a high ratio of length to diameter improved the thermal stability and anti-compaction properties of membranes more than nanoparticles [37].

Recently, the application of carbon-based nanomaterials for preparing UF nanocomposite membranes has attracted considerable attention [26,38–40]. Among these nanomaterials, graphene/ graphene oxide (GO) is being repeatedly employed for the fabrication of novel separation membranes owing to its distinct two dimensional (2D) and single atom thick structure[41]. The field of graphene-based nanocomposites membrane is still in its infancy. Researchers are exploring the influence of different allotropes of carbon/ graphenes via different fabrication methods on membrane separation performance. Wang et al. [42] reported the fabrication of PVDF-GO blended UF membrane. The resulted membranes appeared to be more hydrophilic and have higher pure water flux recovery ratio. Ganesh et al. [43] described preparation of GO blended polysulfone (PSF) mixed matrix membranes and reported their improved performance in terms of pure water flux and salt rejection. Zhao et al. [44] have fabricated a novel GO blended polyvinyl chloride (PVC) membrane. It is claimed that with addition of low fraction of GO powder, the GO-PVC hybrid membranes demonstrated a remarkable improvement in hydrophilicity, water flux, and mechanical properties. Zinadini et al. [20] claimed that the permeation flux and anti-biofouling property of PES-GO membranes can be significantly enhanced with the addition of 0.5 wt.% GO. Wu et al. [45] have developed a novel SiO_2-GO nano-hybrid PSF membrane that exhibited enhanced water permeability with high rejection rate for albumin. Lee et al. [40] demonstrated that addition of GO to PSF has suppressed the fouling to such an extent that 5-fold lengthening between chemical cleaning.

GO nanosheets can adjust membrane structure, improve mechanical strength and enhance hydrophilic properties of the polymeric membrane [20,38,40,42–47]. Individual GO nanosheets within the polymeric matrix are strongly held together with several hydrogen bonding and van der Waals interactions with polymer matrix. It was reported that GO sheets with different lateral size greatly affects the performance of membrane for gas separations [48]. Although GO nanosheets were studied extensively there is a lack of study on the size, shape (nanosheets vs nanoribbons) and oxidation state of GO derivatives that need to be addressed to explain the improved flux, rejection and fouling resistance properties of GO-based nanocomposite membranes.

Another fouling control strategy has been reported by applying an external electric field to electro-conductive membranes (ECMs). The fouling on the membranes can be mitigated due to the dual effect of electrostatic repulsion, gas bubbles generation [49], and the electrochemical oxidation/reduction of the foulants on the membrane [50–53]. The surface charge of the smart membranes fabricated by the incorporation of ITO nanoparticles was reported to be adjustable by applying an external electrical field and therefore can prevent adsorption of foulants based on electrostatic repulsion [54]. HO et al. have developed a graphene oxide/multi-walled carbon nanotubes (GO/MWCNTS) via the blending phase inversion method [55]. Huang et al. fabricated a novel ECM by introducing a stainless steel mesh into a polymeric MF membrane [56]. Liu et al. synthesized reduced graphene oxide/ halloysite nanotube membranes (rGO/HNTs) via polydopamine (PDA) modification on the commercial cellulose acetate membrane [57]. Dudchenko et al.synthesized a robust electrically conductive thin film made of cross-linked polyvinyl alcohol and carboxylated multi-walled carbon nanotubes (PVA-CNT-COOH) via a sequential deposition and cross-linking method [58]. Jassby et al. fabricated polyaniline-coated carbon nanotube UF membrane through a process of electro-polymerization of aniline on CNT substrate under acidic condition [59]. The main objectives are to synthesize more fouling resistance, high water-permeable membranes with tunable surface and bulk properties in order to provide enhanced hydrophilic, electrical, and anti-fouling characteristics.

1.10 Research objectives

The main objective of the research was to develop graphene based-PES nanocomposite membranes to provide a more efficient water pretreatment process with improved fouling resistance characteristics, specifically in oil sand in-situ operations. The general idea of making mixed matrix membranes was to induce the hydrophilic, electrical, and molecular sieve properties of these nanomaterials to the base membrane so creating composite membranes with enhanced separation performance. The interesting properties of graphene nanoplatelets (GNP), graphene oxide (GO), reduced graphene oxide (rGO), longitudinally unzipped graphene oxide nanoribbon (GONR-L), and helically unzipped graphene oxide nano-ribbon (GONR-H) includes outstanding chemical and thermal stability, hydrophilicity, electrical conductivity, and environmental friendliness that offer an extraordinary potential for fabricating nanocomposite membrane with high chemical stability, strong hydrophilicity, and excellent antifouling properties.

The objectives of this research were as follows:

(i) Developing high-performance and durable nanocomposite membranes by incorporation of graphene-based nanosheets and nanoribbons as additives to a polymer film, with the intention of improving the permeation and antifouling properties. In this work, four different graphene oxide (GO) derivatives were incorporated into a polyethersulfone (PES) matrix *via* a non-solvent induced phase separation (NIPS) method. The GO derivatives used have different shapes (nanosheets *vs* nanoribbons) and different oxidation states (C/O=1.05-8.01) with the potential to enhance water flux and suppress fouling of the membranes through controlled pore size, hydrophilicity, and surface charge.

(ii) investigating the fouling behavior of organic foulant from SAGD produced water on synthesized ultrafiltration (UF) membranes PES, PES/PVP, PES/PVP/GO using an extended DLVO (XDLVO) interaction energy analysis, fouling experiments, and quartz crystal microbalance with dissipation monitoring (QCM-D). In the XDLVO analysis, the fundamental interactions (van der Waals, electrostatic, and acid-base interactions) that control organic fouling were evaluated. Surface tension parameters, derived from contact angle measurements, were employed to calculate the free energy of adhesion between membrane and foulant material to elucidate the differences in flux decline.

(iii) Fabricating a novel electro-conductive membrane via pressure-assisted technique where a thin film of reduced graphene oxide/ polyaniline (rGO/PANI) was laminated on the PES substrate. By applying external potentials, the conductive membrane could acquire different electrical charges, enabling them to repel oppositely-charged foulants through electrostatic repulsive forces and minimizing the deposition of oppositely-charged foulants. Moreover, electrochemical reactions may occur on the conductive membrane, which could partially or completely destroy the chemical structure of some foulants. Furthermore, organic fouling could be mitigated by generation of gas bubbles in a specific range of potentials over conductive membrane.

1.11 Thesis structure

The present dissertation was organized in a paper-based format.

Chapter 1 of this thesis gives a general overview of the SAGD process and the conventional produced water treatment methods used by the oil sands industries. The limitations of the current water treatment methods were explained. The membrane-based separation processes were presented as a feasible solution to these limitations. In the end, the literature review on UF composite membrane and the objective of this work was presented.

Chapters 2, 3, and 4 each were written based on submitted/published articles.

Chapter 2 is based on the outcome of a series of systematic studies on the effect of incorporation of graphene-based derivatives on the final properties of phase inversion PES membranes. The graphene-based derivatives used have different shapes (nanosheets *vs.* nanoribbons), and different oxidation states. The incorporation of the graphene-based nanomaterials has improved antifouling performance of polymeric PES membrane, as well as enhanced pure water flux and separation performance of composite membranes evaluated using dead-end cell filtration setup. In addition, the membranes are characterized for contact angle, zeta potential, field emission scanning electron microscopy (FESEM), X-ray photoelectron spectroscopy (XPS), Fourier-transform infrared spectroscopy (FTIR), and pore size.

Chapter 3 presents the results of a study on antifouling behaviors of GO modified nanocomposite membranes through QCMD and surface energetics analysis. The extent of organic fouling relies on membrane-foulant affinity, which depends on the physicochemical properties of the foulant and membrane. XDLVO interaction energy analysis, as well as quartz crystal microbalance with dissipation monitoring (QCM-D), were used to explain the adsorption behavior of organic matters from BFW waste of SAGD operation on three fabricated ultrafiltration membranes. Surface tension parameters, derived from contact angle measurements, were used to calculate the free energy of adhesion between membrane and foulant material to explain the differences in flux decline in cross-flow filtration setup.

Chapter 4 provides the outcomes of a study on the antifouling behavior of electro-conductive composite membranes (ECMs) fabricated by reduced graphene oxide – polyaniline (rGO-PANI). The innovative adjustment relies on mixing rGO as a higher conductive component with PANI polymer as an adhesive, protective component that together creates a stabilized conductive thin film laminate on PES support. The antifouling propensity of the fabricated membranes was evaluated using sodium alginate as model foulant as well as BFW waste of SAGD operation. The substantial changes in the antifouling properties by applying the electric potential of 2V and higher on the surface on ECMs were discussed in this chapter.

Chapter 5 summarizes the major findings of all parts of this research and provides a concluding discussion. Moreover, suggestions and recommendations for further advancement of the ongoing research were provided.

Chapter 2

Development of advanced nanocomposite membranes using graphene nanoribbons and nanosheets for water treatment

2.1 Introduction

Improved water usage efficiency has driven the research community to explore advanced methods for water recycling that are more environmentally sustainable and energy-efficient [60]. Filtration using polymeric membranes has attracted attention due to the ease of operation and integration with other processes, reliable contaminant removal without production of any harmful by-products, and cost-efficiency, compared to other conventional filtration technologies [30,61].

Polyethersulfone (PES) has been extensively used for applications in ultrafiltration (UF) and nanofiltration (NF) systems, where it can offer superior mechanical strength, chemical and thermal stabilities and a wide range of pH resistance [20]. PES, however, is inherently fairly hydrophobic, which could lead to severe fouling in long-run operations. Throughout the fouling process, the key membrane properties, i.e., water permeation and solute rejection rate, are affected that ultimately increase the operating cost, and decrease the membrane lifespan [5].

Surface properties of polymeric membranes can have significant impacts on the initial stages of fouling where the negatively-charged and hydrophilic surfaces can effectively hinder the fouling process [8-10]. As a result, membrane cleaning interval can be prolonged. Numerous studies have investigated surface properties and morphologies of the polymeric membranes with the objective to fabricate fouling-resistant surfaces against different kinds of foulants [5,11,31,32,64]. Several approaches have been explored, such as surface coating [65,66], chemical grafting [67], ultraviolet-assisted plasma treatment [68,69], and physical blending with antifouling materials [42].

Incorporation of hydrophilic nanofillers into the polymer matrix to fabricate polymer nanocomposite membranes is one of the most effective approaches that showed promising potentials for surface modification [32]. This technique has the advantage of being straightforward and cost-effective and can enhance antifouling properties, selectivity, and thermomechanical stability of membranes [70].

Various studies explored the effect of incorporating a broad category of nanofillers including single-element oxides (TiO_2 [35,37], ZrO_2 [15,71,72], MgO [14], Al_2O_3 [33], SiO_2 [16,73], Fe_2O_3 [34]), double-element oxides (indium tin oxide, ITO [54]), molecular-sieve nanomaterials (zeolites [74]), and carbon-based nanomaterials (carbon nanotube [75,76], cellulose nanocrystals (CNC) [77], and graphene oxide (GO) [30,43]) into polymer membrane matrix. Recently, graphene-based nanomaterials have emerged as a topic of vast scientific interest [39,78–80]. These nanomaterials are carbon allotropes composed of a monolayer of tightly packed carbon atoms with various geometrical structures, e.g., nanosheets, nanoribbons, and nanotubes [46]. Graphene-based nanomaterials can also be readily synthesized with different functional groups, e.g., carboxyl, epoxy, and hydroxyl, positioned at their edges and basal planes. Two exceptional properties of these nanomaterials have made them attractive for the development of nanocomposite membranes. First, most GO derivatives have high charge density that help to reach stable dispersion in organic solutions (e.g., DMAc solution) [81]. Second, due to different oxidation state, they possess tunable hydrophilic properties that can be induced to the polymer material and high-performance membranes can be fabricated in terms of flux and antifouling properties to satisfy specific water treatment applications.

A summary of earlier studies on the effect of incorporating GO nanofillers on membrane properties is presented in Table 2.1. As can be observed, the addition of GO nanofillers has generally improved mechanical, permeation, and antifouling properties of polymer membranes. However, these results were primarily based upon utilization of GO nanosheets with specific geometrical and chemical characteristics, and the effect of shape and oxidation state of nanofillers on membrane properties yet to be explored.

Table 2.1. Brief overview of previous studies on the effect of GO on membrane properties

Reference	Additive	Polymer	Major finding
Ganesh et al. [43]	GO	PSf[1]	Increase in pure water flux and salt rejection
Yu et al. [82]	HPEI[2]-GO	PES	Lower permeation but improved tensile strength and antifouling properties
Lee et al. [40]	GO	PSf	Enhanced antifouling ability of the developed membrane bioreactor (MBR)
Zhao et al. [44]	GO	PVC[3]	Significant enhancement in hydrophilicity, water flux, and mechanical properties
Wu et. al. [45]	SiO_2-GO	PSf	Enhanced permeation and protein rejection and anti-fouling ability
Lim et al. [83]	TA[4]-GO	PEI[5]	Excellent antibacterial activity against E. Coli
Zinadini et. al.[20]	GO	PES	Improved water flux, dye removal, and anti-biofouling properties
Xu et al. [84]	Organosilane - GO	PVDF[6]	Enhanced mechanical strength, permeation and flux recovery ratio (FRR)

[1]Polysulfone, [2]Tannic acid, [3]Polyvinyl chloride, [4]Hyperbranched polyethylenimine, [5]Polyethylenimine, [6]Polyvinylidene fluoride

In the present work, we report the effect of incorporation of four GO derivatives on physicochemical characteristics and permeation properties of the polyethersulfone (PES) membranes. The GO derivatives used in this study include graphene nano-platelet (GNP), graphene oxide (GO) nano-sheet, longitudinally unzipped graphene oxide nano-ribbon (GONR-

L), and helically unzipped graphene oxide nano-ribbon (GONR-H). They have different shapes and oxidation states with the potentials to enhance water flux and fouling resistance of the nanocomposite membranes through controlled surface charge density, and hydrophilicity of membrane surface. The nanocomposite membranes were fabricated *via* non-solvent phase separation (NIPS) method. Structural morphology, surface properties, and chemical composition of fabricated membranes were examined by field emission scanning electron microscopy (FESEM), Fourier-transform infrared spectroscopy (FTIR), water contact angle, and surface zeta potential measurements. Water flux, rejection of organic matter and fouling resistance of the synthesized nanocomposite membranes were studied using synthetic and real produced water and was compared with unmodified PES membrane.

2.2 Materials and Methods

2.2.1 Chemical and reagents

PES was obtained from BASF and was used to prepare porous UF membranes. N,N-dimethylacetamide (DMAc), potassium permanganates, and H_2SO_4 were purchased from Fisher Scientific. Graphene nanoplatelets (GNP) and GO were supplied from Carbon Upcycling Technologies (CUT). The fluids used for testing fouling on the membrane were SAGD produced water samples provided from a SAGD water treatment plant located in the Athabasca oil sands region of Alberta. The GONR-L and GONR-H were synthesized by using the previously reported carbon nanotube unzipping procedure where multiwalled carbon nanotubes were treated with potassium permanganates in acid [85–89].

2.2.2 Preparation of GO/PES nanocomposite membranes

GO/PES membranes were fabricated via NIPS method. This process relies on the phase separation of a polymer solution, producing a porous polymer film. Homogeneous polymer solutions were prepared by mixing DMAc with 18 wt.% PES, 2 wt.% PVP, and different ratio of GO derivatives to polymer (0.05, 0.1, 0.2 wt.%) shown in Table 2.2. To prepare a casting solution, first GO nanofillers were uniformly dispersed in DMAc using a probe sonicator for 15 minutes. Then, PES and PVP were added to GO-DMAc mixture and stirred overnight. The solution was then kept still for 24 h at room temperature for the complete removal of the air bubbles from the solution. After that, the polymer solution was cast on the flat glass surface using a film applicator (Gardco, MICROM II) with casting speed of 5 mm/s and the clearance gap of 150 microns. Finally, the cast film was immersed in a water bath for 24 hours to complete membrane formation by liquid-liquid demixing.

Table 2.2. Concentration of GO nanofillers in the polymer casting solution

Membrane	Nanofiller	The ratio of nanofiller to polymer
M0	---	0
M1	GNP	0.05
M2	GNP	0.1
M3	GNP	0.2
M4	GO	0.05
M5	GO	0.1
M6	GO	0.2
M7	GONR-L	0.05
M8	GONR-L	0.1
M9	GONR-L	0.2
M10	GONR-H	0.05
M11	GONR-H	0.1
M12	GONR-H	0.2

2.2.3 Measurement of porosity and pore size

Porosity is the ratio of the total pore volume to the volume of the membrane. The gravimetric method was used to evaluate average porosity (ε) of membranes [90]:

$$\varepsilon = \frac{w_1 - w_2}{(A \times l)\rho} \qquad (2.1)$$

where w_1 and w_2 are the mass of wet and dry membranes (g), respectively; A is the membrane surface area (cm^2), l is the membrane thickness (cm), and ρ is the water density (0.997 g/cm^3 at 25 °C). All measurements were repeated at least 3 times and the average value were reported as the membrane porosity.

To measure the membrane average pore size, the relationship proposed by Guerout-Elford-Ferry [20] is used:

$$r_{\mathrm{m}} = \sqrt{\frac{(2.9 - 1.75\varepsilon)8\eta l Q}{\varepsilon \times A \times \Delta P}} \qquad (2.2)$$

where η is the water viscosity (8.9×10^{-4} Pa.S at 25°C), Q is the permeate volumetric flow rate (m^3/s), and ΔP is the transmembrane pressure (Pa). The operational transmembrane pressure is 0.28 MPa (40 psi).

2.2.4 Pure water flux measurement

Pure water flux experiments were conducted using a lab-scale batch filtration setup consists of a dead-end stirred cell (Amicon, UFSC40001) with the capacity of 400 ml and effective membrane area of 41.8 cm^2. Pressurized nitrogen gas was used to apply 40 psi pressure. A digital balance (ME4002, Mettler Toledo, USA) connected to a computer was used to automatically monitor and record the permeate water flux over time. The fabricated membranes were immersed in water for

24 hours and then were compacted at 70 psi for 1 hour before each permeation test to achieve a steady flux. During filtration, the feed solution was stirred at a rate of 300 rpm. The following equation was used to calculate the water flux (J_0):

$$J_0 = \frac{W}{A \times \Delta t} \qquad (2.3)$$

where W is the mass of the permeate water (kg), A is the membrane effective area (m^2), and Δt is the permeation time (h).

2.2.5 Produced water treatment

To evaluate the separation performance of the synthesized membranes filtration experiments were conducted on WLS inlet water of SAGD operation. The concentration of contaminants in the WLS inlet water was determined by ICP-OES (Thermo Scientific, iCAP™ 7400, Massachusetts, USA) and TOC analyzer (Shimadzu, model TOC-V; detection range 3-25,000 mg/L, Kyoto, Japan) and the results are presented in Table 2.3. The rejection of organic matter by membranes was calculated by measuring the TOC in the collected permeate during the filtration of WLS inlet water at 25° C and 40 psi using the following equation:

$$\text{Rejection (\%)} = (1 - \frac{C_\text{p}}{C_\text{f}}) \times 100 \qquad (2.4)$$

where C_p and C_f are the TOC content in permeate and feed solution, respectively.

2.2.6 Fouling tests

To investigate fouling behavior of membranes a three-step experimental protocol was followed. First, the pure water flux, J_{W1}, was measured. Then, the water flux during filtration of WLS inlet water, J_{Wf}, was recorded. After hydraulic washing of the membrane surface with deionized water for 10 min, the pure water flux of cleaned membrane, J_{W2}, was measured again. To determine the antifouling property of the membranes total fouling ratio (DR_t) and flux recovery ratio (FRR) were calculated as follows [82]:

Table 2.3. Properties of WLS inlet water

Parameters	WLS Inlet Water
pH	7.0
TOC (mg/L)	550
TDS(mg/L)	1050
Conductivity (µS/cm)	1508
Na^+ (mg/L)	310
Cl^- (mg/L)	240
Mg^{2+} (mg/L)	0.371
Ca^{2+} (mg/L)	2.83
Iron, total (mg/L)	1.02
$SiO_{2,}$ dissolved (mg/L)	63.7

$$DR_t = 1 - \frac{J_{\mathrm{Wf}}}{J_{\mathrm{W1}}} \quad (2.5)$$

$$FRR = \frac{J_{\mathrm{W2}}}{J_{\mathrm{W1}}} \quad (2.6)$$

Here, DR_t is the sum of irreversible fouling ratio (DR_{ir}) and reversible fouling ratio (DR_r) which are associated with the flux decline due to the adsorption of foulant molecules on a membrane surface and concentration polarization phenomenon, respectively. DR_{ir} and DR_r can be calculated by the following equations:

$$DR_{ir} = 1 - \frac{J_{\mathrm{W2}}}{J_{\mathrm{W1}}} \quad (2.7)$$

$$DR_r = \frac{(J_{\mathrm{W2}} - J_{\mathrm{Wf}})}{J_{\mathrm{W1}}} \quad (2.8)$$

2.2.5 Polymer solution viscosity measurement

The viscosity of the polymer solution was measured by Rheometer (Brookfield, DV-III Altra, Massachusetts, USA). The relationship between viscosity and shear rate for each casting solution was acquired at a shear rate ranging from 50 to 250 s^{-1} at 25 ˚C.

2.2.6 Chemical composition tests

Potassium bromide-Fourier transform infrared (KBr-FTIR) spectroscopy was used to provide information on the type of functional groups present in GO derivatives. The FTIR spectra were obtained using FTIR imaging system (Varian Digitlab, FTS 7000, Massachusetts, USA). This device is equipped with a mercury-cadmium-telluride (MCT) detector with high photometric accuracy and sensitivity. The KBr-FTIR spectroscopy exploits the property of KBr that forms a transparent sheet in infrared region when subjected to high pressure. To prepare 13 mm-diameter pellets, approximately 1% samples of GO nanomaterials mixed with fine moisture-free KBr were put into the pellet-forming die. A force of about 8000 psi was applied for several minutes to create transparent pellets. The background was measured using pure KBr pellets. All samples were scanned over the range of 600- 4000 cm^{-1} and 100 scans were averaged for each spectral measurement.

Detailed elemental and chemical bonding analysis of GO derivatives was conducted using X-ray photoelectron spectroscopy (XPS). XPS analysis provided information about the outer 1-10 nm of GO derivative samples. In the present work, XPS imaging spectrometer (Kratos, AXIS Ultra, Manchester, UK), equipped with a monochromatic Al Kα X-ray source were used. Low-resolution survey scans, as well as a high-resolution scan of C, were taken. Survey spectra were obtained with a pass energy of 160 eV, and sweep time of 100 s in the range of 0- 1100 eV. High-resolution spectra were obtained for C 1sand then were analyzed using CasaXPS software.

2.2.7 Surface properties (wettability and surface charge)

Water contact angle on the flat sheet membranes was measured to investigate the surface wetting characteristic of fabricated membranes as a function of GO contents. The measurement was carried out based on sessile drop method using goniometer Kruss Model DSA 100E (Hamburg, Germany) with deionized water. The higher the surface wettability, the lower is the contact angle. For each sample, five measurements were performed, and the average was reported.

The surface zeta potential of the fabricated membranes was measured using Surpass3 analyzer (Anton Paar, Graz, Austria). This device evaluates the surface zeta potential based on streaming potential and streaming current measurements. The zeta potential values were determined at pH 7.0 and 25 ˚C using 0.001 M KCl solution.

2.2.8 Membranes morphology study

To study the effects of GO content on membranes microstructure, the morphology of fabricated membranes was examined using field emission scanning electron microscopy (FESEM). The dried membranes samples were fractured under liquid nitrogen and were mounted on SEM stub. To improve electron conductivity of the samples 8 nm gold Au was sputter-coated on the surface of the membranes using Gatan 682 Precision Etching and Coating System (Gatan, Inc., Pleasanton, USA). The cross-sectional images were taken at 5 kV and high vacuum condition.

2.3 Results and discussion

2.3.1 FTIR measurement results

FTIR measurement results on the GO derivatives is shown in Figure 2.1. The peak at 3435 cm^{-1} is attributed to the OH stretching vibrations in carboxylic groups. The transmittance bands at 1625 cm^{-1} is ascribed to C=C in benzene rings, and sharp, intense peak at 1718 cm^{-1} is attributed to C=O carboxylic groups. The peaks at 1396 cm^{-1}, 1193 cm^{-1}, and 1016 cm^{-1} are attributed to C-O single bond and C=O double bond vibrations. Finally, the peak at 890 cm^{-1} is ascribed to aromatic sp^2 C-H bending. All these groups are valid and are expected to be present in the structure of GO derivatives. GO, GONR-L, and GONR-H possess the same molecular groups, but it seems to differ in chemical makeup (oxidation state). On the contrary, GNP showed smaller peaks for OH stretching vibrations and C=C in benzene rings. It reveals that GNP has a few carboxylic and hydroxyl groups and confirms that GO, GONR-L, and GONR-H are effectively functionalized.

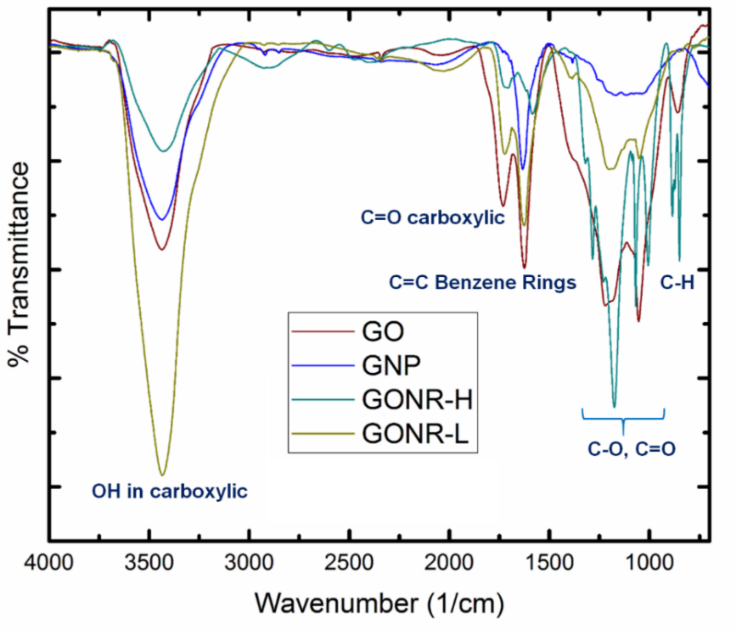

Figure 2.1 The FTIR spectra of different graphene-based nanomaterials

2.3.2 XPS Characterization of Graphene Nanofillers

To further investigate the functional state of oxygen existing on the surface of nanofillers XPS analysis was conducted. The survey scans for GNP, GO, GONR-L and GONR-H are presented in Figure 2.2. The analysis of survey spectra showed that oxygen functional groups on GONR-H (C/O = 3.10), GO (C/O = 2.04), and GONR-L (C/O = 1.05) were significantly higher than that in GNP (C/O = 8.01). The magnified Survey scan is presented in Figure A1 in Appendix A. High-resolution C 1s spectra of the GNP, GO, GONR-L and GONR-H are presented in Figure 2.3. The original chemical shifts of C-C, C-OH, C-O-C (epoxide or cyclic ether), and O-C=O bonds were positioned at 284.5, 285.7, 286.6, and 288.5 eV, respectively. A tolerance of ±0.3 eV shift from the initial peak position was permitted during the fitting. Shirley algorithm was used to determine background for all regions.

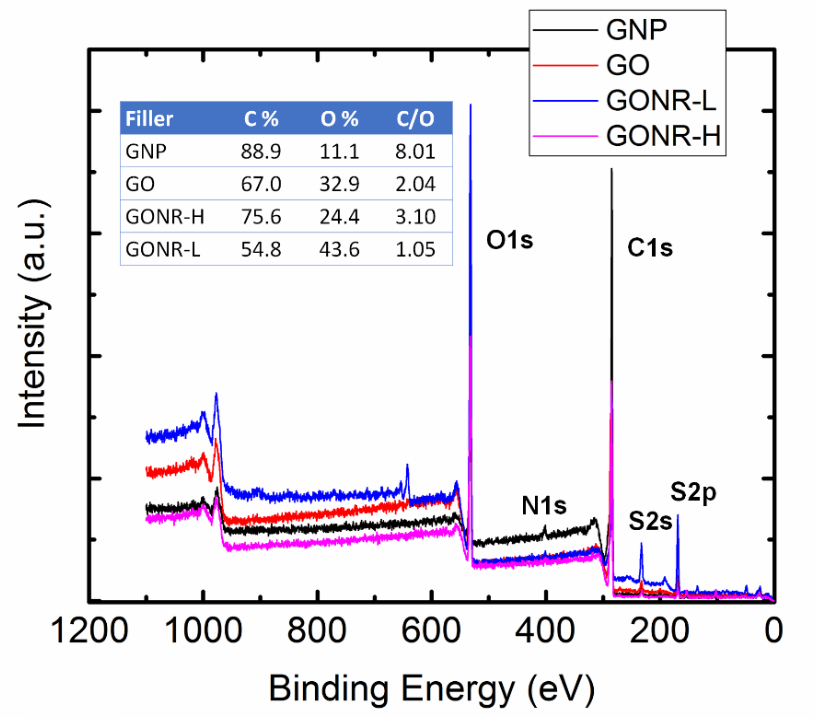

Filler	C %	O %	C/O
GNP	88.9	11.1	8.01
GO	67.0	32.9	2.04
GONR-H	75.6	24.4	3.10
GONR-L	54.8	43.6	1.05

Figure 2.2 XPS survey spectra of GNP, GO, GONR-L, and GONR-H along with carbon to oxygen ratio (C/O) in these nanofillers

The deconvolution of C 1s peaks indicated that oxygen functional groups on GO derivatives were comprised of hydroxyl (C-OH, 285.7 eV), epoxide (O-C-O, 286.6 eV), and carboxyl (O=C-OH, 288.8 eV), however, the majority of these groups in GO, GONR-L, and GONR-H are hydroxyl/epoxide and few of them are carboxyl groups. A possible explanation for this might be that the carboxyl groups are mainly positioned at the graphene edges while hydroxyl and epoxide are mostly located in the graphene basal plane [86].

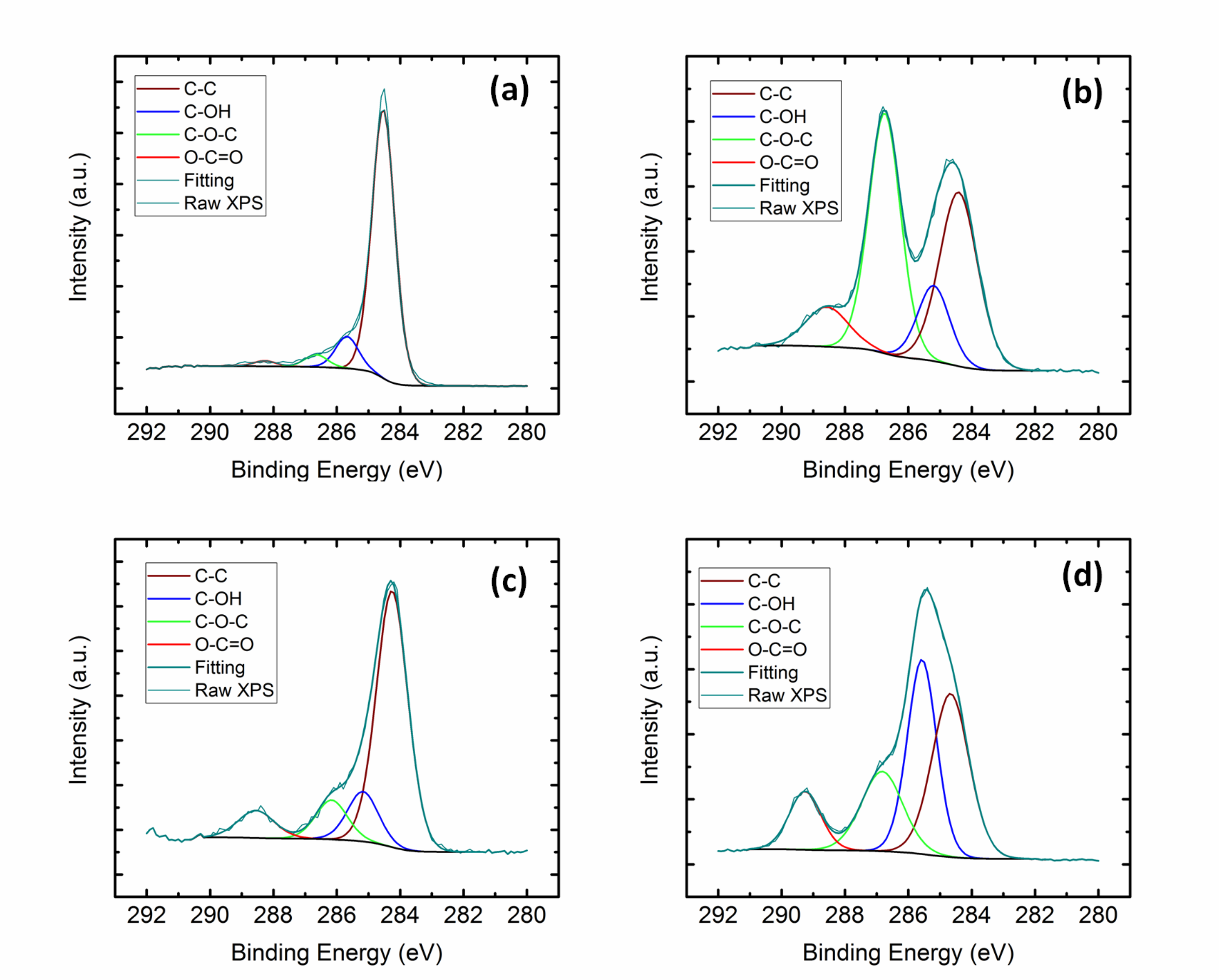

Figure 2.3. C 1s high-resolution spectra of (a) GNP, (b) GO, (c) GONR-H, and (d) GONR-L

2.3.3 Surface and cross-section morphology

The internal structure of the pristine PES membrane and GO-based nanocomposite membranes (0.1 wt.% nanofiller) is presented in Figure 2.4. As can be observed, all membranes have an asymmetric structure with a dense skin top layer supported by a porous finger-type structure, which is a common internal morphology for NIPS membranes [70,91]. According to Figure 2.5, the addition of 0.1 wt.% nanofillers decreased the thickness of membranes with from 120 μm to 100±5 μm. However, the average skin layer thickness increased significantly from 150 nm to 350±50 nm. The addition of GO nanofillers slows down the solvent/nonsolvent exchange rate in the coagulation bath and thus leads to the formation of thinner membranes with thicker skin layer due to the entrapment of more GO nanofillers at the top surface during phase separation [91,92].

It is worth mentioning that GO nanofillers are hydrophilic additives and tend to enhance thermodynamic instability of casting solution that accelerates the demixing of solvent and nonsolvent. Also, the swelling of the polymer film by hydrophilic nanofillers prior to its solidification allows for more passage of nonsolvent to the casting film during NIPS process and might increase the membrane thickness. However, a significant increase in the viscosity of the casting solution (Figure A2 in Appendix A) has countered these effects and increased the skin layer thickness due to a reduction in mutual diffusivities between solvent and nonsolvent.

Figure 2.5 shows that the thickness of skin layer increased by increasing the GONR-H loading in the casting solution. The same results were obtained for other types of nanofillers. As can be observed in Figure 2.5, the thickness of skin layer increased significantly from 150 nm to 600 nm This finding can also be attributed to an increase in the polymer solution viscosity which reduced the phase inversion rate on the top surface and consequently led to a thicker skin layer.

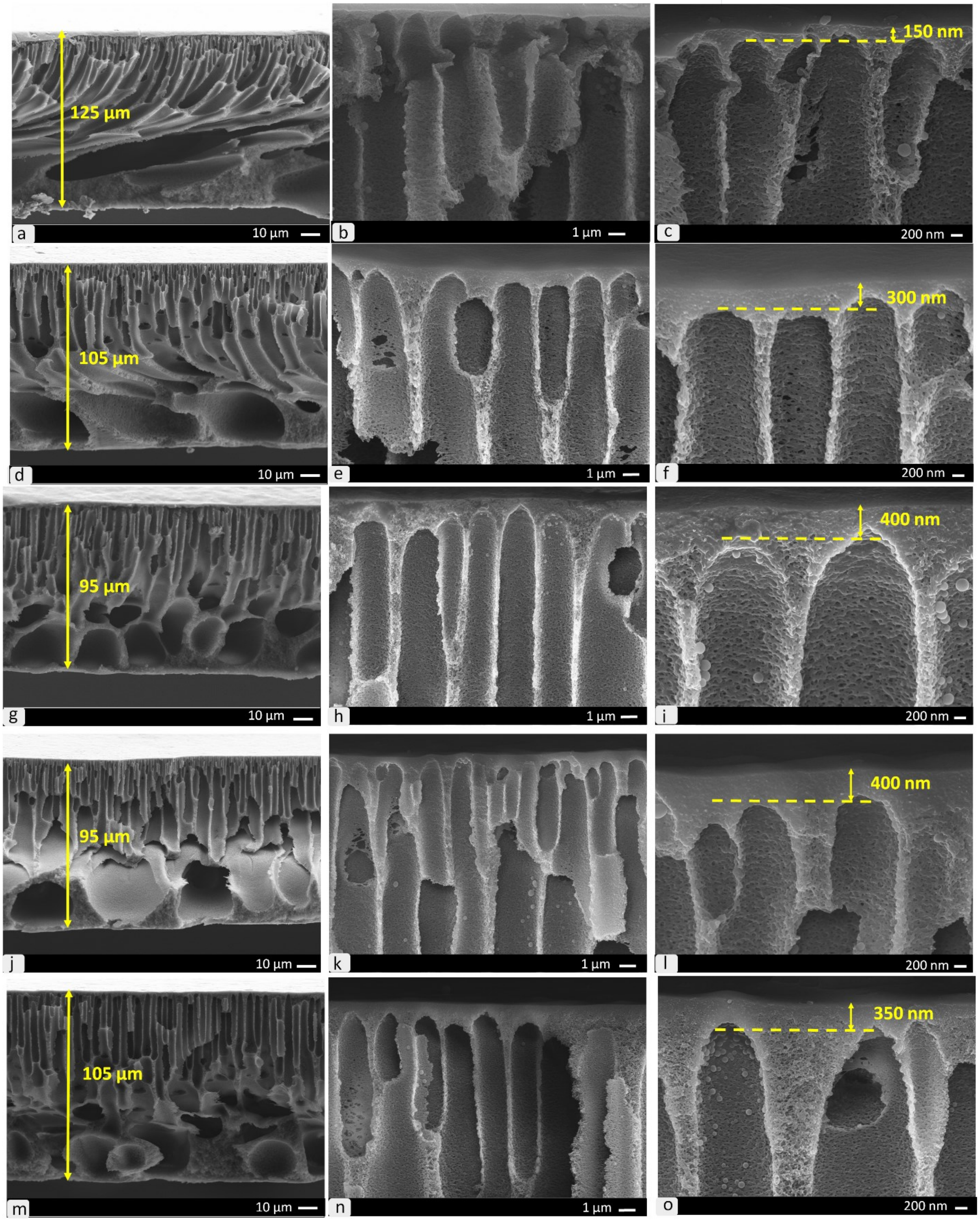

Figure 2.4. Cross-sectional FESEM images of unmodified PES (a-c) and nanocomposite membranes loaded with 0.1 wt.% of (d-f) GNP, (g-i) GO, (j-l) GONR-L, and (m-o) GONR-H with different magnification

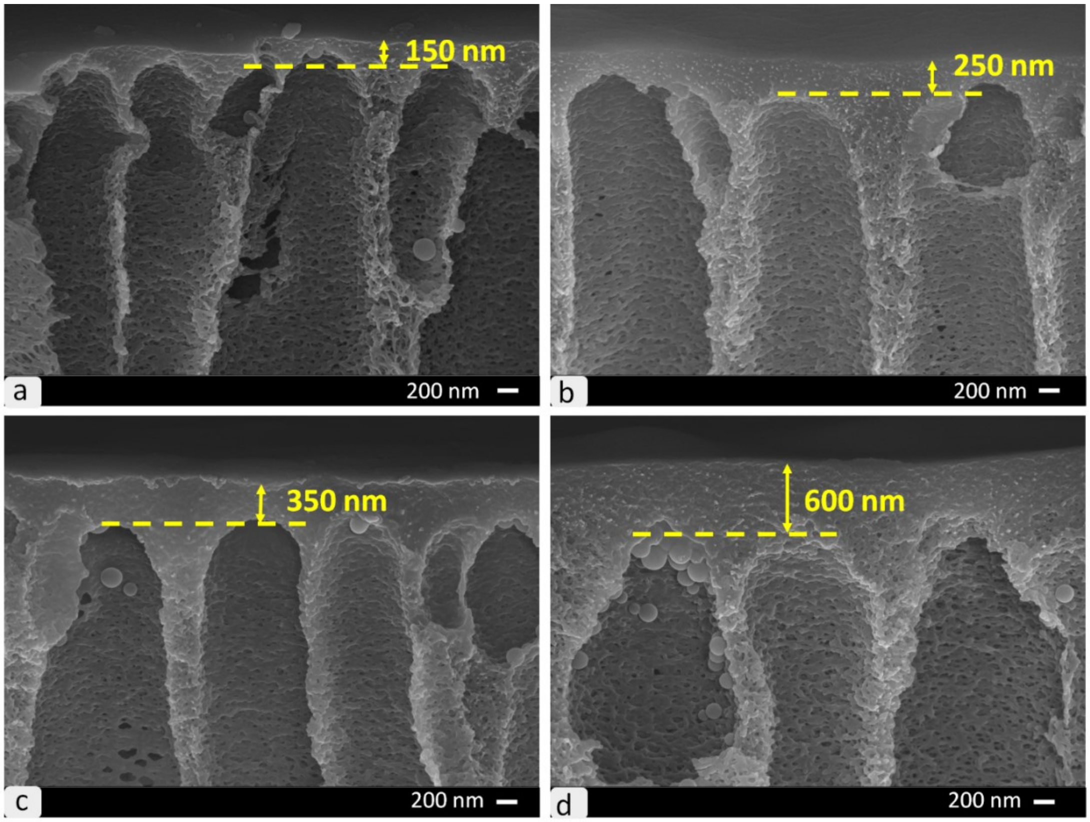

Figure 2.5. Cross-sectional FESEM images of the skin layer of (a) unmodified PES and nanocomposite membranes containing (b) 0.05 wt.%, (c) 0.1 wt.%, and (d) 0.2 wt.% GONR-H

2.3.4 Contact Angle measurement results

The hydrophilic property of fabricated membranes can be studied by water contact angle measurement. Surface hydrophilicity is a decisive parameter in determining the antifouling characteristics of NF/UF membranes. Based on sessile drop method, water droplets with a volume of 2 μl were gently placed on the surface of membranes, and the initial contact angle was measured after 3 s. Higher contact angle represents the more hydrophobic surface, and lower contact angle reveals the higher surface energy, as well as, hydrophilic nature of membrane. As presented in Table 2.4, contact angle decreased with the incorporation of graphene-based nanomaterial into the membrane matrix. The contact angle for the base membrane was 64.6˚. By adding 0.2 wt.% GO, GNR, GONR, and GNP the water contact angle reduced significantly to 43.8˚, 45.6˚, 50.2˚, and 56.9˚, respectively. Since graphene nanomaterials are more hydrophilic than PES, their accumulation on the surface can reduce interface energy. During membrane formation by NIPS method, graphene nanofillers move to the surface of the casting film to be exchanged with water. Most of these nanofillers entrap in the solidified film and thus remain in the polymer matrix. This is justified by the darker color of the top surface as compared to the bottom surface of synthesized membranes. As a result, the contact angle values of all graphene-based nanocomposite membranes were less than the unmodified PES membranes, suggesting that the incorporation of graphene nanofillers leads to the formation of more hydrophilic membranes.

2.3.5 Membrane surface charge results

Membrane surface charge density can change by the incorporation of nanofillers due to their surface functional groups. The surface charge of synthesized membranes is presented in Table 2.4. At pH values higher than the isoelectric point (IEP), the sulfonic acid groups in PES polymer become negatively charged ($–SO_3^-$) upon dissociation. By incorporation of GO nanofillers, the membrane surface becomes rich in ionizable functional groups, such as carboxylic and hydroxyl groups, which are responsible for the development of surface charge. At high pH, carboxylic (-COOH) and hydroxyl (-OH) get deprotonated to $–COO^-$ and $–O^-$ negative groups and become the source of electric charge causing the membrane to be negatively charged [93]. The more negative surface charge is proven to reduce fouling by both organic and inorganic materials in the water, which are mostly negatively charged, due to electrostatic repulsion [94,95].

Table 2.4. Contact angle and zeta potential of unmodified PES and graphene-based nanocomposite membranes

Membranes	Contact Angle	Zeta Potential (mV) at pH 6.5
Unmodified PES	65.2° ± 1.8	-20.7 ± 1.6
GNP 0.05 wt.%	63.3° ± 0.7	-22.2 ± 0.7
GNP 0.1 wt.%	61.6° ± 1.0	-22.5 ± 0.8
GNP 0.2 wt.%	56.9° ± 1.1	-23.1 ± 1.0
GO 0.05 wt.%	58.6° ± 0.6	-25.1 ± 1.9
GO 0.1 wt.%	51.1° ± 0.9	-28.0 ± 0.6
GO 0.2 wt.%	43.8° ± 1.0	-29.7 ± 2.3
GONR-L 0.05 wt.%	57.5° ± 1.0	-24.2 ± 1.4
GONR-L 0.1 wt.%	51.8° ± 1.1	-26.8 ± 1.6
GONR-L 0.2 wt.%	45.6° ± 0.4	-28.6 ± 2.3
GONR-H 0.05 wt.%	59.2° ± 1.2	-22.7 ± 1.2
GONR-H 0.1 wt.%	56.0° ± 0.9	-24.4 ± 0.8
GONR-H 0.2 wt.%	50.2° ± 1.6	-23.2 ± 1.4

2.3.6 Permeability of membranes

The pure water flux of unmodified PES membrane and nanocomposite membranes with 0.1 wt.% loading of nanofillers, as a function transmembrane pressure, is shown in Figure 2.6a. The slopes in this figure indicate the hydraulic permeability of the membranes. As can be seen, incorporating 0.1 wt.% of all graphene nanofillers has led to the higher water permeability than pristine PES membrane. This improvement can be attributed to the improved surface hydrophilicity (Table 2.5) by the incorporation of more hydrophilic hydroxyl groups to the surface [96]. The nanocomposite membrane prepared by GONR-L was found to provide the maximum hydraulic permeability of 1.30 LMH/psi.

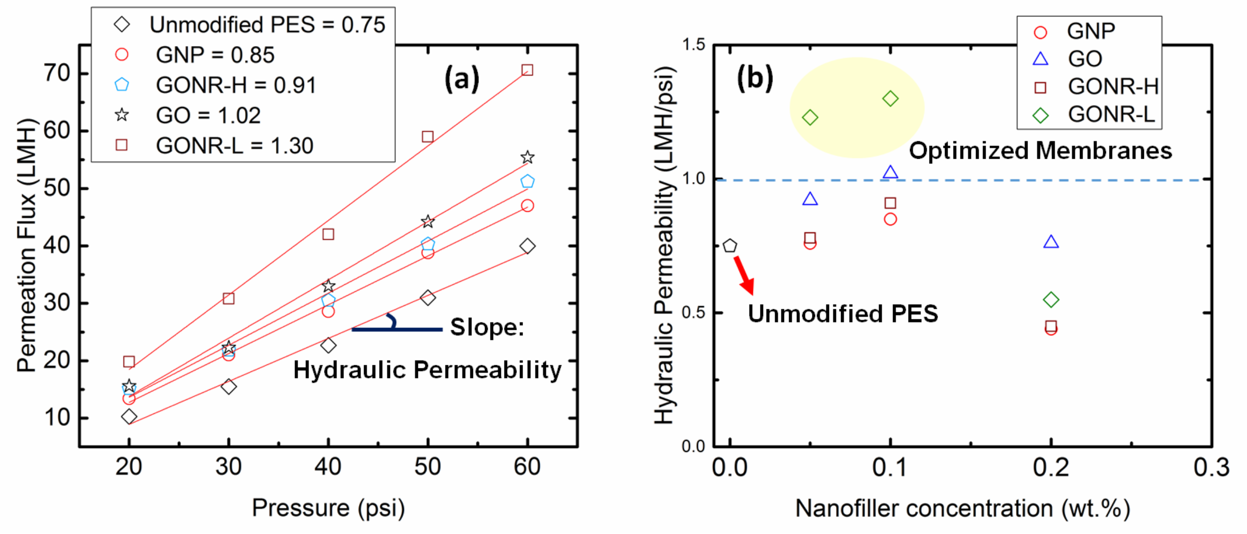

Figure 2.6. (a) Pure water flux vs pressure for unmodified PES membrane and nanocomposite membranes prepared by 0.1wt. % GO derivative nanofillers (the slope represents hydraulic permeability of membranes), (b) hydraulic permeability of membranes as a function of nanofillers loading in membrane

The effect of nanofillers concentration on the hydraulic permeability of membranes is shown in Figure 2.6b. Hydraulic permeability data in this figure are extracted from flux vs. pressure graphs as presented in Figure A3 in Appendix A. As can be seen in Figure 2.6b, increasing the concentration of nanofillers up to 0.1 wt.% increased the water permeability, however, further increase up to 0.2 wt.% decreased the water permeation, significantly, to even less than that of unmodified PES membrane. Theoretically, the porosity of phase inversion membranes is influenced by a trade-off between thermodynamic enhancement and kinetic hindrance of the casting solution [97]. The addition of hydrophilic nanofillers to polymer solution induces thermodynamic instability. The thermodynamic variation enhances the demixing rate of solvent and non-solvent in the casting solution, thus leading to the formation of more porous structures, whereas the rheological variation induces the opposite trend. A significant increase in the viscosity of casting solution (Figure A2 in Appendix A) by the addition 0.2 wt.% nanofillers has led to the delayed demixing of solvent and non-solvent and thus formation of denser structures due to the dominant role of the kinetic hindrance. This implies the presence of an optimum loading of nanofillers for improving the water flux.

It is worth mentioning that the addition of higher concentration of nanofillers not only affects the overall porosity of the membrane but also changes the thickness and morphology of skin layer which is mainly responsible for the permeation properties of membranes. In the present study, another reason for the significant decrease in the water flux by the addition of 0.2 wt.% nanofillers can be due to the notable increase in the thickness of skin layer (FESEM images in Figure 2.4).

2.3.7 Porosity of membranes

Figure 2.7 shows overall porosity of nanocomposite membranes. By the addition of a low quantity of graphene-based nanofillers up to 0.1 wt.%, the overall porosity is initially increased, then reduced by further addition of the nanofillers up to 0.2 wt.%. This behavior is also reported by other researchers [84,98,99]. Incorporation of hydrophilic nanofillers at low content into the polymer matrix could enhance amorphous nature of membranes; together with the rapid exchange of DMAc and water in NIPS process, the overall porosity of nanocomposite membrane increases [90]. This trend is consistent with the water flux results that showed a convex profile with increasing nanofillers. In addition, incorporation of hydrophilic nanofillers increases the thermodynamic instability of casting solution in the coagulation bath which leads to an accelerated solvent and nonsolvent exchange and large pore formation [97]. In the case of high nanofillers loading, the mean pore size decreased (Figure A4 in Appendix A) because of an apparent increase in the viscosity of the polymer solution. As mentioned earlier, increased viscosity causes a delay in demixing and thus suppresses the formation of large pore size.

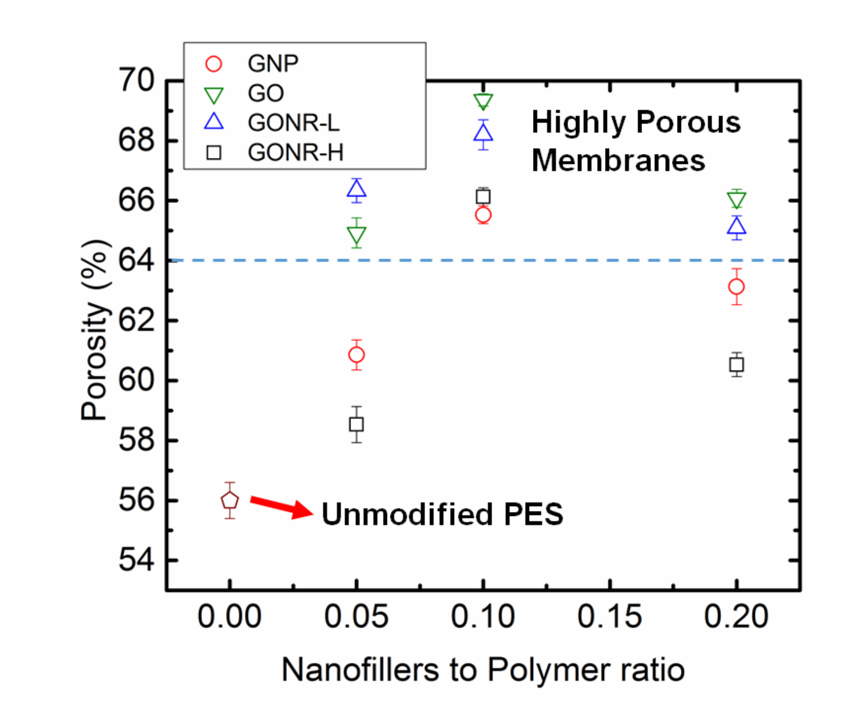

Figure 2.7. Membranes porosity in the different loading of graphene-based nanofillers.

2.3.8 Separation performance of membranes

The separation performance of synthesized membranes was evaluated by filtration of PEG solution and WLS inlet water. 250 mg/L solutions of PEG with a nominal average molar mass of 35,000 g/mol with the mean molecular diameter [100] of 8.92 nm was filtered, and concentration of PEG in permeate was measured using TOC analyzer. The rejection results are presented in Table 2.5. WLS inlet filtration results show superior performance of nanocomposite membranes for the removal of organic matter from oil sands produced water. The rejection increased from 43% to more than 50% for all GO-based nanocomposite membranes. Based on the data presented in Figure 2.4 and Table 2.5, the addition of 0.1 wt.% GONR-L has maximized both water flux (70 LMH at 60 psi) and TOC rejection (59%). PEG rejection results confirm that the molecular weight cut-off (MWCO) of modified membranes is about 35 kDa [97].

Table 2.5. WLS inlet and PEG rejection by graphene-based nanocomposite membranes

Membranes	WLS inlet Rejection (%)	PEG (Mw=35000 g/mol) Rejection (%)
Unmodified PES	43	86
GNP 0.05 wt.%	47	88
GNP 0.1 wt.%	49	90
GNP 0.2 wt.%	51	90
GO 0.05 wt.%	57	92
GO 0.1 wt.%	58	97
GO 0.2 wt.%	55	96
GONR-L 0.05 wt.%	55	88
GONR-L 0.1 wt.%	59	92
GONR-L 0.2 wt.%	57	94
GONR-H 0.05 wt.%	50	90
GONR-H 0.1 wt.%	50	91
GONR-H 0.2 wt.%	52	91

2.3.9 Fouling characteristics of membranes

The fouling behavior of the graphene-based nanocomposite membranes and unmodified PES membrane during filtration of WLS inlet water is presented in the Figure 2.8. Experiments were conducted at the same initial flux to investigate the effect of induced surface properties by graphene nanofillers on flux decline. Constant initial flux ensures a constant permeation drag for all experiments and thus fouling intensity can be attributed to surface properties like hydrophilicity and surface charge [95]. Also, all membranes were compacted at higher pressure before filtration test to make sure that the flux decline over time is just due to the fouling phenomenon [54].

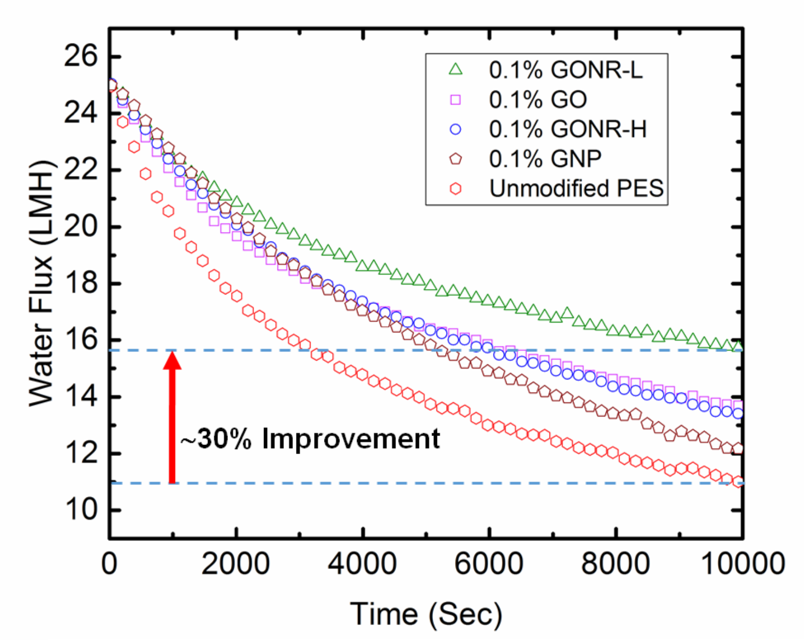

Figure 2.8. Flux vs. time of nanocomposite membranes and unmodified PES membrane due to fouling by WLS inlet water, compared at the same initial flux

As can be observed in Figure 2.8, the flux decline in graphene-based nanocomposite membranes was less than unmodified PES membranes. After 160 min filtration, GONR-L membrane showed 30% more water flux than pristine PES membrane (16 LMH compared to 11 LMH) that demonstrate its antifouling property for the filtration of WLS inlet water. This result can be attributed to higher hydrophilicity and more negatively charged surface of GONR-L (Table 2.4) that mitigated fouling through electrostatic repulsion and reduced hydrophobic interaction mechanisms.

Fouling behavior of a membrane is controlled by several parameters such as membrane surface properties (e.g., zeta potential and hydrophilicity), feed solution chemistry (e.g., ionic strength, and pH) and hydrodynamic of membrane modules [101,102]. In this research to investigate membrane surface properties, the latter two parameters and temperature were kept similar during experiments. It is generally accepted that the membrane with higher hydrophilicity and more negative surface charge are more resistant to fouling owing to fewer interactions among the polar groups on the membrane surface and the functional groups of the dissolved organic compounds in the feed. A possible explanation is that the formation of hydrogen bonding among the surface hydrophilic groups and water molecules forms a water layer on membrane surface that could impede membrane-foulant attachment [96,103]. Also, organic matter in the fluids tested are mostly hydrophobic [104] and, therefore are less inclined to attach to a hydrophilic surface due to the smaller hydrophobic interaction between fouling material and membrane surface. The combination of the hydrophilic surface of graphene-based nanocomposite membranes along with their high surface potential made them less inclined to fouling by suspended organic matter, which may be beneficial for oil sands produced water treatment.

Water flux recovery ratio (FRR), total flux decline ratio (DR_t), irreversible fouling ratio (DR_{ir}), and reversible fouling ratio (DR_r) for the base and 0.1 wt.% graphene-based nanofillers/PES membranes are depicted in Figure 2.9. All membranes showed flux decline during filtration of WLS inlet water for 1 hour which was likely due to deposition of organic and inorganic materials on the surface of membranes. However, the irreversible flux reduction due to strong adsorption of foulants on the surface and pores of the membranes was decreased for graphene-based nanocomposite membranes (GO: 9.3%, GONR-L: 10%, GNP: 19%, GONR-H: 19%) in comparisons with unmodified PES membrane (24%). The flux decline of graphene-based nanocomposite membrane was 14% less than the unmodified PES membrane at the same condition. Also, GO/PES and GONR-L/PES membranes indicated 14% more flux recovery ratio than the unmodified PES membrane, implying an enhancement in antifouling characteristics of the base membrane by the incorporation of GO and GONR-L nanofillers. However, FRR enhanced only 4% after the addition of GNP and GONR-H which might be due to the lack of oxygen functional groups on GNP surface.

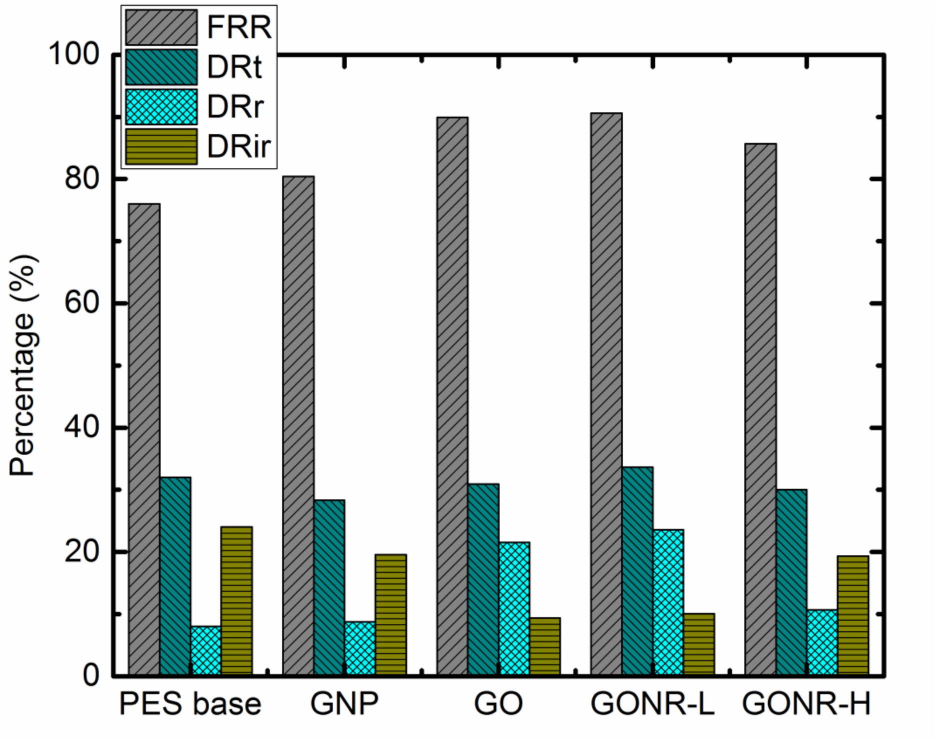

Figure 2.9. Comparison of the fouling characteristics of PES/ Graphene-based nanofillers membranes and unmodified membrane. DRt is total flux decline ratio, DRr is reversible flux decline, DRir is irreversible flux decline ratio, and FRR is flux recovery ratio.

2.4 Conclusions

In this study, graphene oxide derivatives with different shapes and oxidation states were incorporated into a polymeric membrane matrix via NIPS technique. The surface properties of the fabricated membranes have significantly changed in terms of hydrophilicity and surface charge. The contact angle and streaming potential measurements demonstrated the fabrication of more hydrophilic and negatively charged PES/GO nanocomposite membranes. All graphene-based nanocomposite membranes showed better water flux and rejection of organic matter than unmodified PES membrane. The addition of graphene nanofillers, up to 0.1 wt.%, first enhanced the water flux due to an increase in overall porosity and hydrophilicity of the membranes, then further increase of nanofillers loading decreased the flux more likely due to the formation of a thicker skin layer. The optimum loading to improve both water flux and rejection of organic matter was found to be 0.1 wt.%. The graphene-based nanocomposite membranes were found to have an MWCO of ~35 kDa and removed 50% of dissolved organic matter from SAGD produced water. Fouling propensity of membranes was tested with SAGD WLS inlet water. The results show that by the addition of graphene nanofillers the fouling tendency of the membranes has hindered due to improved surface properties. GONR-L at its optimum loading (0.1 wt.%) has provided the maximum water flux (70 LMH at 60 psi), TOC rejection (59%) and antifouling properties (30% improvement compared to pristine PES membrane). The flux recovery ratio (FRR) experiments have confirmed significant improvement in the antifouling property of PES/GO nanocomposite membranes.

Chapter 3

Study on antifouling behaviors of GO modified nanocomposite membranes through QCM-D and surface energetics analysis

3.1 Introduction

Water-use efficiency calls for swift and effective technological progress in water recycling and wastewater treatment methods. Water treatment via membrane technology has become one of the most promising methods due to some distinct advantages over conventional methods such as higher product quality, more compact design, and lower operating costs. The major challenge that inhibits more practical application of membrane technology is the fouling of membranes. Membrane fouling, which is caused by the deposition of foulant materials onto the membrane surface or within its pores, decreases water flux, shortens membrane lifespan, and consequently leads to a higher operating cost [5]. Fouling can be classified as colloidal, organic, biofouling, and minerals scaling. The focus of this study is organic fouling.

Surface characteristics play an important role in organic fouling behavior of a membrane by a variety of mechanisms including hydrophobic interactions, hydrogen bonding, van der Waals forces, and electrostatic interactions between organic foulants and membrane material. Therefore, membrane surface modification by different methods such as chemical grafting [67,105,106] plasma treatment [69,107,108], and physical blending of hydrophilic nanofillers [77,109–111] with polymer has been suggested for mitigation of organic fouling. Although all these methods have shown a considerable improvement in the overall antifouling characteristic of host membrane, the employed method to assess the membrane's hydrophilic properties could not still represent a clear picture of this phenomenon. In all these studies, the hydrophilic characteristics of membranes have been evaluated through water contact angle measurement and correlated with membrane fouling propensity. However, further investigations have shown that surface hydrophilicity, being assessed by only water contact angle, cannot represent the non-electrostatic and polar interactions existing between foulants and membrane [112–118]. To account for the effect of these interactions on membrane fouling, it is necessary to conduct a more sophisticated surface energetics analysis. Taking into account that all these three important interaction energies including acid-base (AB), Lifshitz-van der Waals (LW), and electrostatic double layer (EDL) through extended Derjaguin-Landau-Verwey-Overbeek (DLVO or known as XDLVO) theory provide more realistic information about the interfacial interaction between foulant and membrane. XDLVO can also provide free energy of interaction which is considered as a quantitative estimation of surface hydrophilicity [113]. Brant et al. [112] used XDLVO to assess short-ranged membrane-colloid interactions to describe colloidal fouling of reverse osmosis (RO) membranes. He followed van Oss approach [119] to combine Lewis AB interactions with Lifshitz-van der Waals and electric double layer interactions. Subramani et al. [120,121] and Wang et al. [122,123] combined the use of XDLVO theory with models of interfacial hydrodynamic interactions, particularly, the drag force exerted by water permeation, to explain initial attachment mechanism of microbial particles onto membranes. In another research, XDLVO theory was employed to study the effects of colloidal interactions on the flux of skim milk in cross-flow tubular ceramic membranes [124]. In classical DLVO theory, LW and EDL interactions are considered, but the AB component, which describes repulsive hydration effects and attractive hydrophobic interactions was added in the extended version. Hence, the XDLVO theory offers a more precise approach to understand the intermolecular interactions between foulants and membrane surface [112].

This study aims to understand the reason that exists behind the reduced fouling propensity of the synthesized PES-PVP-GO nanocomposite membrane in comparison with the pristine PES membrane during an ultrafiltration process. Having a planar two-dimensional structure which is abundantly covered by hydrophilic oxygen containing functionalities, graphene oxide (GO) has been listed as one of the best candidates to cease organic fouling on membrane. It is stated in the literature that natural organic matter in water can be treated as colloidal particles and thus its adsorption on the membrane surface could be well described by interfacial hydrodynamic and XDLVO interactions [122]. In addition, to evaluate the adsorption of foulants on the surface of membranes, real wastewater (boiler feed water (BFW) of Steam assisted gravity drainage (SAGD) operation) was tested using quartz crystal microbalance with dissipation monitoring (QCM-D). The QCM-D is a very sensitive technique which has been used to detect nanoscale changes of surface mass [124]. Study on surface crystallization kinetics is one of the main applications of QCM-D, which could be translated into scaling in membrane science [125]. The physiochemical properties of the foulant and membrane dictate the extent of organic adsorption on membranes. Therefore, the synthesized membranes were also characterized by contact angle analyzer, zeta potential measurement, Fourier transform infrared spectroscopy (ATR-FTIR) and atomic force microscopy (AFM).

3.2 Materials and Methods

3.2.1 Chemical and reagents

PES (polyethersulfone, Ultrason E6020P with molecular weight (Mw) = 58 kDa) was obtained from BASF and was used as the main polymer to fabricate membranes. Graphene oxide (GO) was purchased from Angstron Materials with specific surface area ≥ 400 m^2/g. Diiodomethane 99% was purchased from Acros Organics, and humic acid and glycerol (99%) were acquired from Sigma-Aldrich. Sodium dodecyl sulfate (SDS, 99% purity, Sigma-Aldrich Co., USA) was used to clean the crystal sensors, QCM-D camber, and connecting tubes. Helmanex III solution (2 vol %) at pH 11.7 was used as a detergent for cleaning the immersion beaker. Helmanex solution, ammonium hydroxide (25 vol %) hydrogen peroxide (30 % w/w), potassium chloride (KCl), sodium chloride (NaCl), polyvinylpyrrolidone (PVP, Mw = 360 kDa) and N,N-dimethylacetamide (DMAc) were all purchased from Fisher Scientific. All chemicals were used as received without more purification. The industrial wastewater used to evaluate adsorption on the thin film coated sensors was SAGD boiler feed water (BFW) which was provided from a SAGD water treatment plant located in the Athabasca oil sands region of Alberta.

3.2.2 Membrane fabrication

Three UF membranes, pristine PES, PES-PVP, and PES-PVP-GO, were fabricated via nonsolvent-induced phase separation (NIPS) method [77,110,111]. Homogeneous polymer solutions were first prepared by dissolving the materials listed in Table 3.1 in DMAc solvent. For fabrication of PES-PVP-GO membranes, first GO nanosheets were uniformly dispersed in DMAc solvent using a probe sonicator, then PVP and PES were added, and the mixture was stirred for one day. After stirring, the homogenous solution was rested for 24 hours to eliminate the air bubbles from the solution. Subsequently, the solution was cast on the flat surface as a thin film using a film applicator (Gardco, MICROM II). In the last step, the cast film was immersed in a water container and left in water for a day to complete membrane formation by phase inversion. All membranes were stored in ultrapure water at 23 ˚C after preparation. The molecular weight cut off (MWCO) of the synthesized PES, PES-PVP, and PES-PVP-GO was 40, 37, and 35 kDa, showing a smaller pore size of graphene-based nanocomposite membrane.

Table 3.1. Chemical composition of all fabricated membranes in this study via NIPS method

Membranes	PES (wt %)	PVP (wt %)	GO (wt %)
PES	18	0	0
PES-PVP	18	2	0
PES-PVP-GO	18	2	0.1

3.2.3 Representative organic waste

To evaluate the fouling of fabricated membranes listed in Table 3.1, QCM-D experiments were conducted on BFW of SAGD operation. The concentration of contaminants in the BFW was analyzed by ICP-OES (Thermo Scientific, iCAP™ 7400, Massachusetts, USA) and TOC analyzer (Shimadzu, model TOC-V; detection range 3–25,000 mg/L, Kyoto, Japan) and the results are presented in Table 3.2. It was reported that a significant fraction of organic carbon existing in BFW of SAGD operation composes of humic acids [104,126]. To simplify the calculation of total energy of interaction we used humic acid as the main foulant in BFW.

Table 3.2. Properties of BFW which was used as a feed solution.

Parameters	BFW
pH	8.85
TOC (mg/L)	340
TDS (mg/L)	1310
Conductivity (µS/cm)	2049
Na^+ (mg/L)	400
Si(mg/L)	0.162
Mg^{2+} (mg/L)	0.44
Ca^{2+} (mg/L)	3.90
Iron, total (mg/L)	187.8

3.2.4 Membrane topography

The roughness of the fabricated membranes was evaluated by AFM (Dimension edge, Bruker Nano Surface, USA). The average roughness (R_a), root-mean-square roughness (R_q), and maximum roughness (R_m) were utilized to compare the surface roughness of membranes quantitatively. The structural morphology of the fabricated membranes was examined using field emission scanning electron microscopy (FESEM). The dried membranes samples were fractured under liquid nitrogen and were mounted on SEM stub. To improve electron conductivity of all the membrane samples, they were coated with a thin film of chromium (8nm) using Nanotek SEMprep 2 sputter coater. The cross-sectional images were taken at 10 kV and high vacuum condition.

3.2.5 XDLVO theory

The XDLVO theory was used to determine the interaction energetics between different membrane surfaces and foulants. In this approach, the surface energy parameters of membrane and foulants must be determined experimentally by performing contact angle measurements on membranes and fouled membrane using three probe liquid of known surface tension properties.

It is suggested by van Oss [119] that the total interaction energy between the membrane and foulant immersed in water (U^{XDLVO}) can be evaluated by the sum of Lifshitz-van der Waals (U^{LW}), acid-base (U^{AB}), and electrostatic (U^{EL}) interaction energies as follows:

$$U^{XDLVO} = U^{EL} + U^{LW} + U^{AB} \tag{3.1}$$

These components of the total interaction energy are calculated by the following equations [112].

$$U^{EL} = \pi \varepsilon_r \varepsilon_0 a_f \left(2\xi_f \xi_s ln\left(\frac{1 + e^{-\kappa d}}{1 - e^{-\kappa d}}\right) + \left(\xi_f^2 + \xi_s^2\right) \ln\left(1 - e^{-2\kappa d}\right) \right) \tag{3.2}$$

$$U^{LW} = 2\pi \Delta G_{d_0}^{LW} \frac{a_f d_0^2}{d} \tag{3.3}$$

$$U^{AB} = 2\pi a_f \lambda \Delta G_{d_0}^{AB} e^{(d_0 - d)/\lambda} \tag{3.4}$$

In the above equations, ε_r represents the dielectric permittivity of suspending fluid (=78.9 for water), ε_0 is vacuum permittivity (8.85 ×10^{-12} C^2/J/m), a_f is the radius of foulant, κ is the inverse Debay length, ξ_f is the foulant surface potential, ξ_s is the membrane surface potential, d is the separation distance between membrane and foulants, d_0 is the minimum separation distance of 0.158 nm [119], λ is the decay length of acid-base interactions (0.6 nm in aqueous media) [127], $\Delta G_{d_0}^{LW}$ is the Liftshitz-van der Waals free energy, $\Delta G_{d_0}^{AB}$ is the acid-base interaction free energy element at the separation distance of d_0 which could be calculated by the following equations [112,128].

$$\Delta G_{d_0}^{LW} = 2(\sqrt{\gamma_l^{LW}} - \sqrt{\gamma_s^{LW}})(\sqrt{\gamma_f^{LW}} - \sqrt{\gamma_l^{LW}}) \tag{3.5}$$

$$\begin{gathered}\Delta G_{d_0}^{AB} = 2\sqrt{\gamma_l^+}\left(\sqrt{\gamma_s^-} + \sqrt{\gamma_f^-} - \sqrt{\gamma_l^-}\right) + 2\sqrt{\gamma_l^-}\left(\sqrt{\gamma_s^+} + \sqrt{\gamma_f^+} - \sqrt{\gamma_l^+}\right) \\ -2(\sqrt{\gamma_s^+\gamma_f^-} + \sqrt{\gamma_s^-\gamma_f^+})\end{gathered} \tag{3.6}$$

where γ^{LW}represents the LW component, γ^+ is the electron acceptor, and γ^- is the electron donor components, and the subscripts s, l, f denote solid (membrane), liquid, and foulants, respectively.

By replacing subscript of “s” instead of “f” in the above equations, ΔG_{sls}^{AB} and ΔG_{sls}^{LW} could respectively be calculated for membrane-membrane interaction. If two identical surfaces are considered, the sum of $\Delta G_{sls}^{LW}$and ΔG_{sls}^{AB} is the interfacial free energy of cohesion, while if two dissimilar surfaces are studied, the sum of $\Delta G_{d_0}^{LW}$and $\Delta G_{d_0}^{AB}$ is the interfacial free energy of adhesion (ΔG^{AD}). Therefore, ΔG_{sls}^{CO} could be defined as free energy of cohesion between two similar surfaces like membrane-membrane or foulant-foulant as following:

$$\Delta G_{sls}^{CO} = -2\left(\sqrt{\gamma_s^{LW}} - \sqrt{\gamma_l^{LW}}\right)^2 + 4(\sqrt{\gamma_s^+\gamma_l^-} + \sqrt{\gamma_s^-\gamma_l^+} - \sqrt{\gamma_s^+\gamma_s^-} - \sqrt{\gamma_l^+\gamma_l^-}) \tag{3.7}$$

κ value, representing the inverse Debye length, can be obtained using the following equation [112]:

$$\kappa = \sqrt{\frac{e^2 \sum n_i z_i^2}{\varepsilon_r \varepsilon_0 kT}} \tag{3.8}$$

where e is the fundamental electric charge (1.6×10^{-19} C), n_i is the number concentration of ion i in the bulk solution, z is the balance of ion i, k is Boltzmann's constant (1.38×10^{-23} J/K), and T is absolute temperature. The Young–Dupre equation [129] is used to relate the contact angle (θ) of a liquid on a membrane surface to the surface tension of the liquid, solid and foulant. In this study, a background electrolyte of 10 mM NaCl was used.

According to van Oss, the total surface tension γ^{TOT} for any medium is sum the of the nonpolar (Lifshitz-van der Waals, γ^{LW}) and polar (acid-base, γ^{AB}) components. The polar AB element is to explicitly include surface tension component due to hydrogen bonding [130]. γ^{TOT} is expressed by the following equation [128,131].

$$\gamma^{TOT} = \gamma^{LW} + \gamma^{AB} \tag{3.9}$$

The polar AB element consists of an electron acceptor and an electron donor parameter [131–135] and is given by the following equation [136]:

$$\gamma^{AB} = 2\sqrt{\gamma^{+}\gamma^{-}} \tag{3.10}$$

The surface tension parameter of membrane ($\gamma_s^{LW}, \gamma_s^{+}, \gamma_s^{-}$) can be evaluated by measuring sessile drop contact angle using three probe liquids with known surface tension parameters ($\gamma_l^{LW}, \gamma_l^{+}, \gamma_l^{-}$) and using the extended Young equation [137]:

$$\gamma^{TOT}(1 + \frac{cos\theta}{r}) = 2(\sqrt{\gamma_s^{LW}\gamma_l^{LW}} + \sqrt{\gamma_s^{+}\gamma_l^{-}} + \sqrt{\gamma_s^{-}\gamma_l^{+}}) \tag{3.11}$$

$$r = 1 + SAD \tag{3.12}$$

where θ is the equilibrium contact angle and r is the Wenzel's roughness ratio that accounts for the increase in the surface area because of roughness. The SAD is surface area difference that could be driven from AFM results. The surface tension components are used to measure the free energy of cohesion for membrane-membrane and foulant-foulant materials and the free energy of adhesion for membrane-foulant.

3.2.6 Contact angle measurement

All contact angle measurements were carried out based on the sessile drop method using goniometer Kruss Model DSA 100E (Hamburg, Germany). The probe liquids being selected for this study were ultra-pure water, glycerol, and diiodomethane. It is necessary that two of these liquids be polar (water, glycerol) and one be apolar (diiodomethane) [112]. The apolar probe liquid was employed to find the nonpolar component (γ^{LW}) of surface tension whereas the polar liquids gave the acid-base (γ^{AB}) component. The properties of probe liquids are shown in Table 3.3.

Table 3.3. Surface tension properties (mJ/m2) of probe liquids at 20˚C (Data was taken from van Oss [127])

Probe liquids	γ^{LW}	γ^{+}	γ^{-}	γ^{AB}	γ^{TOT}
Ultra-pure water	21.8	25.5	25.5	51.0	72.8
Glycerol	34.0	3.9	57.4	30.0	64.0
Diiodomethane	50.8	0.0	0.0	0.0	50.8

3.2.7 Zeta potential measurement

The surface zeta potential of the membranes was measured using Surpass3 analyzer (Anton Paar, Graz, Austria). This device measures the surface zeta potential based on streaming potential measurement. Measurements were conducted using a 0.001 M KCl solution at 25 °C and over pH range of 4-9. The zeta potential of foulants in BFW was also determined by using an electrophoretic light scattering spectrophotometer (Nano-ZSP Zetasizer, Malvern Instruments, Worcestershire, UK). This device measures the zeta potential based on the laser Doppler electrophoresis method. Electrophoretic mobility was evaluated with a background of 0.01M KCl solution at four pH values (4.0, 7.0, 8.80, 10). Zeta potential was calculated from measured electrophoretic mobility using the Smoluchowski equation. A detailed description of the measurement procedure is provided elsewhere [112].

3.2.8 Fouling experiments protocols

To explore fouling propensity of membranes in cross-flow filtration setup, a three-step experimental protocol was followed. First, we determined the pure water flux, J_{W1}. For the next step, the water flux during filtration of BFW, J_{Wf}, was measured. The surface of membrane was washed with deionized water for 30 min to removed loose adsorbed foulants from the surface, and then the pure water flux of cleaned membrane was recorded for the second time, J_{W2}. To evaluate the fouling resistance characteristics of the membranes the total fouling ratio (DR_t) and flux recovery ratio (FRR) were calculated as follows [82]:

$$FRR = \frac{J_{W2}}{J_{W1}} \tag{3.13}$$

$$DR_t = 1 - \frac{J_{Wf}}{J_{W1}} \tag{3.14}$$

Here, DR_t is the summation of reversible fouling ratio (DR_r) and irreversible fouling ratio (DR_{ir}), which are related to the flux decline because of the adsorption of foulant materials on a membrane surface. DR_r and DR_{ir} can be calculated by the following equations:

$$DR_r = \frac{(J_{W2} - J_{Wf})}{J_{W1}} \tag{3.15}$$

$$DR_{ir} = 1 - \frac{Jw_2}{Jw_1} \quad (3.16)$$

3.2.9 QCM-D measurements

Quartz crystal microbalance with dissipation monitoring (QCM-D) was employed to measure the dynamic adsorption behavior of organic matter in the SAGD produced water on pure PES, PES-PVP and PES-PVP-GO membranes. The working principle of QCM-D technology is based on applying an AC voltage across a quartz crystal, immersed in the aqueous solution, in order to excite it to oscillate at a fundamental resonate frequency of 4.95 MHz. Due to the piezoelectric effect of quartz crystal, a decreasing resonance frequency corresponds to a proportional mass adsorbed on the sensor surface. The thickness, density, and viscoelastic properties of the adsorbed layer can be determined by monitoring the frequency change and energy dissipation shift of the recorded response [138–140]. The response sensitivity to mass change is 0.5 ng/cm^2. QCM-D device used in the present work (Q-sense, Gothenburg, Sweden) can measure simultaneous changes in resonance frequency (Δf) and dissipation (ΔD) of accumulated organic matter on the quartz sensors. The Au-coated quartz sensors were covered by a thin film of PES or PES-PVP-GO using a spin coater (SCS, G3P-15, Indianapolis, USA). A peristaltic pump (ISMATEC, ISM831, Wertheim, Germany) supplied a steady flow of 0.15 ml/min of the solutions over the polymer-coated quartz sensor.

The surface properties of the QCM-D sensors are crucial for the interaction of sample material with the surface. Thus, the use of the proper process for cleaning and surface preparation is necessary to obtain reproducible measurements. First, sensors were sonicated in DMAc (solvent for polymer coating) for 15 min to remove polymer film from the surface; then the manufacturer recommended cleaning procedures were followed. UV/ozone cleaning process was employed for 10 min to remove organic contaminants residue from the surface using UV/ozone ProCleaner instrument (BioForce Nanosciences Inc.). Next, the sensors were immersed in an ammonium peroxide solution (1:1:5 mixture of ammonium hydroxide (25%), hydrogen peroxide (30%), and MilliQ water) at 75 ˚C for 5 min. The sensors were rinsed with adequate MilliQ water and finally dried with pure nitrogen gas.

3.2.9.1 QCM-D sample preparation

The QCM-D sensors can be coated with any material that can firmly attach to their surface and make an ultrathin layer. To prepare a solution for spin-coating, the homogenous casting solutions of pure PES, PES-PVP, and PES-PVP-GO was initially diluted ten times with DMAc, and the solutions were stirred for 24 h to prepare homogenous polymer solutions having 2 wt.% polymer (PES or PES-PVP or PES-PVP-GO) content. The prepared solutions were then spin-coated on a previously cleaned quartz crystal sensor at 419 rad/s (4000 rpm) for 100 seconds. Finally, the sensor was left for 4 hours at room temperature until the solvent evaporated completely, and the dried thin polymer film was formed. The spun coated PES sensors were mounted into the flow module chamber. Before each measurement, the chamber was initially flushed with Milli-Q water to get a stable baseline. The signal was considered stable when the frequency change was less than ±1 Hz over 10 mins.

3.3 Results and discussion

3.3.1 Physicochemical characteristics of the composite membranes

3.3.1.1 Surface and cross-section morphology

To observe the effect of the addition of PVP-GO on the composite membrane structure, the FESEM images of cross-section morphologies of all composite membranes are presented in Fig. 3.1. We observed that all membranes have asymmetric morphology with a dense skin layer on top and porous finger-like macrovoids underneath which is a typical structure of NIPS membranes. Based on Fig. 3.1, by incorporation of hydrophilic additives, the thickness of membrane decreased from 106 μm in the pristine PES membrane to 94 μm and 88 μm in PES-PVP and PES-PVP-GO membrane, which could be attributed to acceleration in the exchange rate of solvent (DMAc) and nonsolvent (water) during phase inversion [91,141]. Hydrophilic additives have the propensity to increase the thermodynamic instability of casting solution, therefore, promoting the demixing and make solidification faster [142]. On the other hand, by the addition of hydrophilic additives like GO, the thickness of whole membrane may decrease, but the thickness of skin layer increases. This was ascribed to an increase in the polymer solution viscosity which reduced the phase inversion rate on the top surface and as a result led to a thicker skin layer. In the case of PES-PVP-GO membrane, the color of top layer is light grayish while its bottom layer color is white, implying the migration of more hydrophilic material toward the top layer during NIPS process before the membrane becomes solidified.

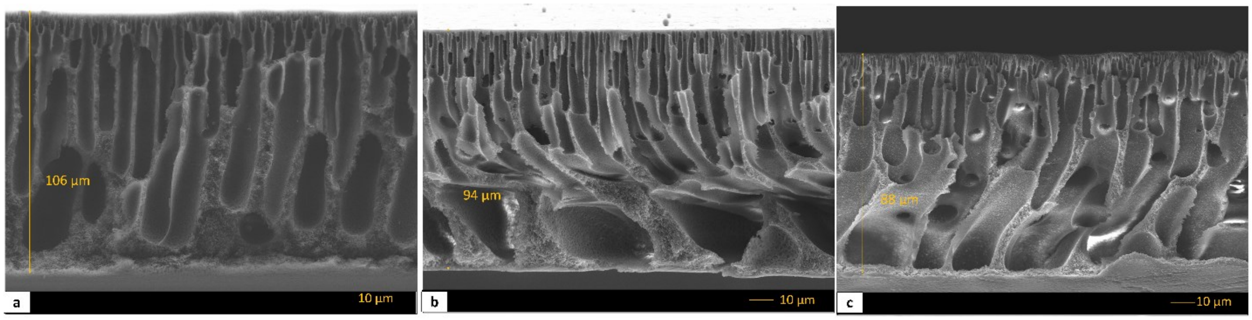

Figure 3.1. Cross-section FESEM images of (a) PES, (b) PES-PVP, and (c) PES-PVP-GO membranes, as well as magnified skin layer of (d) PES, (e) PES-PVP, and (f) PES-PVP-GO membranes

3.3.1.2 Surface roughness of membranes

2D and 3D AFM topographic images of fabricated membranes are presented in Fig. 3.2 to evaluate membrane surface roughness. The AFM scan rate was 5 μm/s for all the measurements. The AFM measurements were performed on four different spots over each membrane sample and the average was reported with standard deviation in Table 3.4. The AFM images and the provided information in Table 3.4 show that by the addition of either PVP or GO nanosheets, the surface roughness parameters of membranes increased. Although no clear correlation between the surface roughness and PVP concentration was found in the literature (since it changes with the Mw and concentration of PVP in the casting solution) in most studies, roughness decreased mainly due to the higher migration rate of hydrophilic PVP toward water [143,144]. The same observation was reported for hydrophilic nanomaterials such as GO [74].

The average roughness parameter (R_a), root mean square of roughness (Rq), and maximum roughness (R_{max}) were doubled in PES-PVP membrane as compared to PES membrane. As mentioned before, hydrophilic additives increases rate of demixing during the phase inversion process. In such condition, casted polymer faces very quick changes like temperature quench, resulting in less interaction of polymer molecules with non-solvent phase (water). Therefore, polymer chains start clustering in some regions which enhance membrane surface roughness [145]. Surface area difference (SAD) values in Table 3.4 show that PVP-GO modified membrane had 30.2% higher surface area compared to pristine PES membrane.

3.3.1.3 Surface composition of membranes

ATR-FTIR results of fabricated membranes are presented in Fig. 3.3. The transmittance peak at 3440 cm^{-1} is ascribed to OH stretching vibration of carboxylic groups existing in GO nanostructures. The peaks at 3102 cm^{-1}, 3068 $cm^{-1,}$ and 2922 cm^{-1} wavenumbers are ascribed to C-H stretching vibration that exists in PES main backbone, GO, and PVP additive. The characteristic peak at 1650 cm^{-1} is also assigned to C=O vibration of carboxylic groups that presents in both PVP and GO structures [146]. The peak at 1620 cm^{-1} is attributed to C=C in benzene rings in PES and GO structure. As it can be easily seen, the intensity of this peak in

PES-PVP-GO membrane increased very sharply. The oxygen-containing functional groups on GO can make hydrogen bonds with added PVP. In such condition, more PVP chains could remain within the final membrane structure after phase inversion step. Furthermore, GO nanostructures have some carboxylic groups that can improve FTIR absorption intensity to some extent.

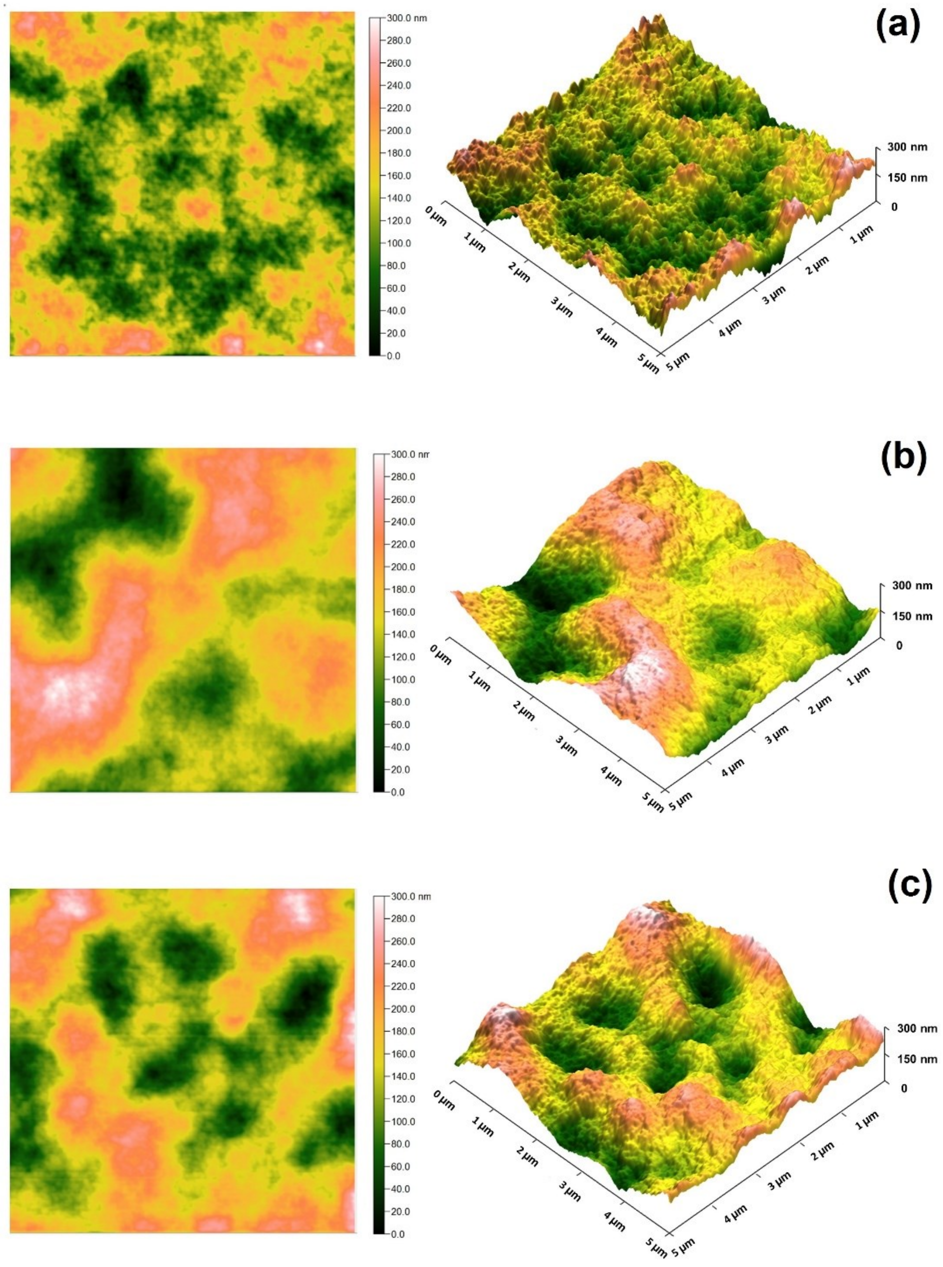

Figure 3.2. 2D and 3D AFM topographies of a) PES, b) PES-PVP, and c) PES-PVP-GO membranes.

Table 3.5. Ra, Rq, Rmax, and SAD% of fabricated membranes

Membrane	R_a (nm)	R_q (nm)	R_{max} (nm)	SAD %
PES	6.62 ± 0.37	5.25 ± 0.23	51.85 ± 8.8	0.37 ± 0.04
PES-PVP	17.57 ± 3.72	14.14 ± 3.2	124.5 ± 28.4	0.44 ± 0.08
PES-PVP-GO	17.5 ± 1.66	14.0 ± 1.33	121.0 ± 12.0	0.53 ± 0.02

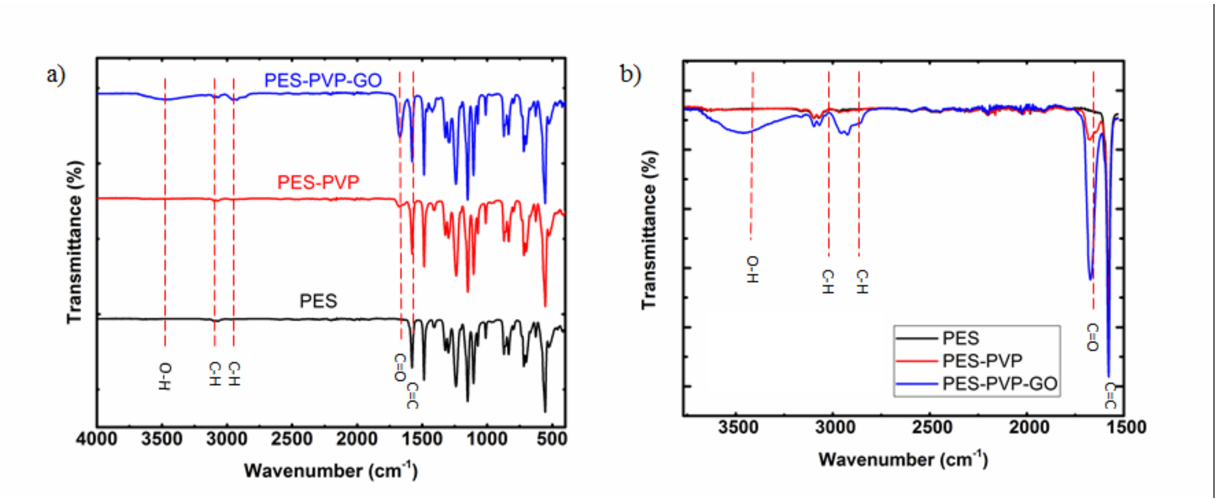

Figure 3.3. FTIR spectra of PES, PES-PVP, PES-PVP-GO membranes a) wavenumber 500 to 4000 b) wavenumber 1500 to 3800

3.3.1.4 Pure water permeability of membranes

The pure water flux of PES, PES-PVP, and PES-PVP-GO membranes versus transmembrane pressure was compared to illustrate the influences of incorporation of PVP and GO on physicochemical properties of the membranes. The slopes in this figure show the hydraulic permeability of the membranes. It could be observed from Fig. 3.4(a) that incorporating 0.1 wt.% GO has led to a higher water permeability in PES-PVP-GO (0.3 L/m^2 h kPa) than PES-PVP (0.28 L/m^2 h kPa) and pristine PES (0.22 L/m^2 h kPa) membrane. This enhancement in flux can be attributed to the decreased thickness of membranes (FESEM images in Fig. 3.1) and more importantly, improved hydrophilicity of membranes, originating from the incorporation of more hydrophilic GO into the nanocomposite membrane, as presented in Table 3.5 [96]. It is worth noting that for all membranes, the permeation fluxes do not go through the origin, indicating a resistance against permeation flux up to a certain pressure. However, water passes through the PES-PVP-GO nanocomposite membrane at lower transmembrane pressure as compared to pristine PES and PES-PVP membranes, more likely due to its higher hydrophilicity. Porosity and mean pore size of the membrane are other influential factors which should be considered. Higher porosity and large mean pore size facilitate more water passage in a determined time step, resulting in higher water permeability. According to our previous study [111], the addition of 0.1 wt% of GO improved membrane porosity more than 23%, while the mean pore size miniaturized approximately 15%. Also, adding GO to the casting solution increased the thickness of the skin layer. Given that, the increase in the water permeability can be primarily attributed to a significant increase in membrane hydrophilicity.

3.3.1.5 Separation performance of membranes

The separation performance of fabricated membranes was determined by filtration of BFW of SAGD operation as feed solution (see properties in Table 3.2) and measurement of organic matter concentration in feed water and permeate using TOC analyzer. The rejection results are displayed in Fig. 3.4(b). BFW filtration results exhibit superior performance of nanocomposite membranes for the removal of organic matter from oil sands produced water. The dissolved organic matter in the SAGD produced water has a wide range of molecular weight [126]. Our fabricated UF membranes were able to remove 40-60% of organic matter present in BFW with a higher molecular weight than 35 kDa [111].

The rejection increased from 48.12% for PES to 54.48% for the GO-based nanocomposite membrane. Based on the data presented in Fig. 3.4(a) and 3.4(b), the addition of 0.1 wt. % GO has maximized both water flux (75 LMH at 207 kPa) and TOC rejection (54.48%). A possible explanation for the improved rejection is that the addition of GO nanofillers slows down the solvent/nonsolvent exchange rate in the coagulation bath and thus reduced the pore size of membranes [111]. Also, migration of GO additive to the skin layer leads to the formation of thicker skin layer [111]. On the other hand, the hydrophilicity of the membrane increased significantly by the addition of GO, which has led to the higher permeation flux.

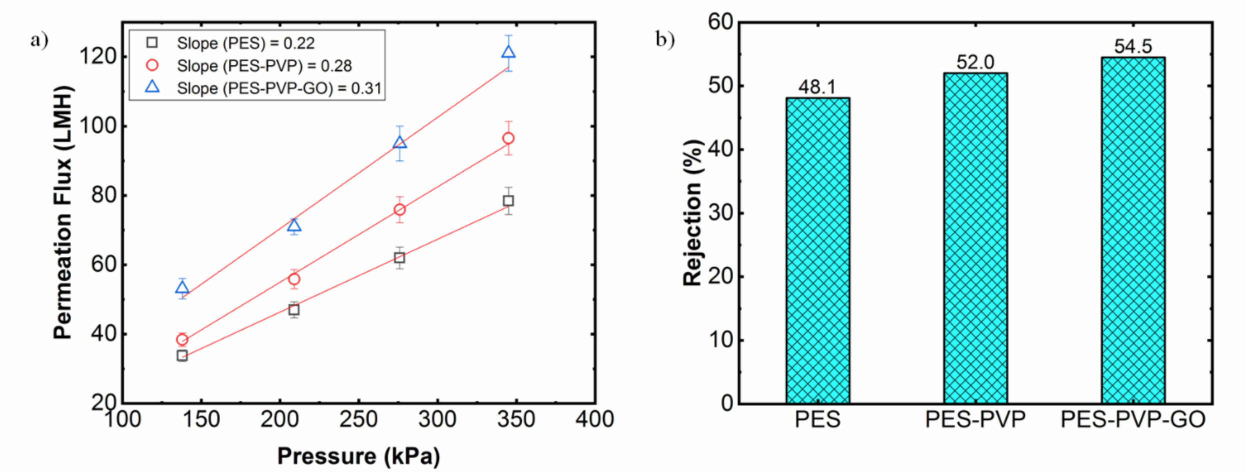

Figure 3.4. (a) Pure water flux vs pressure for PES, PES-PVP, and PES-PVP-GO membranes (the slope represents hydraulic permeability of membranes and (b) rejection of organic matter in BFW (TOC rejection) by membranes. The error bars represent the standard deviations from average water flux values.

3.3.1.6 Surface charge and contact angle measurement results

The surface charge and contact angle of synthesized membranes are presented in Table 3.5. The measured surface zeta potential of pristine PES at pH 6.5 was -17.4 mV. Since the PES does not contain ionic functionals. The adsorption of solution anions on the polymeric surface, like Cl^- or hydroxide, is mainly responsible for the observed negative zeta potential [147]. By GO nanofillers addition, ionizable functional groups become abundant at the membrane surface. These functional groups include carboxylic (–COOH) and hydroxyl (–OH) groups, which are accountable for the formation of more negative surface charge. At high pH, –COOH deprotonated to $–COO^-$, giving negative functional groups [31]. The point of zero charge for all

PES membranes in this research was in the range of 2-3. The more negative surface charge is verified to lower fouling tendency of the membrane via more electrostatic repulsion effect [95,148]. Based on the sessile drop method, probe liquids with a volume of 5 µl were placed on the surface of membranes, and the contact angle was measured after 3 s. Higher contact angle reveals the more hydrophobic surface. It must be mentioned that it is reported that material is considered hydrophilic if it produces a pure water contact angle less than about 45° degrees [137]. Fig. 3.5 shows the zeta potential of organic matter in BFW (in mV) at different pH values. As can be observed, the organic matter in BFW became more negatively charged as pH increased.

Table 3.5. Zeta potential and contact angle for PES nanocomposite membranes

Membranes	Zeta Potential (mV) at pH 6.5	Contact angle (water)	Contact angle (Glycerol)	Contact angle (Diiodomethane)
PES	-17.4 ± 1.4	78.1 ± 1.6	50.1 ± 0.5	11.9 ± 0.7
PES-PVP	-20.7 ± 1.6	67.6 ± 0.7	55.9 ± 1.2	28.9 ± 1.1
PES-PVP-GO	-28.0 ± 0.6	51.2 ± 1.2	61.9 ± 0.6	39.3 ± 1.1

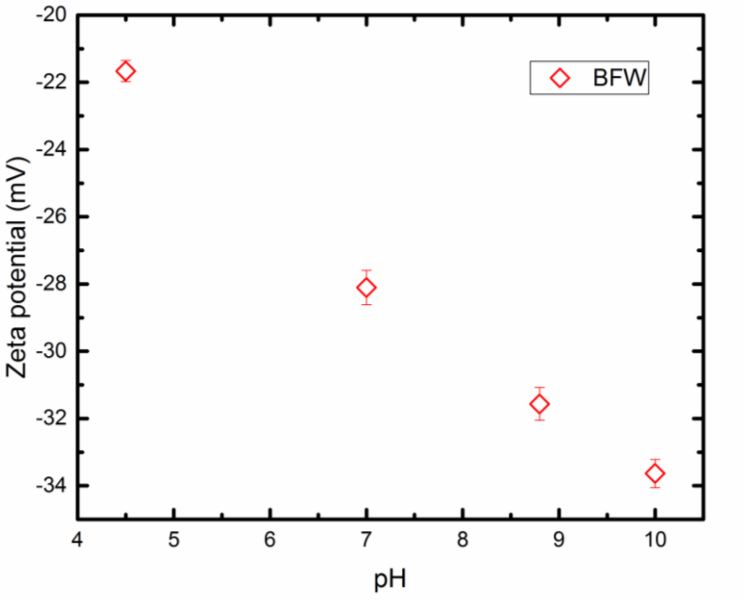

Figure 3.5. Zeta potential of organic matter in BFW at different pH

3.3.2 XDLVO analysis results

The initial buildup of foulants on a membrane is mainly governed by the interfacial free energy of adhesion between foulant and membrane (membrane-foulant interactions) which is presented in Table 3.6. After the formation of the first layer of foulant, the deposition of more layers will be governed by the foulant-foulant interaction (interfacial free energy of cohesion). According to Table 3.6, although foulants in BFW have attractive interfacial free energies of adhesion with all synthesized membranes in this study, its values decreased by the addition of PVP and PVP-GO. The free energy of adhesion decreased significantly from -28.55 mJ/m^2 for pristine PES membrane to -6.73 mJ/m^2 for the PES-PVP-GO nanocomposite membranes.

Table 3.6: Interfacial free energy of adhesion (mJ/m2) between membranes and foulants upon contact

Parameters	$\Delta G_{d_0}^{LW}$	$\Delta G_{d_0}^{AB}$	$\Delta G_{d_0}^{AD}$
PES	-7.55	-21	-28.55
PES-PVP	-6.39	-12.29	-18.67
PES-PVP-GO	-5.24	-1.49	-6.73

Table 3.7 presents the measured surface tension parameters, as well as the free energy of cohesion of membranes. It could be observed that all membranes have high γ^{LW}in comparison with γ^{AB}, implying the strong apolar characteristics of the synthesized membranes. By the addition of PVP and GO; however, the γ^{LW} value decreased and at the same time the polar component γ^{AB} increased. For instance, the presence of 0.1 wt.% GO in PES-PVP-GO increased the polar component (γ^{AB}) from 1.73 mJ/m^2 to 16.41 mJ/m^2, promoting the polar characteristics of the synthesized nanocomposite membrane. The Lifshitz- van der Waals (LW) and acid-base (AB) components of the surface free energy were calculated using equations 5-7. The free energy of cohesion, ΔG_{sls}^{CO}, is the summation of LW and AB surface free energy components and describes the interaction free energy (per unit area) when two surfaces of the same material (e.g.,

membrane-membrane, foulant-foulant) submerged in a medium (water in this study), brought into contact with each other. These values imply the stability of a material submerged in a liquid medium. If the free energy is positive, the material is considered stable (hydrophilic in case immersing liquid is water) and when the free energy value is negative it is thermodynamically unstable (hydrophobic characteristics) [137]. The free energy of cohesion provides quantitative assessment for the hydrophilicity/ hydrophobicity of the membrane and foulants. The more negative the ΔG_{sls}^{CO}, the stronger is the hydrophobic characteristics. In this study, ΔG_{sls}^{CO} is -77.49 mJ/m^2 for PES as compared to -21.08 mJ/m^2 for PES-PVP-GO nanocomposite membrane, implying that the addition of GO made the nanocomposite membrane less hydrophobic and improved the free energy of cohesion of the nanocomposite membrane. In this study, the value of ΔG_{sls}^{AB} is larger than the value of ΔG_{sls}^{LW}, suggesting that the contribution of acid-base free energy component was more notable in comparison with Lifshitz- van der Waals free energy component.

Table 3.7. Surface tension parameters and cohesion free energy (mJ/m2) of membranes and foulants

Membranes	Surface tension parameters					Cohesion free energy		
	γ^{LW}	γ^{+}	γ^{-}	γ^{AB}	γ^{TOT}	ΔG_{sls}^{LW}	ΔG_{sls}^{AB}	ΔG_{sls}^{CO}
PES	49.71	1.58	0.47	1.73	51.44	-11.34	-66.15	-77.49
PES-PVP	44.68	3.21	4.23	7.37	52.05	-8.12	-39.01	-47.13
PES-PVP-GO	39.97	5.03	13.39	16.41	56.38	-5.47	-15.61	-21.08
Foulant:								
Humic acid in BFW	41.33	0.87	45.20	12.57	53.91	-6.20	27.55	21.35

The membrane fouled with humic acid of BFW has demonstrated much higher electron donor (γ^{-}) component than electron acceptor (γ^{+}) one. Previous studies [128,137] have shown that surfaces fouled by organic matter (here with BFW organics) have higher γ^{-}than γ^{+} values due to inherent negative charge of organic materials. The ΔG_{sls}^{CO} for foulant (humic acid of BFW) is

21.35 which is a positive value demonstrating that humic acid is thermodynamically stable in BFW. Since, the free energy of interactions are inversely proportional to surface tension [137], fouling is anticipated to be higher for a surface with a relatively higher surface free energy component.

Fig. 3.6 shows the profiles of interaction energies with the separation distance from membrane surface –foulant flocs combination. The surface tension parameters of the humic acid solution with 10 mM NaCl concentration at pH 7.0 were used to calculate the total energy of interaction, U^{XDLVO}, between the organic compound and different PES membranes at varying separation distance. As mentioned before, the main constituent of BFW is humic acid with the average molecular size is about 6 nm [149,150]. Furthermore, the conductivity of BFW is about 2,000 μS/cm that can be relatively represented by 10 mM NaCl solution. Lifshitz-van der Waals interaction (U^{LW}) is short-ranged and attractive. Electrostatic interaction (U^{EL}) is long-ranged and since all membranes and foulant are negatively charged, the U^{EL} interaction is repulsive. U^{EL} interaction is dominant for longer separation distance.

Fig. 3.6 demonstrates that, for all synthesized membrane, when the organic molecules approach the membrane surface (as close as 20 nm), they would experience repulsive interaction. As it is shown in Fig. 3.6, among three different interaction components (U^{AB}, U^{LW}, and U^{EL}), AB interaction (U^{AB}) is the most determining factor of the total energy of interaction (U^{XDLVO}) when the separation distance is less than 5 nm. According to Fig. 3.6(d), PES-PVP-GO demonstrated the highest energy barrier against adsorption of an initial layer of foulants. When the energy barrier is higher, the foulants fail to overcome it easily and thus the initial adsorption is more difficult to occur. By the addition of GO to the membrane, the interaction barrier becomes larger, meaning that the synthesized nanocomposite membranes had more fouling resistance.

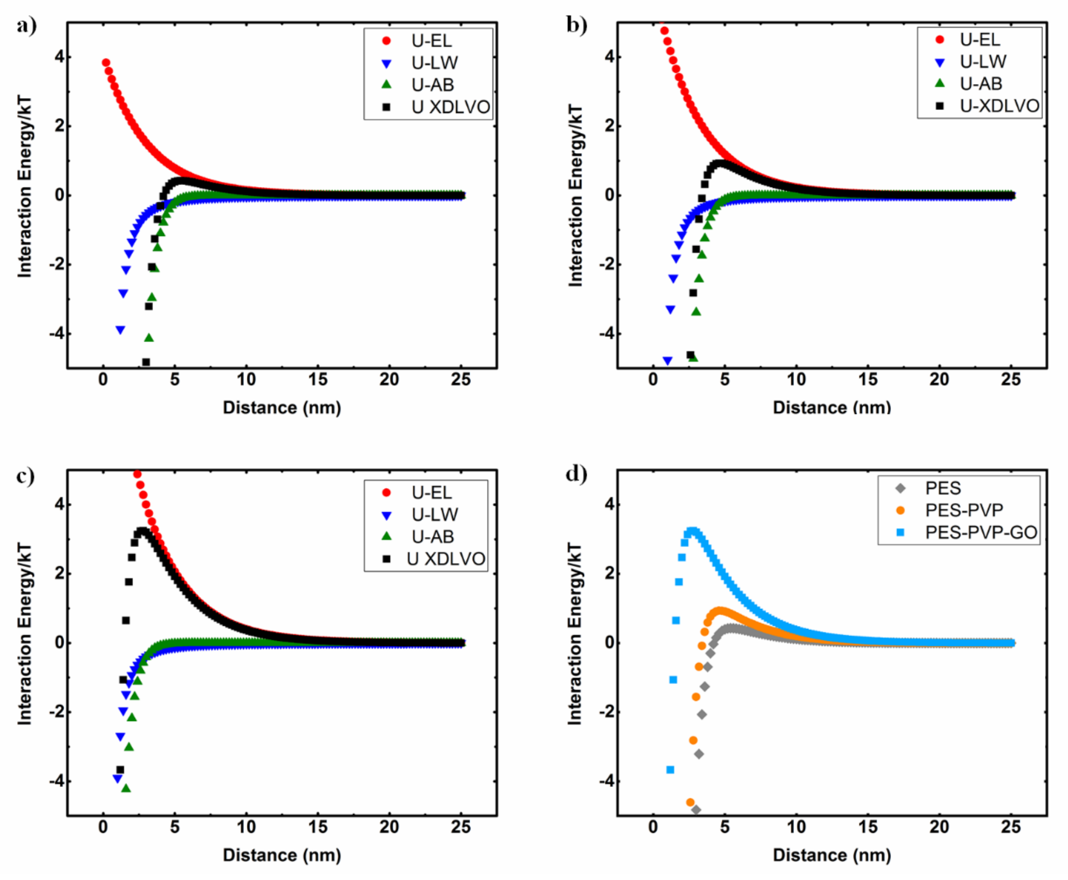

Figure 3.6. The profiles of interaction energies with separation distance from the membrane surface for a) PES, b) PES-PVP, and c) PES-PVP-GO. Panel d) compares XDLVO energies of interaction for PES, PES-PVP, and PES-PVP-GO membranes.

3.3.3 Flux recovery ratio (FRR)

Several parameters that affect fouling on a membrane are membrane surface characteristics (e.g., hydrophilicity, roughness, and zeta potential), hydrodynamic of the membrane module, and feed solution chemistry (e.g., pH and ionic strength) [101,102]. In this work, to explore the effect of membrane surface characteristics on fouling, temperature and the latter two parameters were maintained constant. It is broadly recognized that a membrane with higher hydrophilicity and more negative surface charge has less tendency to develop fouling due to fewer interactions among the functional groups of the dissolved organic compounds in the feed solution and the polar groups on the membrane surface. A reasonable justification could be a layer of water molecules could be established on the membrane surface as a result of hydrogen bonding between the surface hydrophilic groups and water molecules that slow down the attachment of foulants to the membrane surface [96,103]. In addition, the majority of organic matters in the analyzed wastewater are predominantly hydrophobic [104]; thus they have less tendency to adsorb on a hydrophilic surface on account of a smaller hydrophobic interaction with the membrane surface. The combination of the high surface charge and the more hydrophilic surface of the graphene-based nanocomposite membrane (PES-PVP-GO) made the surface less prone to fouling by suspended organic matter, which could be favorable for the treatment of oil sands produced water. It's worth mentioning that the increased roughness of membranes by the addition of PVP and GO (AFM results in Fig. 3.2 and Table 3.5) tends to increase the fouling due to the entrapment of foulants (here humic acid) in the eddy zones generated behind the peaks [95,151]. However, the adverse effect of roughness is countered by the improved hydrophilicity and surface charge.

The fouling behavior of the PES, PES-PVP, and PES-PVP-GO membranes during cross-flow filtration of BFW at the same transmembrane pressure (275 kPa) is shown in Fig. 3.7(a). All membranes were compacted at higher pressure before filtration test to make sure that the flux decline over time is just due to the fouling phenomenon. As can be observed in Fig. 3.7(a), the flux decline in PES-PVP-GO membrane was less than PES and PES-PVP membranes. This result can be ascribed to higher hydrophilicity and more negatively charged surface of GO-PVP modified membrane that reduced fouling through electrostatic repulsion and reduced hydrophobic interaction mechanisms. In addition, the XDLVO curve (Fig. 3.6d) shows a higher maximum for PES-PVP-GO membrane than other membranes, implying less tendency of organic matter to adhere to the membrane surface.

After 1 hour filtration of BFW, the membranes were washed with pure water for 1 hour, and then the second pure water permeation flux was measured. Water flux recovery ratio (FRR), total flux decline ratio (DR_t), reversible fouling ratio (DR_r) and irreversible fouling ratio (DR_{ir}), of the synthesized membranes are presented in Fig. 3.7(b). It can be observed that PES, PES-PVP, and PES-PVP-GO membranes experienced flux reduction during 1 h filtration of organic matter in BFW because of organic and inorganic materials accumulation on the surface of membranes. Nonetheless, the irreversible flux decline, as a result of strong adsorption of foulants on the surface, and inside the membranes pores was reduced for GO nanocomposite membrane (25.3%) in comparison with the pristine PES (72.6%) and PES-PVP membranes (36.3%). Comparing at the same condition, the flux reduction of PES-PVP-GO was 37% less than the PES. In addition, PES-PVP-GO provided 47% and 11% more FRR than PES and PES-PVP, respectively, indicating an improvement in fouling resistance characteristics of the base membrane by the addition of GO nanofillers. Finally, the fouling test results are found to be in good agreement with the XDLVO theory that showed less fouling tendency of GO-modified membranes to fouling by organic matter in BFW.

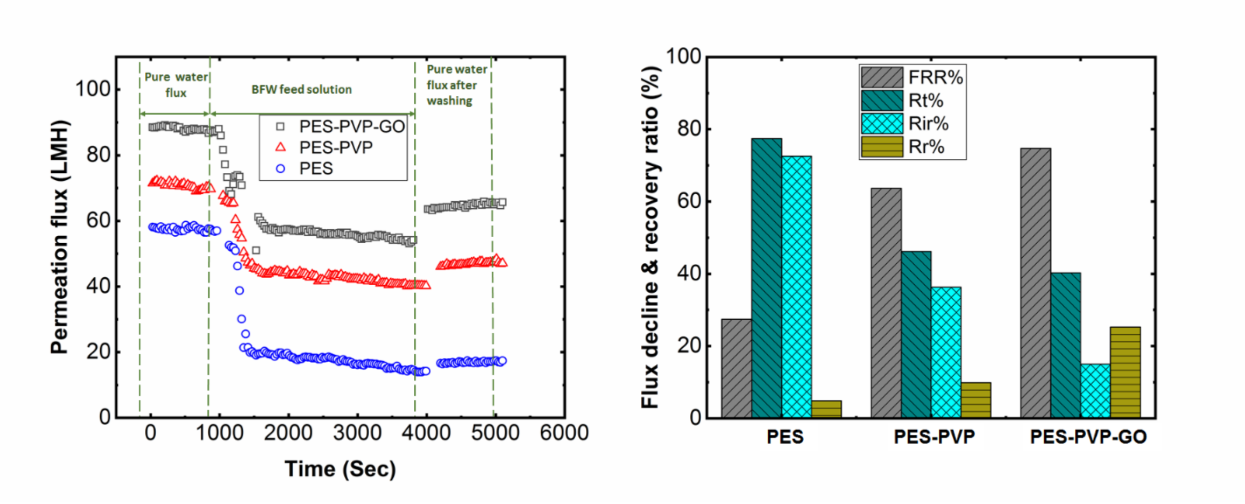

Figure 3.7. (a) Fouling of PES, PES-PVP, and PES-PVP-GO membranes by organic matter in BFW over time and (b) Comparison of the fouling characteristics membranes. DRt is total flux decline ratio, DRr is reversible flux decline, DRir is irreversible flux decline ratio, and FRR is flux recovery ratio.

3.3.4 QCM-D

QCM-D was used to investigate the dynamic adsorption of organic matter in BFW of SAGD operation on PES, PES-PVP, and PES-PVP-GO membranes. After finding the resonance frequencies for the dry QCM-D sensor in the air, Mili-Q DI water was pumped through the system at a flow rate of 150 µL/min and 25 °C. The volume above the sensor was 40 µL, which provided a residence time of 16 seconds and the Reynolds number over the sensor was 0.5 (creeping flow). Therefore, it can be assumed that there was no slip between the adsorbed molecule and polymer coated crystal due to creeping flow over the sensor during QCM-D experiments. In this study, all the organics samples were first filtered by 0.45 µm syringe filter prior to injection. After obtaining a stable baseline for DI water, a background solution of 0.01 M NaCl and BFW solution were respectively supplied over the sensor at an identical temperature and flow rate.

As displayed in Fig. 3.8, when the foulant solution was injected into the chamber, the frequency of all crystal sensors decreased immediately due to the mass adsorption on the coated polymer surface. Subsequently, the observed sharp declining trends were decelerated, representing saturation of adsorptive sites over polymeric coating. The frequency of the sensor which was spin-coated with PES-PVP-GO polymer solution showed a maximum decline, implying the highest deposition of foulant, which is unexpectedly inconsistent with the XDLVO theory and fouling experiment results. According to the XDLVO analysis and filtration tests, the order of attractive interaction energy between organic matter and membranes as well as flux decline (total, reversible, and irreversible) was PES-PVP-GO < PES-PVP < PES. This means that, although the interaction energy barrier is higher, the polymer thin film (membrane) is still more inclined for foulant adsorption when GO and PVP were added. Similar inconsistent behavior was also reported in the literature [128]. One reason for such observations could be different flow regimes and applied pressure that exists between membrane cross-flow filtration chamber (laminar flow, Re ~ 800, 275 kPa) and QCM-D sensor chamber (creeping flow, Re = 0.5, atmospheric pressure).

At lower flow rates, the impacts of electrostatic forces and hydrophobic interactions on the fouling behavior of studied membranes become more significant [152]. In such condition, surface functionality and solution composition are the predominant factors controlling initial adsorption rate [153]. PES-PVP-GO membrane with abundant oxygen-containing functional groups, being originated from deposited GO, can be easily coated by divalent cations of the solution such as Ca^{2+} and Mg^{2+} (see the analysis results of BFW in Table 3.2). It is also reported that among different functional groups, -COOH has the fastest adsorption kinetics [124]. Afterward, negatively charged organic compounds can make another coating layer over this positive wall. The next bilayers could be created either by electrostatic or hydrophobic attraction forces. In addition, the surfaces of membranes fabricated by phase inversion and spin coating are different in terms of surface composition and surface roughness, which is mainly due to a different distribution of GO at the membrane surface using these two methods.

Apart from flow rate effects, the physical surface properties of the studied membranes in QCM-D and filtration tests are different. In the cross-flow filtration tests, a permeable porous membrane was used while the QCM-D experiments were done over a non-permeable sensor surface. By applying transmembrane pressure in filtration tests, water is forced to pass through the membrane, forming a denser layer of water at the initial stage of filtration as compared to the QCM-D cell. This aqueous layer acts as a barrier which prevents attachment of organic matter to the membrane surface. Such beneficial circumstance is absent in the case of QCM-D sensor, thereby, higher hydrophilicity of QCM-D sensor coated by PES-PVP-GO could not have a considerable supportive impact on better antifouling performance.

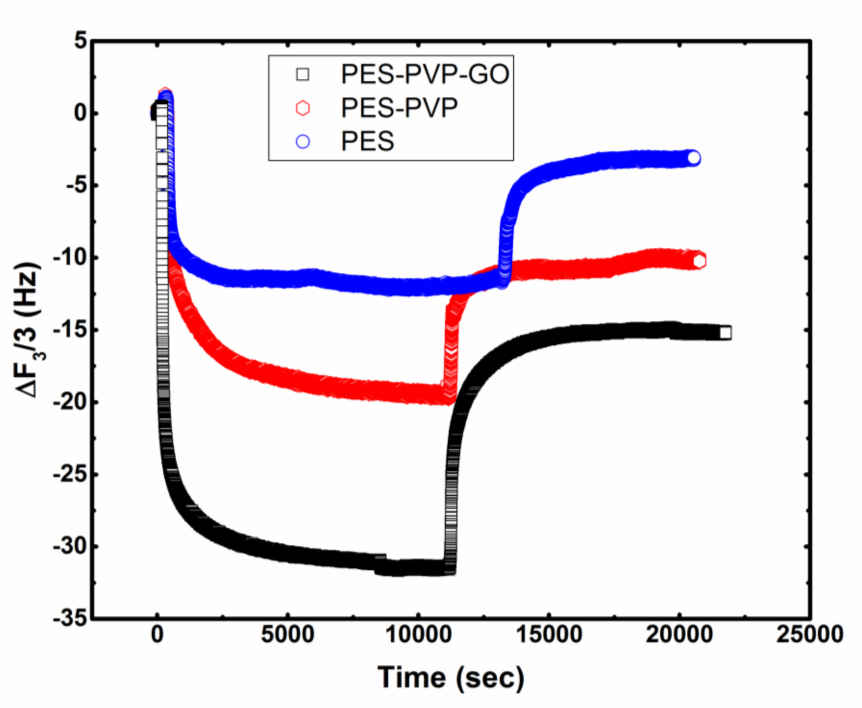

Figure 3.8. Representative frequency shifts by deposition of organic foulants in BFW of SAGD operation onto PES, PES-PVP, and PES-PVP-GO spin-coated on QCM-D crystal sensors

3.4 Conclusions

In this research, we studied the effects that incorporation of hydrophilic additives including PVP and GO can have on fouling behaviors of fabricated membranes through XDLVO analysis, fouling tests, and QCM-D techniques. . Our results showed that different additives can notably alter the surface property of membranes in terms of hydrophilicity and surface charge. The water and oil contact angle measurement results represented that two modified membranes with PVP and PVP-GO had higher hydrophilicity comparing to the pristine one. Beside hydrophilicity, roughness and surface charge of these modified membranes were also increased by the addition of PVP and PVP-GO. The fouling tests and XDLVO analyses demonstrated that among all membranes, PVP-GO modified membrane had the best antifouling performance. According to XDLVO results, all components of interfacial free energy of adhesion between membranes and foulants reduced after modifying membranes by PVP and PVP-GO, implying that the surfaces of these newly fabricated membranes had less tendency to fouling by organic matter. Using QCM-D technique, the adsorptive behaviors of different polymeric compositions of membranes were also studied. The QCM-D results were not in line with real fouling tests as well as XDLVO analyses in which PVP-GO modified membrane showed the highest equilibrium mass adsorption over QCM-D sensor. Fluid dynamics, as well as surface characteristics in QCM-D tests, were totally different compared to fouling tests that could be assumed as a possible reasons for such contrasting observations. Based on the obtained results and observations, the outlines of this study could be listed as following:

1- Assessment of surface enrgy parameteres in a membrane without considering to peripheral condition could not exactly indicate its actual fouling behavior.
2- XDLVO theory is a straightforward technique to investigate how effective adhesive forces between membrane and foulants can determine fouling tendency.
3- The results obtained from XDLVO theory could successfully predict the trends of different membranes working in the feed solutions with high fouling potential.

QCM-D, as a real-time technique for monitoring surface adsorption, is unable to provide information which are comparable with real fouling tests results.

Nomenclature	
a	radius
ε_r	permittivity of the suspending liquid (78.9 for water)
ε_0	vacuum permittivity (8.85×10^{-12} $C^2/J/m$)
κ	inverse Debye screening length
ξ	zeta potential
θ	contact angle
d	separation distance between membrane and foulants
d_0	minimum separation distance (0.158 nm)
λ	decay length of acid-base interactions (0.6 nm in aqueous media)
U	total interaction energy between membrane and particle
γ	surface tension
T	absolute temperature
e	electron charge (1.6×10^{-19} C)
n_i	number concentration of ion i in bulk solution
z_i	valence of ion i
k	Boltzmann's constant (1.38×10^{-23} J/K)
r	Wenzel's roughness
Superscripts	
AB	acid-base
LW	Lifshitz–van der Waals
EL	electrostatic
CO	cohesion
TOT	total
+	electron acceptor
-	electron donor
Subscripts	
f	foulant
l	liquid
s	solid (membrane)
sls	two surfaces of the same material submerged in a liquid

Chapter 4:

Anti-fouling Electro-conductive Thin Film Composite Membranes Fabricated by reduced Graphene Oxide-Polyaniline (rGO-PANI)

4.1 Introduction

Lack of adequate clean water threatens the life of up to 1.2 billion people worldwide [154]. Along with a drastic increase in demand, pollution of water by persistent soluble organic compounds and heavy metals have exacerbated water crisis. Water shortage has also negatively affected energy and food production, and thus hampered the continuous economic growth of both developing and industrialized countries. Given that, the only viable option for the sustainable growth of nations is to treat, recycle and reuse the industrial and residential effluents by energy- and cost-efficient methods [155].

Among many techniques being proposed so far, advanced oxidation processes (AOPs, i.e., Fenton reaction, ozone/UV, and photocatalysis) and membrane-based technologies are recognized as the most effective methods to remove water pollutants [156,157]. The largest wastewater reclamation plant with the initial capacity of 375000 m^3/day is implemented in Sulaibiya (Kuwait) recently, where water is purified through reverse osmosis (RO) and ultrafiltration (UF) techniques [158]. The AOP method has also applied practically for removal of pesticides by PWN water treatment plant in the north Netherland [159]. Depending on the type of AOP, it may suffer from many drawbacks, which restrict its feasible implementation in a large scale. Most of AOP systems are very energy- and cost-intensives and have the potential to produce some toxic byproducts [160]. On the other hand, membrane-based technologies offer several advantages over AOPs for large-scale applications such as compact modular design, low energy consumption, ease of operation, and high quality of the product in terms of purity [155]. However, fouling of membranes via mineral compounds [161], colloidal particles, dissolved organics [111], and microorganisms [162] restricted the widespread application of membranes.

In general, hydrophilicity, charge, and roughness of surface play the most crucial roles in overall fouling behavior of a membrane [77]. Owing to the formation of a dense layer of water over the hydrophilic membrane surface, the attachment of foulants can be inhibited considerably [163]. Furthermore, rougher surfaces are found to be more vulnerable to fouling as foulant can be easily entrapped in the eddy zones generating behind the peaks [95]. It is also reported that membranes with the negatively-charged surface could minimize deposition of negatively charged foulants through electrostatic repulsion [164]. Modification of membranes with nanomaterials [165], polymers with hydrophilic segment [166], and antibacterial agents [167,168] have been so far attempted to improve antifouling performance without sacrificing membrane permeation and selectivity rates. In recent years, researchers have investigated the use of responsive polymers to change the physicochemical properties of membranes[23,31]. The grafted responsive groups at the membrane surface change their conformation and surface charge upon a change in an external stimulus such as pH, ionic strength, electric potential, and temperature, which might reduce adsorption of solutes to the surface[169]. Despite promising results obtained in lab-scale, low physical stability of coated/grafted materials to the surface and massive use of chemicals has confined the application of membrane surface modification methods in practice [170]. Currently, stimuli-responsive membranes are vital components of advanced technologies such as sensors, protein detection kits, and drug delivery devices[171], and their application in water treatment certainly requires further exploration.

Electrically conductive membranes (ECMs), being made by a wide range of organic and inorganic materials, have demonstrated great potential in water purification [172,173]. Applying external potentials, the ECMs could take different electrical charges which are uniformly distributed over the surface of the membrane. The first aptitude of ECMs is their switchable surface charge, enabling them to repel oppositely-charged foulants through electrostatic repulsive forces [174]. Furthermore, electrochemical reactions, including anodic electro-oxidation (AEO) and cathodic electro-reduction (CER), may occur on the ECMs, which could partially or completely destroy the chemical structure of some foulants [59,175,176]. Biofilm formation over the surface of membrane, which causes biofouling, could also be prevented via AEO process on self-cleaning membrane [177]. During membrane scaling by inorganic foulants, primarily divalent ions, the electric field can facilitate the electrophoretic movement of ionic species and consequently disrupt local crystallization [178]. In a specific range of potentials, hydrogen or oxygen gasses could be generated over ECMs surface, contributing to the mitigation of membrane fouling through gas bubbling [179]. Carbon-based nanomaterials including carbon nanotube (CNT) [180,181] and reduced graphene oxide (rGO) [182,183], metals like Ni [184], as well as electro-conductive polymers such as polyaniline (PANI) [185,186] and polypyrrole (PPy) [187] were recently employed to develop ECMs. One of the bottlenecks of ECMs being made by solely carbon-based nanostructures is the low thin film stability under cross-flow filtration and high anodic potentials, deteriorating permselectivity of the membrane in a long-term operation [59,188]. High environmental stability and excellent anti-corrosive properties of PANI make it a promising candidate for improving the attachment of conductive carbon thin film on top of ECMs [59,189]. In this study, we developed a facile approach to fabricate robust stimuli-responsive membranes, which could reduce membrane fouling when subjected to an electric potential by combining the advantages of both AOP and membranes. We proposed a rapid and versatile method to prepare highly-rigid ECMs by simultaneous lamination of rGO and PANI onto polyethersulfone (PES) support. Using PANI, which served as a strong glue for the firm assembly of rGO to the PES surface, without significant sacrifice of rGO electrical conductivity, has resulted in robust and high-performance ECMs. The physicochemical characteristics of the fabricated ECMs were evaluated in terms of hydrophilicity, mechanical stability, and charge density. Afterward, fouling behavior of these membranes was systematically studied in both AEO and CER configurations using synthetic aqueous solutions of sodium alginate and real boiler feed water (BFW), taken from steam-assisted gravity drainage (SAGD) operation for bitumen extraction in Alberta, Canada.

4.2 Material & methods

4.2.1 Chemical and reagents

Commercial PES membrane of 0.1 μm pore size was obtained from Sterlitech Corporation and was used as support layer. N-Methyl-2-pyrrolidone (NMP), potassium permanganates, and H_2SO_4 were purchased from Fisher Scientific. Graphite powder and polyaniline (PANI) (emeraldine base, MW~65000 Da) were purchased from Sigma Aldrich. Synthetic solutions of sodium alginate (Acros Organics) and boiler feed water (BFW) of SAGD operation (Athabasca oil sands region of Alberta, Canada) were used for fouling tests.

4.2.2 Preparation of rGO

Graphene oxide was synthesized by oxidation of graphite powder according to modified Hummer method followed by exfoliation of graphene sheets by probe sonication. After multiple times washing, GO sheets were freeze-dried. Subsequently, reduced graphene oxide (rGO) was synthesized by thermal reduction at 1000 °C under pure N_2 atmosphere.

4.2.3 Membrane fabrication

Stock solutions of PANI in NMP: DI water (W_{NMP}:$W_{DI\ water}$ = 1:4) and rGO in DI water were prepared through 1 h sonication. An appropriate amount of each solution was mixed in a dead-end filtration cell and it was allowed to pass through microporous PES substrate under nitrogen gas pressure. The compositions that were used to prepare all membranes are summarized in Table 1. The concentration of PANI in all membrane was 0.5 mg which was initially dispersed in 40 ml of NMP. rGO was dispersed in 160 ml of DI water.

Table 4.1. Chemical composition of laminated layer

Membranes	PANI (mg)	rGO (mg)	PANI: rGO
ECM1	0.5	0	1:0
ECM2	0.5	1	1:2
ECM3	0.5	2	1:4

4.2.4 Representative organic waste

To evaluate the fouling resistance of the fabricated membranes listed in Table 4.1, we conducted filtration test using sodium alginate synthetic solution (50 ppm, 5 mM NaCl), as well as real BFW waste of SAGD operation.

Table 4.2. Properties of BFW samples of SAGD operation

Parameters	BFW Water
pH	8.8
TOC (mg/L)	300
TDS (mg/L)	1310
Conductivity (μS/cm)	2049
Na^+ (mg/L)	470
Si (mg/L)	0.16
Mg^{2+} (mg/L)	4.8
Ca^{2+} (mg/L)	6.00
Fe^{2+} (mg/L)	2.1

The sodium alginate solution was prepared by mixing 0.1 g of sodium alginate (as a foulant) and 0.58 g of NaCl (as an electrolyte) in 2 L of DI water. The concentration of organic contaminants in the BFW waste was determined by TOC analyzer (Shimadzu, TOC-V CHS/CSN model, Kyoto, Japan). A large portion of carbon-based material existing in BFW of SAGD operation wastewater is composed by humic acid [104]. In addition, ICP-OES (Thermo Scientific, iCAP™ 6000, Massachusetts, USA) was used to measure the metallic cation concentrations in waste solution. The results are shown in Table 4.2.

4.2.5 Membrane characterization

4.2.5.1 Contact angle measurement

The hydrophilicity of membranes was studied by measuring the water contact angle on their surfaces using Kruss contact angle analyzer (Model DSA 100E, Hamburg, Germany) based on the sessile drop method. For each sample, five measurements were performed, and their average value was reported.

4.2.5.2 Transmission electron microscopy (TEM)

Philips/FEI Morgagni 268 TEM (Eindhoven, The Netherlands) was used to measure the thickness of laminated PANI/rGO layer. At first, membrane samples were stained with uranyl acetate and lead citrate and then embedded in Spurr's resin. Next, ultrathin sections of the samples were cut using an ultramicrotome (Reichert-Jung Ultracut E, USA), and finally, examined by TEM.

4.2.5.3 Electrochemical measurements

The electrical conductivity of the membrane was measured using a Potentiostat/Galvanostat (Princeton Applied Research, model 263A). The fabricated membranes were first cut in a strip shape with a dimension of 1 cm × 2 cm. The strips were then clamped between two glass slides with two copper tape electrode having a separating distance of 1 cm for conductivity measurement. The current developed over the surface of three fabricated membranes were recorded by applying a varied DC potential to the membranes in the dry condition. Also, cyclic voltammetry (CV) experiments were conducted to measure the current generation on the fabricated membranes in the wet condition. The CV tests were all performed by cycling the potential of a working electrode, and measuring the resulting current in a standard three-electrode system using membrane (surface area = 1 cm^2) as a working electrode (membrane), saturated calomel electrode (SCE) as a reference electrode, and platinum wire as a counter electrode. Electric potential, in the range of 0-1.2 V, was applied using the Potentiostat/Galvanostat between membrane and the reference electrode. The electrolyte solution in this experiment was 0.1 M KCl solution.

4.2.5.4 X-ray photoelectron spectroscopy (XPS)

Detailed elemental and chemical bonding analysis of PANI/rGO laminated membranes was conducted by XPS imaging spectrometer (Kratos, AXIS Ultra, Manchester, UK), equipped with a monochromatic Al Kα Xray source PS. XPS analysis provided information about the outer 1–10 nm of the GO derivative samples. In the present work, Low-resolution survey scans, as well as a high-resolution scans were taken. XPS spectra were obtained with passing energy of 160 eV and sweep time of 100 s in the range of 0–1100 eV.

4.2.5.5 Field emission scanning electron microscopy (FESEM)

The morphology of fabricated membranes was observed using field emission scanning electron microscopy (FESEM). The dried membranes samples were firmly mounted on SEM stub using double-sided carbon tapes. To prevent membrane surface charging during FESEM analysis, all membrane samples were coated with a thin film of carbon using Leica EM SCD005 evaporative carbon coater. The top view images were taken at 10 kV and high vacuum condition.

4.2.5.6 Zeta potential measurement

The surface zeta potential of the fabricated membranes was measured using Surpass3 analyzer (Anton Paar, Graz, Austria). Two pieces of membrane samples were cut and fixed on the sample holders and then sample holders submerged in 0.001 M KCl solution at 25 °C. The gap between two flat surfaces was set to 100 μm. The surface zeta potential was then evaluated based on streaming potential and streaming current measurements at different pH values.

4.2.5.7 Mechanical stability test

To investigate the mechanical stability of the fabricated membrane, they were immersed in DI water and stirred for 2 weeks. Water samples were taken at the beginning and after each week and were analyzed with the TOC analyzer to determine the amount of organic material leached from the membrane into the water.

4.2.6 Evaluation of pure water flux

A cross-flow membrane filtration setup was used to study the performance of the fabricated PANI-rGO-PES membranes. The process flow diagram of this setup is shown in Fig. B1 in Appendix B. The membrane was cut into a circular shape with the effective filtration area of 19.6 cm^2. Pure water flux experiments were conducted at a constant transmembrane pressure of 60 psi to compare the permeability of fabricated membranes. Prior to each experiment, the fabricated membranes were immersed in water for 30 min and then were compacted at 80 psi for 1 h to achieve a steady flux. The water flux (J_0, L/m^2h) was determined by direct measurement of the permeate volume collected over time using the following equation:

$$J_0 = \frac{m}{\rho A \Delta t} \tag{4.1}$$

where m is the mass of the permeate water (kg), ρ is the water density (1 kg/L), A is the membrane effective area (m^2), and Δt is the permeation time (h). A digital balance (ME4002, Mettler Toledo, USA) connected to a computer was used to automatically weigh and record the permeate mass over time.

The rejection of organic matter by membranes was evaluated by analyzing the TOC in the collected permeate using the following equation:

$$R(\%) = (1 - \frac{C_p}{C_f}) \times 100 \tag{4.2}$$

where C_p and C_f are the TOC content in permeate and feed solutions, respectively.

4.2.7 Fouling tests

A lab-scale diaphragm pump served to apply 40 psi hydraulic pressure over the membrane surface. Membrane's top layer was connected to either anode or cathode output of a DC power supply to conduct AEO or CER reactions, respectively. Using a piece of stainless-steel as an anode (radius = 2 cm), 2 V electric cell potential was employed to study the electroactivity of the fabricated membranes. The distance between anode and cathode was adjusted at 0.5 cm. To study fouling behavior of membranes, a three-step experimental protocol was followed. First, the pure water flux was recorded (J_{W1}). Then, the water flux during filtration of sodium alginate solution or BFW was measured (J_{Wf}). Finally, after hydraulic washing of the membrane surface with deionized water in the same flowrate for 1 h, the water flux of the cleaned membrane was recorded again (J_{W2}). An equal electric potential, which was applied in fouling step, was also imposed to membrane surface during washing step. To determine the antifouling property of the membranes, total fouling ratio (DR_t) and flux recovery ratio (FRR) were determined as follows:

$$DR_t = 1 - \frac{J_{\mathrm{Wf}}}{J_{\mathrm{W1}}} \tag{4.3}$$

$$FRR = \frac{J_{\mathrm{W2}}}{J_{\mathrm{W1}}} \tag{4.4}$$

Here, DR_t is the sum of irreversible fouling ratio (DR_{ir}) and reversible fouling ratio (DR_r), which provide insight regarding the flux decline because of the adsorption of foulant molecules on the membrane surface and concentration polarization phenomenon, respectively. DR_{ir} and DR_r can be calculated by the following equations:

$$DR_{ir} = 1 - \frac{J_{\mathrm{W2}}}{J_{\mathrm{W1}}} \tag{4.5}$$

$$DR_r = \frac{(J_{\mathrm{W2}} - J_{\mathrm{Wf}})}{J_{\mathrm{W1}}} \tag{4.6}$$

4.3 Results & discussion

4.3.1 Membrane characterization results

To check physical stability of coatings, membranes were immersed in vigorously stirring DI water for two weeks. Fig. B2 in Appendix B presents optical images of the membranes before and after leaching tests. Neither visible defect on the membrane surface nor a change in the turbidity of the aqueous solution was observed for all three membranes, implying that the coated thin films were sufficiently stable under harsh conditions. To confirm this result, the TOC of the aqueous solution was measured after two weeks. It was found that the TOC of solutions containing ECM1, ECM2, and ECM3 were 2.47 ppm, 2.85 ppm, and 2.04 ppm, respectively. The surface charge of fabricated membranes was evaluated through zeta potential measurements. As demonstrated in Fig. 4.1, all membranes had almost similar zeta potentials at different pH values. Zeta potential of the ECM1 was slightly more positive at lower pH values due to its higher density of amine functionals, being readily protonated in acidic environments. The electrical conductivity of the membranes was studied by applying dynamic electric potentials to membranes and recording the current. The trend of current elevation with applied voltage for all three membranes is illustrated in Fig. 4.2. The results showed that ECM3 had the highest electrical conductivity among all membranes (84.53 S/m). The electrical conductivities of ECM1 and ECM2 are 0.459 S/m and 2.170 S/m, respectively. The observed substantial increase in electrical conductivity of ECM3 is due to the higher weight ratio of rGO in its top thin layer, which possesses better electrical conductivity than PANI.

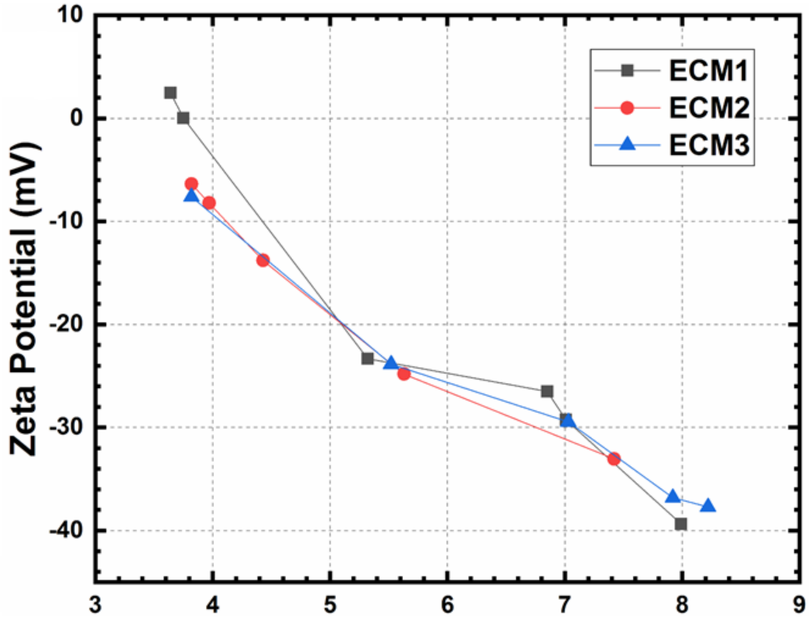

Figure 4.1. Variation of membrane surface zeta potential in different pHs.

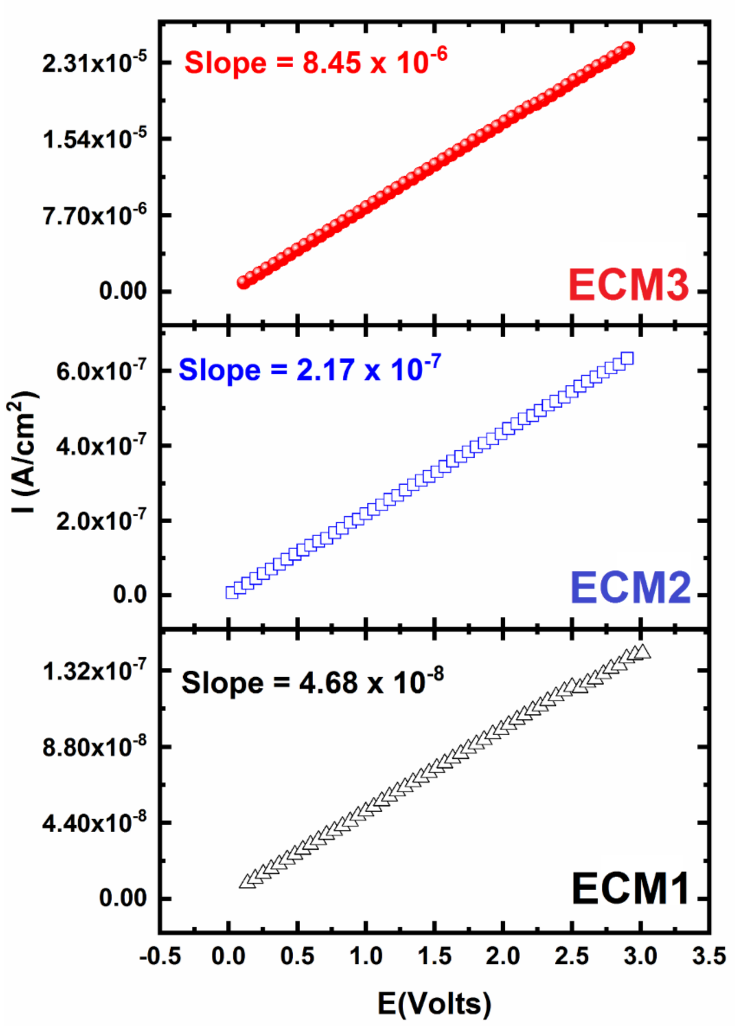

Figure 4.2 Current elevation over the surface of three different membranes by applying a varied DC potential.

Optical photographs, top FESEM, cross-sectional TEM, and water contact angles of the fabricated membranes are shown in Fig. 4.3. It was observed that a uniform and defect-free thin film of PANI or PANI/rGO nanocomposite was coated on the commercial PES support using the pressure-assisted method. The color of HCl-doped PANI is green, and by adding rGO nanosheets, the color of the thin layer is changed to dark gray. Top FESEM images indicated visible open pores on ECM1, which was coated with just PANI. Solid plane structures of rGO nanosheets were clearly observed in ECM2 and ECM3. It seems that rGO nanosheets are buried within the PANI matrix. By increasing rGO content, the number of open pores remarkably declined on the membrane surface, which would likely result in better solute rejection properties.

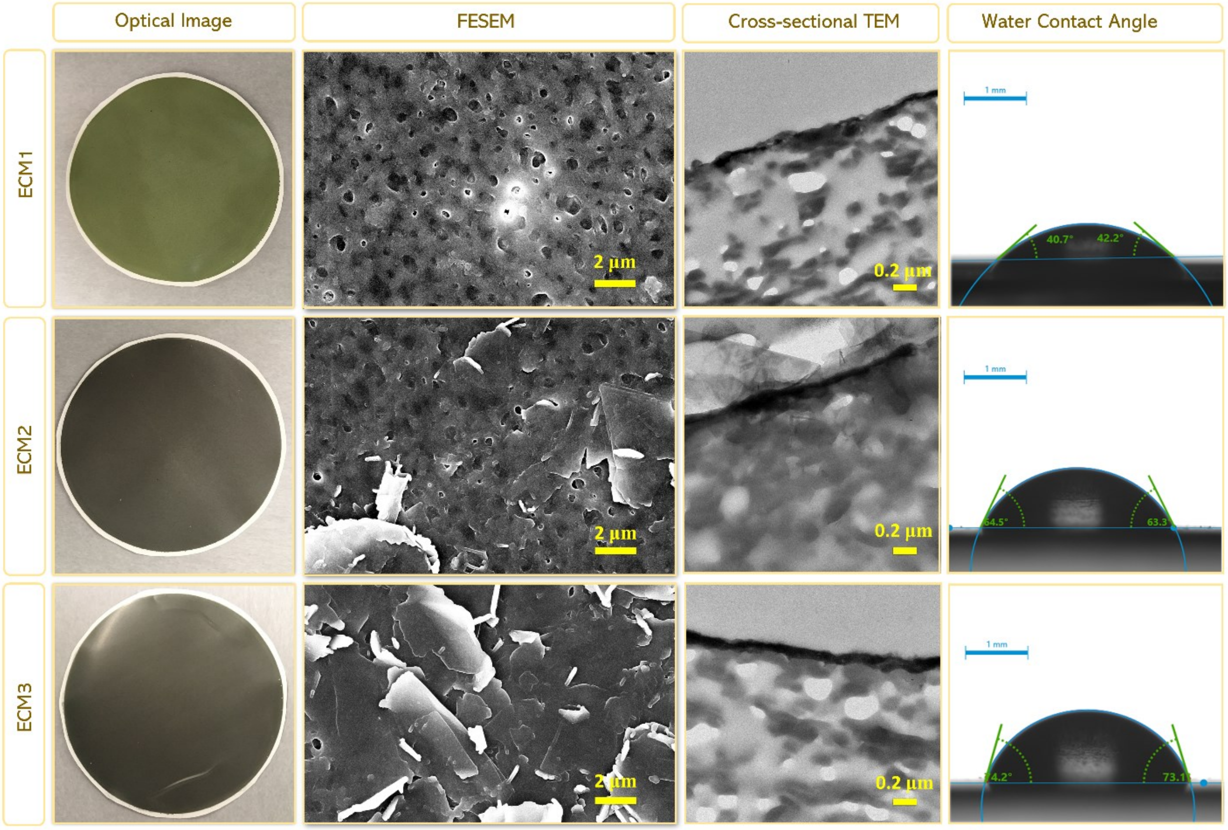

Figure 4.3. Optical, top FESEM, and cross-sectional images with water droplet pictures, representing contact angles in three different fabricated membranes.

According to cross-sectional TEM images, the thickness of the coating layer was in the range of 100-150 nm. In terms of surface wettability, ECM1 with 41.4° had the lowest water contact angle among all membranes. Owing to the hydrophobic nature of rGO, water contact angles were elevated up to 63.9° and 73.65° for ECM2 and ECM3, respectively.

To study the surface chemical composition of the fabricated membranes, XPS analysis was conducted, and the survey spectra, as well as deconvolution of high-resolution spectra of N1s peak, are presented in Fig. 4.4. The survey XPS spectra showed that all membranes contained three main peaks at 284.6 eV, 398.8 eV, and 531.2 eV, which are respectively ascribed to characteristic bonding energy of C1s, N1s, and O1s. The atomic percentage of these three elements in Table B1 revealed that ECM1 possessed the highest contents of nitrogen and oxygen atoms. In ECM2 and ECM3, the incorporated rGO increased the carbon content proportionally. Deconvoluted N1s region gave three smaller peaks including the benzenoid amine at 397.8 eV (=N–), the quinoid amine at 398.3 eV (–NH–) and the cationic nitrogen radical at 399.6 eV ($N^{+\bullet}$) [190]. It clearly shows that acid doping converted some emeraldine base PANI to salt emeraldine, improving the electrical conductivity of the coated surface. The intensities of deconvoluted N1s bonds (Table B1) shows that by increasing rGO content on the membrane surface, the amount of cationic radical nitrogen increased. It might be due to the deprotonation of few carboxylic acid functionals over the rGO plane which can slightly increase acid doping of PANI.

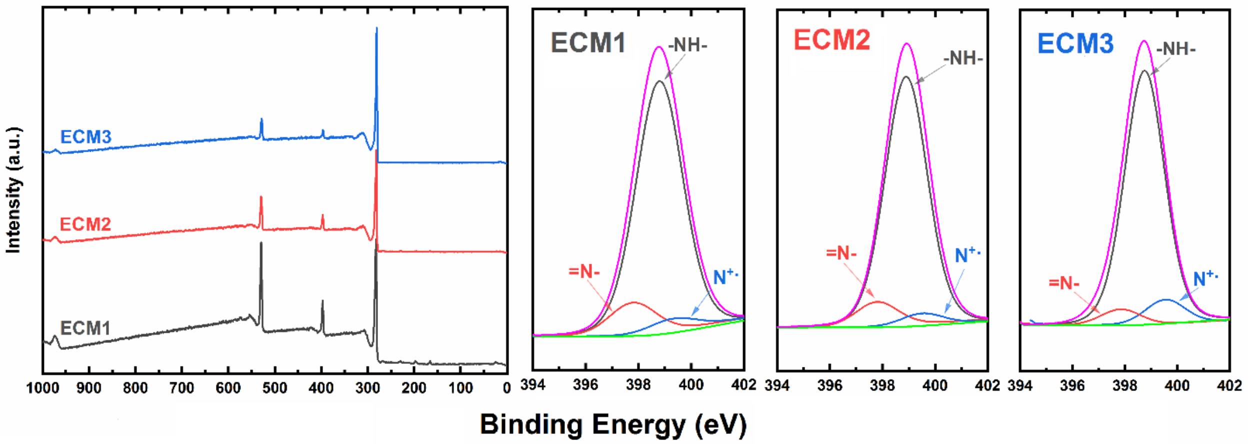

Figure 4.4. Wide-survey XPS spectrum obtained from prepared membranes with typical high-resolution XPS scans of N1s.

4.3.2 Fouling of membranes with sodium alginate

Sodium alginate is an anionic linear polysaccharide which could be derived from seaweed. Owing to abundant hydroxyl and carboxyl functional groups, this natural polymer is negatively charged, forming hydrogels with oppositely-charged ions [191]. In Fig. 4.5, the left plot is showing the normalized water flux of three different membranes after addition of sodium alginate under no electric potential. The initial water fluxes of ECM1, ECM2, and ECM3 after compaction was 238.5 LMH, 188.5 LMH, and 107.7 LMH, respectively. Presence of open pores on the surface of ECM1, as well its higher hydrophilicity (see Fig. 4.3), improve water permeation through the ECM1. The planar structure of rGO blocked some pores on the thin layer of ECM2 and ECM3 and declined hydrophilicity of these membranes. Higher initial flux is a reason behind higher fouling of ECM1, which caused an intense dragging force of foulant material over the surface [146]. In ECM3, higher content of hydrophobic rGO in top layer decreased the affinity of the surface toward water molecules. The absence of aqueous dense layer over hydrophobic membrane surface increases the attachment of foulants, leading to higher observable fouling in ECM3 [192]. Results of normalized flux decline when membranes experienced 2 V cathodic cell potentials are shown in the mid graph of Fig. 4.5. Comparing to baseline (steady J_W/J_{W0} without applying electric potential), improvement of anti-fouling performance was negligible (~2%) for the ECM1. It is worth mentioning that by applying 2 V CER, the ECM1 experienced a distinguished less water decline before 4000 s of filtration time. However, ECM2 and ECM3 demonstrated 5.4% and 11.4% less fouling in the CER mode, respectively. By changing DC electrodes positions and applying 2 V anodic cell potential on the surface of membranes more favorable results in term of fouling propensity of membranes was obtained (right graph of Fig. 4.4). ECM3 with 31.9% showed the highest improvement and ECM1 and ECM2 provided 17.4% and 12.5% less water flux declines, respectively, due to sodium alginate fouling. To get better insight in fouling behavior of the prepared membranes, DR_t values were calculated and plotted in Fig. 4.6. The less DR_t, the better membrane would be in term of resistant against fouling. As can be observed, ECM3 provided the lowest DR_t after applying 2 V anodic or cathodic potential.

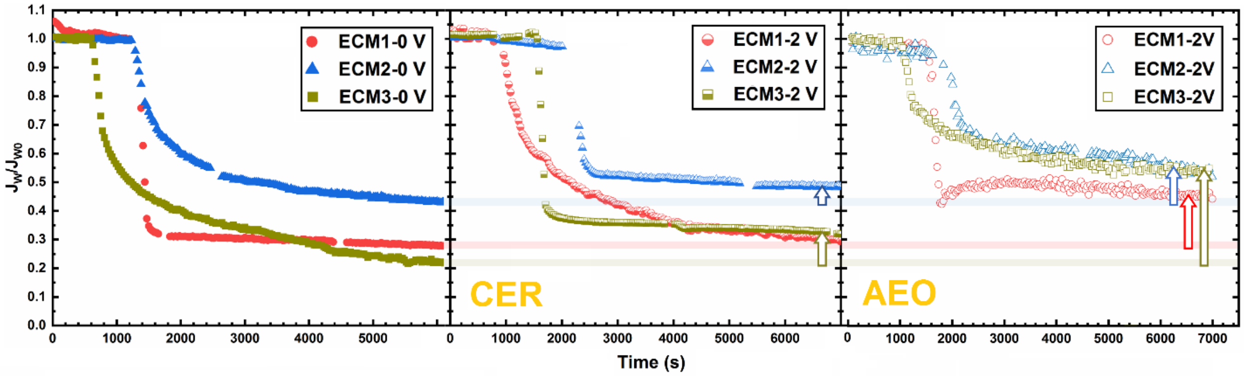

Figure 4.5. Variation of normalized water flux versus time for three fabricated membrane when no electric potential (left graph), 2 V cathodic potential (middle graph), and 2 V anodic potential (right graph) were applied.

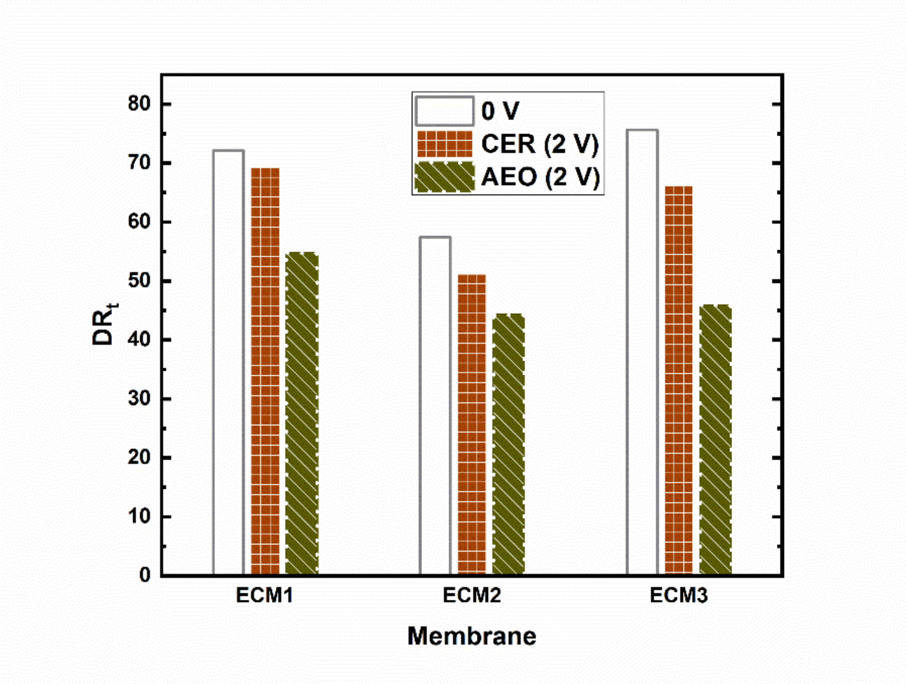

Figure 4.6. DR_t values measured from sodium alginate fouling of membranes under no, CER, and AEO electric potential applications.

4.3.3 Electro-oxidative behavior of membranes under high electric potentials

Since ECM3 provided significant improvement fouling resistance, we focused on this membrane in all following experiments. The capability of ECM3 in water flux recovery was evaluated after sodium alginate fouling in three different anodic potentials by recording normalized water flux versus time, as depicted in Fig. 4.7a. The water flux recovery of ECM3 was also studied under no electric potential. The DR_t, FRR, DR_{ir}, and DR_r were respectively calculated using Eqs. 3-6 and the results are displayed in Fig. 4.7b. As can be seen, increasing the anodic potential, the ECM3 represented less water flux drop after sodium alginate fouling. The DR_t value of the ECM3 reduced from 63.08% for zero potential to 30.97% when 9 V imposed to the membrane surface. Increasing the applied voltage, the FRR showed a growing trend and reached 97.47% under 9 V electro-oxidative potential after washing by salty water. Excellent anti-fouling and flux recovery performances, as well as feasible fabrication method, makes ECM3 a promising candidate for large-scale applications.

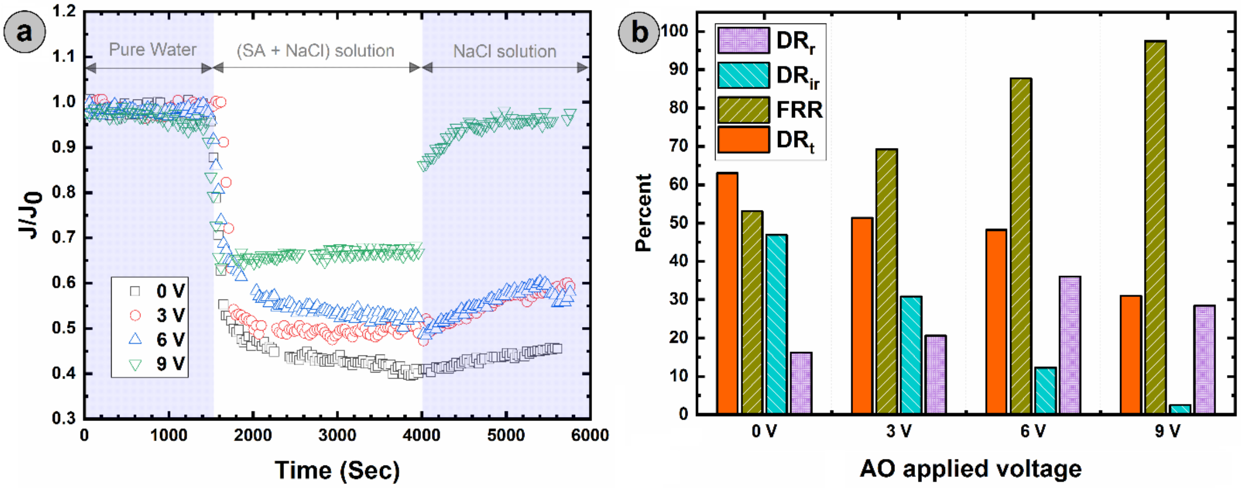

Figure 4.7. (a) dynamic sodium alginate fouling behaviors and (b) representative fouling parameters for the ECM3 in different anodic potentials.

4.3.4 Purification of BFW under different CER potentials

The capability of ECM3 in the purification of BFW was first evaluated in AEO configuration. We observed that permeation of water through the membrane was totally prevented quickly after employing of 3 V anodic cell potential. In contrast, less water flux decline was observed in CER configuration. As represented in Fig. 4.8a, 89.19% normalized water flux decline was observed for the ECM3 under no electric potential by using BFW as a feed solution. Applying 3, 6, and 9 V CER potentials, ECM3 showed 82.75%, 72.20%, and 67.18% normalized water flux decline, respectively. Also, a slight improvement in water flux recovery was observed after the washing steps. Such a sharp flux decline and a minor flux recovery after washing imply that the main mechanism of fouling was membrane pore blocking by the organic matter in BFW [151,193]. Irreversible fouling of ECM3 has, therefore, significantly reduced the FRR. Fig. 4.8b shows the optical images of feed BFW, as well as the permeate solutions at different CER potentials. The percentages of TOC removal in four experiments are illustrated in Fig. 4.8c. It is evident that by increasing the applied CER potential, the TOC rejection of the ECM3 was improved. ECM3 provided 33.29% TOC rejection without applying external potential, which increased significantly to 85.52% by applying 9 V negative DC potential. With increasing CER potential, the density of negative charge would increase over membrane surface, thereby a more severe electrostatic repulsion with negatively-charged organic matters in BFW caused a better performance in TOC removal.

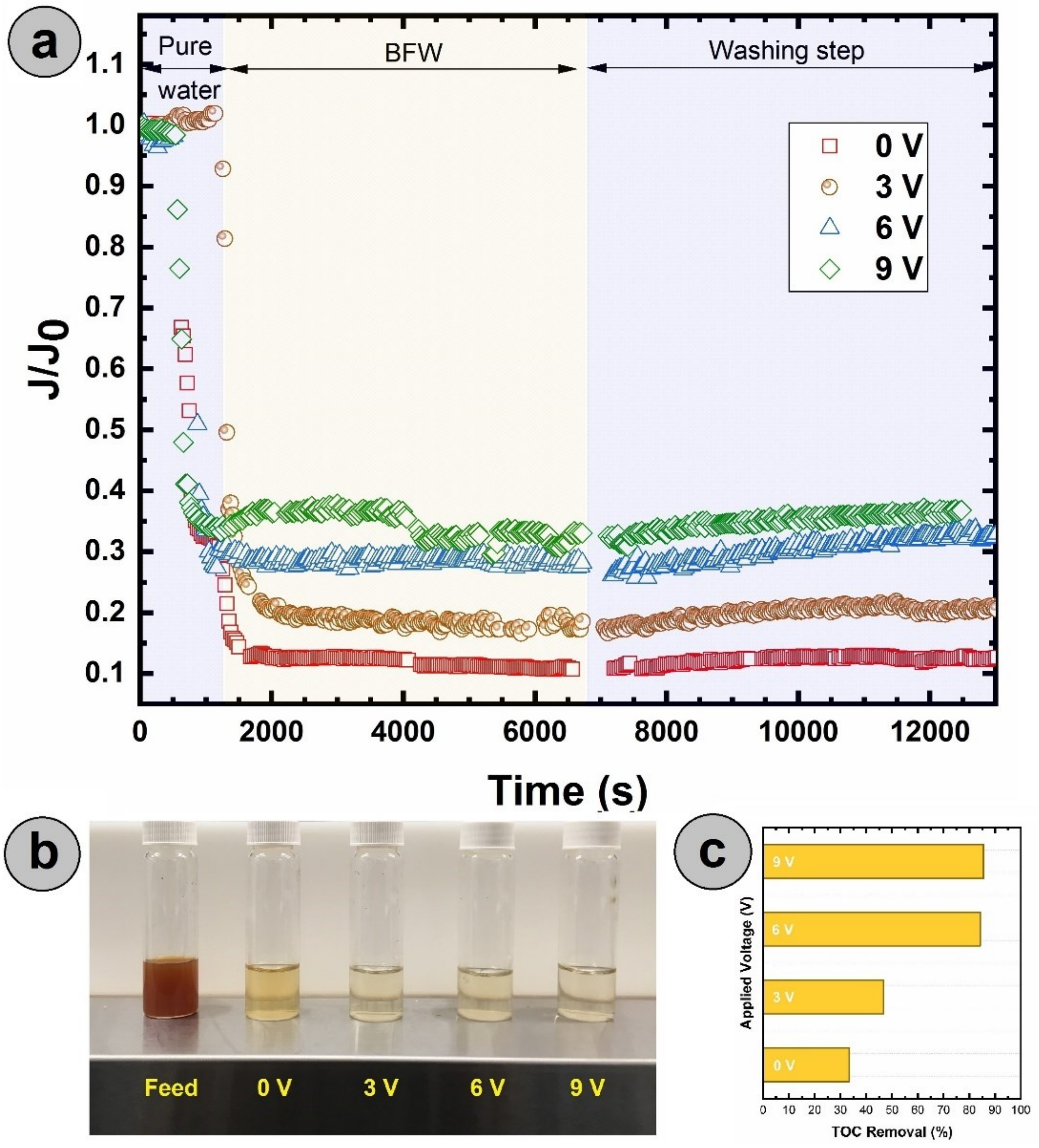

Figure 4.8. (a) Normalized water flux decline of the ECM3 in different CER potentials, (b) optical images of BFW and the permeate solutions obtained at different applied potentials, and (c) TOC removal performance.

4.3.5 Hypothetical mechanisms of fouling reduction in ECMs

The improved anti-fouling behaviors of ECMs could be explained by the following reasons:

4.3.5.1 Electrostatic forces

With a few exemptions, the surface charge of organic matter is naturally negative in water [194]. Therefore, making the membrane surface more negative would obviously be a practical strategy to minimize the attachment of organic foulants to the surface. It was reported that organic fouling of membrane due to pore blocking and gel formation could be partially controlled via surface charge manipulation [195]. *Dudchenko* et al. studied the electrostatic interactions between organic foulant and an electrically conductive membrane made of poly(vinyl alcohol) and carboxylated multi-walled carbon nanotubes. They demonstrated that applying -3 V and -5 V the fouling rate by alginic acid has decreased significantly, compared to no voltage scenario [174]. Using a modified version of the Poisson–Boltzmann equation in the *DLVO* theory, they showed that by applying electrical potential electrostatic interactions created strong repulsive force between the membrane surface and the charged foulants. It was also found that with increasing cathodic potential, the overall repulsive force would increase. Using the ECMs as a cathode (CER plot in Fig. 4.5) induces a negative charge on the surface, which subsequently enhances the electrostatic repulsion between the membrane and sodium alginate foulants. According to *Gouy-Chapman* theory, existing of counter charge substances like divalent cations (Ca^{2+} and Mg^{2+}) in water may alter charge property of the membrane surface, making the membrane less negatively charged [196]. Given that, failure of the ECM3 in the purification of BFW under anodic potentials could be correlated to the presence of multivalent cations in the feed water.

4.3.5.2 Electric field effect

Application of large electric field between two external electrodes mounted on both sides of a membrane was found to improve the anti-fouling tendency of the membrane, as well as permeate water flux [197,198]. It is hypothesized that in an electric field of appropriate polarity, electrophoresis phenomenon decreases the rate of cake deposition and increases the rate of permeation through the filter cake by electroosmosis. A recent molecular dynamics simulation study confirmed that besides water flux, the rejection of solutes also improves by applying electric field due to formation a stable hydration shell around solute that prevents solute passage through membrane pores [199]. However, in such electro-filtration system, electrical insulation of the middle-standing membrane decreases the effectiveness of external electric field on feed solution, thereby increasing energy demands. Using ECMs between electrodes the applied electric field won't be diminished so that even low potentials are significantly effective on controlling the fouling behavior.

4.3.5.3 Gas bubbling

Gas bubbling was found to be an effective technique to decrease membrane fouling [179]. In conventional oxidation processes on the metal electrode, oxygen evolution reaction (OER) occurs on the electrode surface through water electrolysis (Eq. 7). In the present study, the anode (graphene) is made by SP^2 carbon-based materials, which is an active electrode and can drive OER reaction in low potentials. Therefore, even in low potentials, there is a high chance of oxygen production when the ECM is used as the anode. On the cathode, water electrolysis can also result in hydrogen production, as shown in Eq. 8. By increasing electric potential, the amount of produced gas (oxygen or hydrogen) on the electrode surface increases, which can effectively reduce the fouling rate.

$$2H_2O \rightarrow O_2 + 4H^+ + 4e^- \tag{4.7}$$

$$2H_2O + 2e^- \rightarrow H_2 + 2OH^- \tag{4.8}$$

Existing of some ionic species in the aquatic environment may cause various side reactions [200]. For instance, in the presence of chloride anions, chlorine (Cl_2) can be generated via an indirect oxidation reaction on the anode surface (Eq. 9). The produced chlorine gas easily diffuses from the membrane surface to the bulk solution, disproportionating to produce hypochlorous acid (HClO) and chloride (Eq. 10).

$$2Cl^- \rightarrow Cl_2 + 2e^- \tag{4.9}$$

$$Cl_2 + H_2O \leftrightarrow HClO + Cl^- + H^+ \tag{4.10}$$

4.3.5.4 Electrochemical reactions

Regardless of process configuration, two mechanisms could control membrane fouling when electrochemical reactions occur on the surface. First, production of superactive reagents like hydroxyl radicals ($OH^\bullet$), which can attack chemical bonds of organic compounds close to the membrane surface. It minimizes their molecular size and reduces their attachment to the membrane surface through reduced hydrophobic interactions. Second, easy-access to $OH^\bullet$ may completely break down chemical structure of the adsorbed foulants (surface self-cleaning).

4.3.5.4.1 CER reactions

In acidic or neutral media, hydrogen peroxide can be generated on the cathode surface via two-electron reduction of dissolved oxygen (Eq. 11) [201]. In a basic solution, oxygen electroreduction makes hydroperoxide ions (HO_2^-), which is a conjugate form of H_2O_2 (pK_a = 11.64, Eq. 12) [202].

$$O_2 + 2H^+ + 2e^- \rightarrow H_2O_2 \tag{4.11}$$

$$O_2 + H_2O + 2e^- \rightarrow HO_2^- + OH^- \tag{4.12}$$

When ferrous cations exist in water (e.g., in BFW, Table 4.1), classical Fenton process occurs in which super-active hydroxyl radicals are produced ($OH^\bullet$) as follows:

$$Fe^{2+} + H_2O_2 + H^+ \rightarrow Fe^{3+} + H_2O + OH^\bullet \tag{4.13}$$

Hydroxyl radical attack organic molecules (R) and thus degrade their carbon-based structure through different mechanisms: (i) forming water through dehydrogenation, (ii) redox reactions, and (iii) electrophilic substitution on non-saturated carbon bonds, with the latter being the most typical degradation mechanism of aromatic compounds [203].

4.3.5.4.2 AEO reactions

Two main oxidation mechanisms in AEO configuration are:

(i) direct oxidation, where the membrane surface directly transfers electrons to organic species (R) and subsequently oxidizes them (Eq. 14) [204]. In theory, direct electro-oxidation is just possible at low potentials, where oxygen could not be evolved on electrode surface. The reaction rate in direct mechanism has very low kinetics specially in the graphene-based electrodes with excellent adsorption properties.

(ii) indirect oxidation where some super-reactive intermediates are produced from the oxidation of water, as well as other ions, and they participate in demineralization of organic compounds (Eq. 15 and 16). One of the very common indirect reactions is the oxidation of water molecules, which results in the production of $^{\bullet}$OH and O_3 as follows [205]:

$$R_{Adsorbed\ on\ ECM} - 2e^- \rightarrow R_{Oxidized} \tag{4.14}$$

$$ECM + H_2O \rightarrow ECM(OH^{\bullet}) + H^+ + e^- \tag{4.15}$$

$$3H_2O \rightarrow O_3 + 6H^+ + 6e^- \tag{4.16}$$

Regardless of the nature of organic foulant, hydroxyl and ozone can non-selectively degrade carbon-based backbone, forming CO_2 and H_2O as final products. The surface adsorbed hydroxyl radicals, ($ECM(OH^{\bullet})$, can produce H_2O_2 as a moderate oxidant. This reaction (equation 17) is more likely to happen over low O_2-overpotential electrodes like graphene. In such condition, redox couple of ECMO/ECM is acting as an active mediator for the oxidation of organic substances.

$$2ECM(OH^{\bullet}) \rightarrow 2ECMO + 2H_2O_2 \qquad (4.17)$$

Carbon-based electrodes like graphene have low oxygen evaluation overpotentials, implying that only partial oxidation of organic pollutants is allowed to be happened via indirect mechanism [200].

In a water solution, hypochlorite ions (ClO^-) are in equilibrium with hypochlorous acid (Eq. 18). By increasing pH to more than 8 (increasing OH^- in the solution), H^+ will be consumed and more hypochlorite ions will be generated based on *Le Chatelier's* principle. All chlorine-based species are capable of oxidizing organic substances near the surface of the membrane, consequently reducing its fouling propensity [177].

$$HClO \leftrightarrow ClO^- + H^+ \qquad (4.18)$$

Despite unfavorable electrostatic forces in sodium alginate fouling of the ECMs exposed to AEO (positive charge), a series of effective electrooxidation reactions, as well as the production of oxygen bubbles could minimize water flux decline (see Fig. 4.4). Total flux decline results confirm the strong impact of AEO configuration on the recovery of fouled membranes (Fig. 4.5).

4.4 Conclusion

This study presented a versatile method to develop physically stable electroconductive membrane. Optimized weight ratios of PANI and rGO were co-deposited over PES support, under pressurized air force, to fabricate electric potential-responsive membranes. The fabricated membranes were stable under harsh stirring conditions. By increasing rGO content, the electric conductivity of the final membrane increased accordingly. Our findings showed that fouling potential of organic matter in the synthetic wastewater of sodium alginate can be mitigated in AEO configuration. ECM3 demonstrated 31.9% less water flux decline by applying only 2 V anodic potential. By applying higher electric potentials in AEO, less water flux decline, as well as better flux recovery ratios could be achieved. In the case of BFW, AEO failed in permeation tests, while the anti-fouling performance and rejection results of CER were promising. The antifouling properties of the prepared ECMs were justified based on electrostatic interactions, gas bubbling, and electrochemical reactions.

Chapter 5

Conclusions and future works

5.1 Conclusion

The thesis is built on the experimental research on fabrication and charactrization of UF graphene-based nanocomposite memberane and application for the treatment of produced water obtained from SAGD operation. The research was conducted in three stages considering the main objective, which was developing high-performance nanocomposite membrane with enhanced permeation, sepration and fouling resistance properties.

In the first part of the thesis, graphene nanoribones were used for the first time to fabricate nanocomposite membranes using NIPS fabrication method The synthesized membranes by graphene nanoribones were then compared with three other GO-based nanocomposite membranes, in terms of water flux, fouling resistance, separation performance. The GO derivatives used have different shapes and different oxidation states that affected membranes properties such as pore size, hydrophlicity, and surface charge. The results for contact angle and zeta potential measurements showed formation of more hydrophilic and negatively charged PES-GO nanocomposite membranes. All graphene-based nanocomposite membranes exhibited better water flux and separation of organic matter compared to the unmodified PES membrane. The fouling measurement results displayed that fouling was hindered owing to enhanced membrane surface properties. Longitudinally unzipped graphene oxide nanoribbons (GONR-L) at an optimum loading of 0.1 wt% supplied the maximum water flux (70 LMH at 60 psi), organic matter rejection (59%) and antifouling properties (30% improvement compared to pristine PES membrane). Flux recovery ratio experiments indicated a remarkable enhancement in the fouling resistance property of PES/GO nanocomposite membranes.

In the second part of the thesis, two experimental techniques were used to study antifouling behavior of GO-modified nanocomposite membrane. The extent of organic fouling depends on membrane-foulant affinity, which relies on the physicochemical properties of the foulant and membrane. In this research, an extended DLVO (XDLVO) interaction energy analysis, fouling experiments, and quartz crystal microbalance with dissipation monitoring (QCM-D) were all employed to investigate the adsorption behavior of organic foulant from steam assisted gravity drainage (SAGD) produced water on three synthesized ultrafiltration (UF) membranes including pristine polyethersulfone (PES), PES/polyvinylpyrrolidone (PVP), and PES/PVP/ graphene oxide (GO) nanocomposite. In the XDLVO analysis, the fundamental interactions (van der Waals, electrostatic, and acid-base interactions) that control organic fouling were evaluated. Surface tension parameters, derived from contact angle measurements, were employed to calculate the free energy of adhesion between membrane and foulant material to elucidate the differences in flux decline. It was found that acid-base interaction energies between foulant and membrane's surface were the most influential factor on the total energy of interaction in distance shorter than 5 nm. This investigation demonstrated that surface free energy elements, evaluated for the wastewater and membranes, could successfully anticipate fouling behavior of organic matters on the membrane surface. QCM-D technique was also used to study the fouling behavior of membranes. The QCM-D results contrasted with XDLVO theory and fouling test due to different fluid conditions and surface characteristics.

In the third part of the thesis, a thin layer of polyaniline (PANI)- reduced graphene oxide (rGO) was laminated on polyethersulfone (PES) support by feasible pressure-assisted technique. Using electrical conductivity of the fabricated membranes, we reduced organic fouling by applying an external electric field. Electrical conductivity of pristine PANI film was 0.46 S/m while adding appropriate amount of rGO, it was improved to 84.53 S/m. Physical stability tests were done for two weeks by vigorously-stirring water on top, showing that the laminated coating is highly stable where neither visible defect nor particle leaching out was observed in aqueous solution. We applied either of anodic or cathodic potentials in different ranges on the prepared membranes when feed water contained sodium alginate or boiler feed water (BFW) waste of steam-assisted gravity drainage (SAGD) operation. The obtained results for anodic potentials were more favorable in term of less fouling for all membranes. Batch tests showed that membrane ability in alginate fouling resistance can improve about 30% when 2 V anodic potential was applied. By increasing the applied voltage from 3 V to 9 V, the antifouling propensity of membrane increased dramatically in anode setting. The enhanced electrostatic repulsive force between foulant and membrane surface, massive gas bubble as well as electrooxidative reactions are listed as possible reasons for such observation. Cathodic reduction was also tested for BFW feed, where both water flux decline and rejection performance were favorably ameliorated by elevating electric potential.

InsituSim cloud-based software (https://insitusim.com) was employed to simulate a SAGD plant with 33,000 bpd bitumen production rate (WLS inlet flow rate of 900,000 kg/hr or 135,942 bpd) before and modification with our membrane-based system for water treatment. The power consumption for the conventional warm lime softener/ion exchange resin configuration and steam to oil ratio (SOR) of 3 is 21.5 MW which will reduce to 13 MW using our membrane scheme. The two main changes in the simulation are replacement of OTSG with 80% steam quality with a drum-type boiler with 99.9% steam quality, and reducing the SOR from 3 to 2, as the higher steam quality increases the bitumen production rate. Therefore, the energy efficiency for one SAGD plant will be 8.5 MW with the successful use of the membrane process.

In terms of water efficiency, the current scheme uses 26,000 bpd brackish water, as makeup water, which will be reduced to 7,000 bpd with the replacement of the membrane process. In addition, 19,000 bpd decrease in makeup water usage will be obtained. The total water recycling rate will be 99.78% which is close to zero liquid discharge (ZLD).

5.2 Possible Future Directions

In this study, we fabricated GO-based nanocomposite membranes for pressure-assisted filtration setup. However GO-based nanocomposite membranes could be used in other membrane filtrations processes including forward osmosis (FO) and membrane distillation (MD) to increase the efficiency of the water treatment system. Incorporation of GO nanosheets can change the thermodynamic of casting solution in the process of membrane fabrication therefore, it can tune the pore size and skin layer thickness so water throughput may increase in FO filtration method. Moreover, to enhance the rate of contaminants removal in electro-Fenton cell, it may couple with FO filtration setup. One of the weaknesses of the electro-Fenton reaction is that the rate of contaminant removal becomes extremely slow when the concentration decreases in the feed side. By coupling electro-Fenton cell with FO setup, water will permeate to draw side and the concentration of organic matter will increase in feed side resulting in faster contaminant removal.

Regarding MD, the driving force for the membrane distillation method is temperature gradient and the membrane suitable for MD should have hydrophobic characteristics. Incorporation of rGO to the membrane matrix can increase the hydrophobicity of membrane so hydrophobic graphene-based nanocomposite membranes can be designed and fabricated for MD process. The objective could be to reduce energy consumption and increase the separation efficiency of MD process with these membranes.

5.3 List of contributions

The outcomes of this research are published and presented in the following journals and conferences:

5.3.1 Journal papers

1. A. Karkooti, A.Z. Yazdi, P. Chen, M. McGregor, N. Nazemifard, M. Sadrzadeh, Development of advanced nanocomposite membranes using graphene nanoribbons and nanosheets for water treatment, J. Membrane. Science. 560 (2018) 97–107. doi:10.1016/j.memsci.2018.04.034.

2. A. Karkooti, M. Rastgar, N. Nazemifard, M. Sadrzadeh, Study on antifouling behaviors of GO modified nanocomposite membranes through QCM-D and surface energetics analysis. Accepted in Colloids and Surfaces A: Physicochemical and Engineering Aspects, 2019

3. A. Karkooti, M. Rastgar, N. Nazemifard, M. Sadrzadeh, Anti-fouling electro-conductive thin film composite membranes fabricated by reduced graphene oxide- polyaniline (rGO-PANI), Accepted in J. Science of the Total Environment, 2019

5.3.2 Conference presentations

1. A. Karkooti, M. Rastegar, M. Sadrzadeh, N. Nazemifard, Fabrication of fouling-resistant electro-conductive thin film composite membranes by laminating polyaniline (PANI) and reduced graphene oxide (rGO) on polyethersulfone, 2019 Annual Meeting The American Institute of Chemical Engineers (AIChE), Orlando, FL, Nov 2019

2. A. Karkooti, M. Sadrzadeh, N. Nazemifard, Study on antifouling properties of electro-conductive membranes fabricated by rGO-PANI laminate, 13th International Symposium on Electrokinetics (ELKIN), Massachusetts Institute of Technology, Boston, MA, June 2019

3. A. Karkooti, M. Sadrzadeh, N. Nazemifard, Study on antifouling behaviors of GO modified nanocomposite membranes through QCMD and surface energetics analysis, 28th Annual Meeting North American Membrane Society (NAMS), Pittsburgh, PA, May 2019

4. A. Karkooti, M. Sadrzadeh, N. Nazemifard, Study the dynamic adsorption of organic foulants from SAGD produced water onto PES-GO membrane using QCM-D, XXIX Interamerican Congress of Chemical Engineering Incorporating the 68th Canadian Chemical Engineering Conference, Toronto, ON, October 2018

5. A. Karkooti, M. Sadrzadeh, N. Nazemifard, Synthesis and characterization of graphene-based polyethersulfone nano-composite membrane , 67th Canadian Chemical Engineering Conference, Edmonton,AB , October 2017

References

[1] W.E. Forum, The Global Risks Report 2019 14th Edition, 2019.

[2] M. Sadrzadeh, D. Pernitsky, M. Mcgregor, Nanofiltration for the Treatment of Oil Sands-Produced Water, in: IntechOpen, 2018. doi:10.5772/intechopen.74086.

[3] S.G. Thakurta, A. Maiti, D.J. Pernitsky, S. Bhattacharjee, Dissolved Organic Matter in Steam Assisted Gravity Drainage Boiler Blow-Down Water, (2013). doi:10.1021/ef4002154.

[4] D.W. Jennings, A. Shaikh, B. Petrolite, W. Airport, V. Boule, S. Land, Heat-Exchanger Deposition in an Inverted Steam-Assisted Gravity Drainage Operation . Part 1 . Inorganic and Organic Analyses of Deposit Samples, (2007) 176–184. doi:10.1021/ef060109d.

[5] X. Shi, G. Tal, N.P. Hankins, V. Gitis, Journal of Water Process Engineering Fouling and cleaning of ultrafiltration membranes : A review, J. Water Process Eng. 1 (2014) 121–138. doi:10.1016/j.jwpe.2014.04.003.

[6] M. Mulder, Basic principles of membrane technology, 2nd ed., Kluwer Academic, Dordrecht, The Netherlands, 1997.

[7] R.W. Baker, Membrane Technology and Application, 2nd Editio, Wiley, 2004.

[8] C.A. Smolders, A.J. Reuvers, R.M. Boom, I.M. Wienk, Microstructures in phase-inversion membranes . Part 1 . Formation of macrovoids *, 73 (1992) 259–275.

[9] I.M.W. C.A. Smolders, A.J. Reuvers, R.M. Boom, Microstructures in phaseinversionmembranes .1. Formation of macrovoids, J. Memb. Sci. 73 (1992) 259–275.

[10] W. Guo, H.-H. Ngo, J. Li, A mini-review on membrane fouling., Bioresour. Technol. 122 (2012) 27–34. doi:10.1016/j.biortech.2012.04.089.

[11] R. Zhang, Y. Liu, M. He, Y. Su, X. Zhao, M. Elimelech, Z. Jiang, Antifouling membranes for sustainable water purification: strategies and mechanisms., Chem. Soc. Rev. 45 (2016) 5888–5924. doi:10.1039/c5cs00579e.

[12] A.S. Al-Amoudi, Factors affecting natural organic matter (NOM) and scaling fouling in NF membranes: A review, Desalination. 259 (2010) 1–10. doi:10.1016/j.desal.2010.04.003.

[13] C.Y. Tang, T.H. Chong, A.G. Fane, Colloidal interactions and fouling of NF and RO membranes : A review, Adv. Colloid Interface Sci. 164 (2011) 126–143. doi:10.1016/j.cis.2010.10.007.

[14] Y. Zhang, L. Wang, Y. Xu, ZrO2 solid superacid porous shell/void/TiO2 core particles (ZVT)/polyvinylidene fluoride (PVDF) composite membranes with anti-fouling performance for sewage treatment, Chem. Eng. J. 260 (2015) 258–268. doi:10.1016/j.cej.2014.08.083.

[15] Y. Zhang, L. Wang, Y. Xu, Effect of doping porous ZrO2 solid superacid shell/void/TiO2 core nanoparticles (ZVT) on properties of polyvinylidene fluoride (PVDF) membranes, Desalination. 358 (2015) 84–93. doi:10.1016/j.desal.2014.12.022.

[16] Y. Zhang, F. Liu, Y. Lu, L. Zhao, L. Song, Investigation of phosphorylated TiO2–SiO2 particles/polysulfone composite membrane for wastewater treatment, Desalination. 324 (2013) 118–126. doi:10.1016/j.desal.2013.06.007.

[17] W. Salim, W.S.W. Ho, Recent developments on nanostructured polymer-based membranes, Curr. Opin. Chem. Eng. 8 (2015) 76–82. doi:http://dx.doi.org/10.1016/j.coche.2015.03.003.

[18] A. Rahimpour, S.S. Madaeni, S. Mehdipour-Ataei, Synthesis of a novel poly(amide-imide) (PAI) and preparation and characterization of PAI blended polyethersulfone (PES) membranes, J. Memb. Sci. 311 (2008) 349–359. doi:10.1016/j.memsci.2007.12.038.

[19] A. Rahimpour, S.S. Madaeni, Polyethersulfone (PES)/cellulose acetate phthalate (CAP) blend ultrafiltration membranes: Preparation, morphology, performance and antifouling properties, J. Memb. Sci. 305 (2007) 299–312. doi:10.1016/j.memsci.2007.08.030.

[20] S. Zinadini, A.A. Zinatizadeh, M. Rahimi, V. Vatanpour, H. Zangeneh, Preparation of a novel antifouling mixed matrix PES membrane by embedding graphene oxide nanoplates, J. Memb. Sci. 453 (2014) 292–301. doi:10.1016/j.memsci.2013.10.070.

[21] F. Meng, S.R. Chae, A. Drews, M. Kraume, H.S. Shin, F. Yang, Recent advances in membrane bioreactors (MBRs): Membrane fouling and membrane material, Water Res. 43 (2009) 1489–1512. doi:10.1016/j.watres.2008.12.044.

[22] D. Li, H. Wang, Recent developments in reverse osmosis desalination membranes, J. Mater. Chem. 20 (2010) 4551–4566. doi:10.1039/b924553g.

[23] L.Y. Ng, A.W. Mohammad, C.P. Leo, N. Hilal, Polymeric membranes incorporated with metal/metal oxide nanoparticles: A comprehensive review, Desalination. 308 (2013) 15–33. doi:10.1016/j.desal.2010.11.033.

[24] W. Salim, W.W. Ho, Recent developments on nanostructured polymer-based membranes, Curr. Opin. Chem. Eng. 8 (2015) 76–82. doi:10.1016/j.coche.2015.03.003.

[25] X. Qu, P.J.J. Alvarez, Q. Li, Applications of nanotechnology in water and wastewater treatment, Water Res. 47 (2013) 3931–3946. doi:10.1016/j.watres.2012.09.058.

[26] C.H. Ahn, Y. Baek, C. Lee, S.O. Kim, S. Kim, S. Lee, S.H. Kim, S.S. Bae, J. Park, J. Yoon, Carbon nanotube-based membranes: Fabrication and application to desalination, J. Ind. Eng. Chem. 18 (2012) 1551–1559. doi:10.1016/j.jiec.2012.04.005.

[27] D. Li, Y. Yan, H. Wang, Recent advances in polymer and polymer composite membranes for reverse and forward osmosis processes, Prog. Polym. Sci. 61 (2016) 104–155. doi:10.1016/j.progpolymsci.2016.03.003.

[28] K.P. Lee, T.C. Arnot, D. Mattia, A review of reverse osmosis membrane materials for desalination-Development to date and future potential, J. Memb. Sci. 370 (2011) 1–22. doi:10.1016/j.memsci.2010.12.036.

[29] A.W. Mohammad, Y.H. Teow, W.L. Ang, Y.T. Chung, D.L. Oatley-Radcliffe, N. Hilal, Nanofiltration membranes review: Recent advances and future prospects, Desalination. 356 (2015) 226–254. doi:10.1016/j.desal.2014.10.043.

[30] L.Y. Ng, A.W. Mohammad, C.P. Leo, N. Hilal, Polymeric membranes incorporated with

metal/metal oxide nanoparticles: A comprehensive review, Desalination. 308 (2013) 15–33. doi:10.1016/j.desal.2010.11.033.

[31] K.C. Khulbe, C. Feng, T. Matsuura, The art of surface modification of synthetic polymeric membranes, J. Appl. Polym. Sci. 115 (2009) 855–895. doi:10.1002/app.

[32] J. Yin, B. Deng, Polymer-matrix nanocomposite membranes for water treatment, J. Memb. Sci. 479 (2014) 256–275. doi:10.1016/j.memsci.2014.11.019.

[33] L. Yan, Y.S. Li, C.B. Xiang, S. Xianda, Effect of nano-sized Al2O3-particle addition on PVDF ultrafiltration membrane performance, J. Memb. Sci. 276 (2006) 162–167. doi:10.1016/j.jsb.2006.03.024.

[34] N. Ghaemi, S.S. Madaeni, P. Daraei, H. Rajabi, S. Zinadini, A. Alizadeh, R. Heydari, M. Beygzadeh, S. Ghouzivand, Polyethersulfone membrane enhanced with iron oxide nanoparticles for copper removal from water: Application of new functionalized Fe3O4 nanoparticles, Chem. Eng. J. 263 (2015) 101–112. doi:10.1016/j.cej.2014.10.103.

[35] M.L. Luo, J.Q. Zhao, W. Tang, C.S. Pu, Hydrophilic modification of poly(ether sulfone) ultrafiltration membrane surface by self-assembly of TiO2 nanoparticles, Appl. Surf. Sci. 249 (2005) 76–84. doi:10.1016/j.apsusc.2004.11.054.

[36] H. Choi, A. Zakersalehi, S.R. Al-Abed, C. Han, D.D. Dionysiou, Nanostructured titanium oxide film- and membrane-based photocatalysis for water treatment, in: A. Street, R. Sustich, J. Duncan, N. Savage (Eds.), Nanotechnol. Appl. Clean Water, 2nd ed., Elsevier, Oxford, 2014: pp. 123–132.

[37] Y. Zhang, P. Liu, Polysulfone(PSF) composite membrane with micro-reaction locations (MRLs) made by doping sulfated TiO2 deposited on SiO2 nanotubes (STSNs) for cleaning wastewater, J. Memb. Sci. 493 (2015) 275–284. doi:10.1016/j.memsci.2015.06.011.

[38] G.S. Lai, W.J. Lau, P.S. Goh, A.F. Ismail, N. Yusof, Y.H. Tan, Graphene oxide incorporated thin film nanocomposite nanofiltration membrane for enhanced salt removal performance, Desalination. 387 (2016) 14–24. doi:10.1016/j.desal.2016.03.007.

[39] T. Kuilla, S. Bhadra, D. Yao, N.H. Kim, S. Bose, J.H. Lee, Recent advances in graphene based polymer composites, Prog. Polym. Sci. 35 (2010) 1350–1375. doi:10.1016/j.progpolymsci.2010.07.005.

[40] J. Lee, H.R. Chae, Y.J. Won, K. Lee, C.H. Lee, H.H. Lee, I.C. Kim, J. min Lee, Graphene oxide nanoplatelets composite membrane with hydrophilic and antifouling properties for wastewater treatment, J. Memb. Sci. 448 (2013) 223–230. doi:10.1016/j.memsci.2013.08.017.

[41] M. Miculescu, V.K. Thakur, F. Miculescu, S.I. Voicu, Graphene-based polymer nanocomposite membranes: a review, Polym. Adv. Technol. 27 (2016) 844–859. doi:10.1002/pat.3751.

[42] Z. Wang, H. Yu, J. Xia, F. Zhang, F. Li, Y. Xia, Y. Li, Novel GO-blended PVDF ultrafiltration membranes, Desalination. 299 (2012) 50–54. doi:10.1016/j.desal.2012.05.015.

[43] B.M. Ganesh, A.M. Isloor, A.F. Ismail, Enhanced hydrophilicity and salt rejection study

of graphene oxide-polysulfone mixed matrix membrane, Desalination. 313 (2013) 199–207. doi:10.1016/j.desal.2012.11.037.

[44] J.L. Yuanyuan Zhao, Jiaqi Lu, Xuyang Liu, Yudan Wang, Jiuyang Lin, Na Peng, F. Zhao, Performance enhancement of polyvinyl chloride ultrafiltration membrane modified with graphene oxide, J. Colloid Interface Sci. 480 (2016) 1–8. doi:10.1016/j.jcis.2016.06.075.

[45] H. Wu, B. Tang, P. Wu, Development of novel SiO2-GO nanohybrid/polysulfone membrane with enhanced performance, J. Memb. Sci. 451 (2014) 94–102. doi:10.1016/j.memsci.2013.09.018.

[46] A. Fonseca, S. Nejati, M. Elimelech, Antimicrobial properties of graphene oxide nanosheets: Why size matters, ACS Nano. 9 (2015) 7226–7236. doi:10.1021/ascnano.5b02067.

[47] S. Liu, T.H. Zeng, M. Hofmann, E. Burcombe, J. Wei, R. Jiang, J. Kong, Y. Chen, Antibacterial activity of graphite, graphite oxide, graphene oxide, and reduced graphene oxide: Membrane and oxidative stress, ACS Nano. 5 (2011) 6971–6980. doi:10.1021/nn202451x.

[48] J. Shen, M. Zhang, G. Liu, K. Guan, W. Jin, Size Effects of Graphene Oxide on Mixed Matrix Membranes for CO2 Separation, AIChE J. 62 (2016) 2843–2851. doi:10.1002/aic.

[49] Z.H. Wu, H.B. Chen, Y.M. Dong, H.L. Mao, J.L. Sun, S.F. Chen, V.S.J. Craig, J. Hu, Cleaning using nanobubbles: Defouling by electrochemical generation of bubbles, J. Colloid Interface Sci. 328 (2008) 10–14. doi:10.1016/j.jcis.2008.08.064.

[50] C.A. Martínez-Huitle, S. Ferro, Electrochemical oxidation of organic pollutants for the wastewater treatment: Direct and indirect processes, Chem. Soc. Rev. 35 (2006) 1324–1340. doi:10.1039/b517632h.

[51] H. Särkkä, A. Bhatnagar, M. Sillanpää, Recent developments of electro-oxidation in water treatment - A review, J. Electroanal. Chem. 754 (2015) 46–56. doi:10.1016/j.jelechem.2015.06.016.

[52] E. Brillas, I. Sire, M.A. Oturan, Electro-Fenton Process and Related Electrochemical Technologies Based on Fenton ' s Reaction Chemistry, (2009) 6570–6631.

[53] F.C. Moreira, R.A.R. Boaventura, E. Brillas, V.J.P. Vilar, Applied Catalysis B : Environmental Electrochemical advanced oxidation processes : A review on their application to synthetic and real wastewaters, "Applied Catal. B, Environ. 202 (2017) 217–261. doi:10.1016/j.apcatb.2016.08.037.

[54] B. Khorshidi, J. Hajinasiri, G. Ma, S. Bhattacharjee, M. Sadrzadeh, Thermally resistant and electrically conductive PES/ITO nanocomposite membrane, J. Memb. Sci. 500 (2016) 151–160. doi:10.1016/j.memsci.2015.11.015.

[55] K.C. Ho, Y.H. Teow, A.W. Mohammad, W.L. Ang, P.H. Lee, Development of graphene oxide (GO)/multi-walled carbon nanotubes (MWCNTs) nanocomposite conductive membranes for electrically enhanced fouling mitigation, J. Memb. Sci. 552 (2018) 189–201. doi:10.1016/j.memsci.2018.02.001.

[56] J. Huang, Z. Wang, J. Zhang, X. Zhang, J. Ma, Z. Wu, A novel composite conductive microfiltration membrane and its anti-fouling performance with an external electric field

in membrane bioreactors, Sci. Rep. 5 (2015) 1–8. doi:10.1038/srep09268.

[57] Y. Liu, W. Tu, M. Chen, L. Ma, B. Yang, Q. Liang, Y. Chen, A mussel-induced method to fabricate reduced graphene oxide / halloysite nanotubes membranes for multifunctional applications in water puri fi cation and oil / water separation G RA P H I C A L AB S T R A C T, Chem. Eng. J. 336 (2018) 263–277. doi:10.1016/j.cej.2017.12.043.

[58] A. V. Dudchenko, J. Rolf, K. Russell, W. Duan, D. Jassby, Organic fouling inhibition on electrically conducting carbon nanotube-polyvinyl alcohol composite ultrafiltration membranes, J. Memb. Sci. 468 (2014) 1–10. doi:10.1016/j.memsci.2014.05.041.

[59] W. Duan, A. Ronen, S. Walker, D. Jassby, Polyaniline-Coated Carbon Nanotube Ultrafiltration Membranes: Enhanced Anodic Stability for in Situ Cleaning and Electro-Oxidation Processes, ACS Appl. Mater. Interfaces. 8 (2016) 22574–22584. doi:10.1021/acsami.6b07196.

[60] M. Hu, B. Mi, Enabling graphene oxide nanosheets as water separation membranes, Environ. Sci. Technol. 47 (2013) 3715–3723. doi:10.1021/es400571g.

[61] R. Rezaee, S. Nasseri, A.H. Mahvi, R. Nabizadeh, S.A. Mousavi, A. Rashidi, A. Jafari, S. Nazmara, Fabrication and characterization of a polysulfone-graphene oxide nanocomposite membrane for arsenate rejection from water, J. Environ. Heal. Sci. Eng. (2015) 1–11. doi:10.1186/s40201-015-0217-8.

[62] A. Seidel, M. Elimelech, Coupling between chemical and physical interactions in natural organic matter (NOM) fouling of nanofiltration membranes : implications for fouling control, J. Memb. Sci. 203 (2002) 245–255.

[63] S. Hong, M. Elimelech, Chemical and physical aspects of natural organic matter (NOM) fouling of nanofiltration membranes, J. Memb. Sci. 132 (1997) 159–181. doi:10.1016/S0376-7388(97)00060-4.

[64] D. Rana, T. Matsuura, Surface modifications for antifouling membranes, Chem. Rev. 110 (2010) 2448–2471. doi:10.1021/cr800208y.

[65] D.J. Miller, D.R. Dreyer, C.W. Bielawski, D.R. Paul, B.D. Freeman, Surface Modification of Water Purification Membranes, Angew.Chem.Int. 56 (2017) 4662–4711. doi:10.1002/anie.201601509.

[66] B. Khorshidi, B. Soltannia, T. Thundat, M. Sadrzadeh, Synthesis of thin film composite polyamide membranes: Effect of monohydric and polyhydric alcohol additives in aqueous solution, J. Memb. Sci. 523 (2017) 336–345. doi:10.1016/j.memsci.2016.09.062.

[67] O. Burtovyy, V. Klep, T. Turel, Y. Gowayed, I. Luzinov, Polymeric membranes: Surface modification by “grafting to” method and fabrication of multilayered assemblies, ACS Symp. Ser. 1016 (2009) 289–305. doi:10.1021/bk-2009-1016.ch022.

[68] J.M. Grace, L.J. Gerenser, Plasma Treatment of Polymers, J. Dispers. Sci. Technol. 24 (2003) 305–341. doi:10.1081/DIS-120021793.

[69] E.F. Castro Vidaurre, C. a. Achete, F. Gallo, D. Garcia, R. Simão, a. C. Habert, Surface Modification of Polymeric Materials by Plasma Treatment, Mater. Res. 5 (2002) 37–41. doi:10.1590/S1516-14392002000100006.

[70] M. Amirilargani, M. Sadrzadeh, T. Mohammadi, Synthesis and characterization of polyethersulfone membranes, J. Polym. Res. 17 (2009) 363–377. doi:10.1007/s10965-009-9323-6.

[71] Y. Zhang, P. Liu, Preparation of porous ZrO2 solid superacid shell/void/TiO2 core particles and effect of doping them on PVDF membranes properties, Chem. Eng. Sci. 135 (2015) 67–75. doi:10.1016/j.ces.2015.06.037.

[72] A. Bottino, G. Capannelli, A. Comite, Preparation and characterization of novel porous PVDF-Zr02 composite membranes, 146 (2002) 35–40.

[73] J. Shen, H. Ruan, L. Wu, C. Gao, Preparation and characterization of PES – SiO 2 organic – inorganic composite ultrafiltration membrane for raw water pretreatment, 168 (2011) 1272–1278. doi:10.1016/j.cej.2011.02.039.

[74] V. Moghimifar, A.E. Livari, A. Raisi, A. Aroujalian, RSC Advances Enhancing the antifouling property of polyethersulfone ultra fi ltration membranes using NaX zeolite and titanium oxide nanoparticles, RSC Adv. 5 (2015) 55964–55976. doi:10.1039/C5RA06986F.

[75] L. Wang, X. Song, T. Wang, S. Wang, Z. Wang, C. Gao, Applied Surface Science Fabrication and characterization of polyethersulfone / carbon nanotubes (PES / CNTs) based mixed matrix membranes (MMMs) for nanofiltration application, Appl. Surf. Sci. 330 (2015) 118–125. doi:10.1016/j.apsusc.2014.12.183.

[76] E. Celik, H. Park, H. Choi, H. Choi, Carbon nanotube blended polyethersulfone membranes for fouling control in water treatment, Water Res. 45 (2011) 274–282. doi:10.1016/j.watres.2010.07.060.

[77] D. Zhang, A. Karkooti, L. Liu, M. Sadrzadeh, T. Thundat, Y. Liu, R. Narain, Fabrication of antifouling and antibacterial polyethersulfone (PES)/cellulose nanocrystals (CNC) nanocomposite membranes, J. Memb. Sci. 549 (2017) 350–356. doi:10.1016/j.memsci.2017.12.034.

[78] G. Mittal, V. Dhand, K.Y. Rhee, S.-J. Park, W.R. Lee, A review on carbon nanotubes and graphene as fillers in reinforced polymer nanocomposites, J. Ind. Eng. Chem. 21 (2015) 11–25. doi:10.1016/j.jiec.2014.03.022.

[79] H. Kim, A.A. Abdala, C.W. MacOsko, Graphene/polymer nanocomposites, Macromolecules. 43 (2010) 6515–6530. doi:10.1021/ma100572e.

[80] K. Hu, D.D. Kulkarni, I. Choi, V. V. Tsukruk, Graphene-polymer nanocomposites for structural and functional applications, Prog. Polym. Sci. 39 (2014) 1934–1972. doi:10.1016/j.progpolymsci.2014.03.001.

[81] O.C. Compton, S.T. Nguyen, Graphene oxide, highly reduced graphene oxide, and graphene: Versatile building blocks for carbon-based materials, Small. 6 (2010) 711–723. doi:10.1002/smll.200901934.

[82] L. Yu, Y. Zhang, B. Zhang, J. Liu, H. Zhang, C. Song, Preparation and characterization of HPEI-GO/PES ultrafiltration membrane with antifouling and antibacterial properties, J. Memb. Sci. 447 (2013) 452–462. doi:10.1016/j.memsci.2013.07.042.

[83] M.Y. Lim, Y.S. Choi, J. Kim, K. Kim, H. Shin, J.J. Kim, D.M. Shin, J.C. Lee, Cross-

linked graphene oxide membrane having high ion selectivity and antibacterial activity prepared using tannic acid-functionalized graphene oxide and polyethyleneimine, J. Memb. Sci. 521 (2017) 1–9. doi:10.1016/j.memsci.2016.08.067.

[84] Z. Xu, J. Zhang, M. Shan, Y. Li, B. Li, J. Niu, B. Zhou, X. Qian, Organosilane-functionalized graphene oxide for enhanced antifouling and mechanical properties of polyvinylidene fluoride ultrafiltration membranes, J. Memb. Sci. 458 (2014) 1–13. doi:10.1016/j.memsci.2014.01.050.

[85] S. Sadeghi, A. Zehtab Yazdi, U. Sundararaj, Controlling Short-Range Interactions by Tuning Surface Chemistry in HDPE/Graphene Nanoribbon Nanocomposites, J. Phys. Chem. B. 119 (2015) 11867–11878. doi:10.1021/acs.jpcb.5b03558.

[86] A.Z. Yazdi, K. Chizari, A.S. Jalilov, J. Tour, U. Sundararaj, A. Zehtab Yazdi, K. Chizari, A.S. Jalilov, J. Tour, U. Sundararaj, Helical and Dendritic Unzipping of Carbon Nanotubes: A Route to Nitrogen-Doped Graphene Nanoribbons, ACS Nano. (2015) 5833–5845. doi:10.1021/acsnano.5b02197.

[87] A. Zehtab Yazdi, H. Fei, R. Ye, G. Wang, J. Tour, U. Sundararaj, Boron/nitrogen co-doped helically unzipped multiwalled carbon nanotubes as efficient electrocatalyst for oxygen reduction, ACS Appl. Mater. Interfaces. 7 (2015) 7786–7794. doi:10.1021/acsami.5b01067.

[88] A.L. Higginbotham, D. V Kosynkin, A. Sinitskii, Z. Sun, J.M. Tour, Lower-Defect Graphene Oxide Nanotubes, 4 (2010) 2059–2069.

[89] D. V. Kosynkin, A.L. Higginbotham, A. Sinitskii, J.R. Lomeda, A. Dimiev, B.K. Price, J.M. Tour, Longitudinal unzipping of carbon nanotubes to form graphene nanoribbons, Nature. 458 (2009) 872–876. doi:10.1038/nature07872.

[90] V. Vatanpour, S.S. Madaeni, R. Moradian, S. Zinadini, B. Astinchap, Novel antibifouling nanofiltration polyethersulfone membrane fabricated from embedding TiO2 coated multiwalled carbon nanotubes, Sep. Purif. Technol. 90 (2012) 69–82. doi:10.1016/j.seppur.2012.02.014.

[91] E. Saljoughi, M. Sadrzadeh, T. Mohammadi, Effect of preparation variables on morphology and pure water permeation flux through asymmetric cellulose acetate membranes, J. Memb. Sci. 326 (2009) 627–634.

[92] V.R.S.S. Mokkapati, D.Y. Koseoglu-Imer, N. Yilmaz-Deveci, I. Mijakovic, I. Koyuncu, Membrane properties and anti-bacterial/anti-biofouling activity of polysulfone–graphene oxide composite membranes phase inversed in graphene oxide non-solvent, RSC Adv. 7 (2017) 4378–4386. doi:10.1039/C6RA25015G.

[93] K.C. Khulbe, C. Feng, T. Matsuura, Synthetic Polymeric Membranes, Characterization by Atomic Force Microscopy, Springer, 2008. doi:10.1007/978-3-540-73994-4.

[94] D. V. Bavykin, E. V. Milsom, F. Marken, D.H. Kim, D.H. Marsh, D.J. Riley, F.C. Walsh, K.H. El-Abiary, A.A. Lapkin, A novel cation-binding TiO2 nanotube substrate for electro-catalysis and bioelectro-catalysis, Electrochem. Commun. 7 (2005) 1050–1058.

[95] M. Hayatbakhsh, M. Sadrzadeh, D. Pernitsky, S. Bhattacharjee, J. Hajinasiri, Treatment of an in situ oil sands produced water by polymeric membranes, Desalin. Water Treat. 57

(2016) 14869–14887.

[96] X. Zhao, J. Ma, Z. Wang, G. Wen, J. Jiang, F. Shi, L. Sheng, Hyperbranched-polymer functionalized multi-walled carbon nanotubes for poly (vinylidene fluoride) membranes: From dispersion to blended fouling-control membrane, Desalination. 303 (2012) 29–38. doi:10.1016/j.desal.2012.07.009.

[97] M. Sadrzadeh, S. Bhattacharjee, Rational design of phase inversion membranes by tailoring thermodynamics and kinetics of casting solution using polymer additives, J. Memb. Sci. 441 (2013) 31–44. doi:10.1016/j.memsci.2013.04.009.

[98] V. Vatanpour, S.S. Madaeni, L. Rajabi, S. Zinadini, A.A. Derakhshan, Boehmite nanoparticles as a new nanofiller for preparation of antifouling mixed matrix membranes, J. Memb. Sci. 401–402 (2012) 132–143. doi:10.1016/j.memsci.2012.01.040.

[99] P. Wang, J. Ma, Z. Wang, F. Shi, Q. Liu, Enhanced separation performance of PVDF/PVP-g-MMT nanocomposite ultrafiltration membrane based on the NVP-grafted polymerization modification of montmorillonite (MMT), Langmuir. 28 (2012) 4776–4786. doi:10.1021/la203494z.

[100] S. Lentsch, P. Aimar, J.L. Orozco, Separation albumin-PEG: Transmission of PEG through ultrafiltration membranes, Biotechnol. Bioeng. 41 (1993) 1039–1047. doi:10.1002/bit.260411106.

[101] V. Kochkodan, D.J. Johnson, N. Hilal, Polymeric membranes: Surface modification for minimizing (bio)colloidal fouling, Adv. Colloid Interface Sci. 206 (2014) 116–140. doi:10.1016/j.cis.2013.05.005.

[102] V. Kochkodan, Reduction of Membrane Fouling by Polymer Surface Modification, in: Membr. Modif. Technol. Appl., CRC Press, 2012: pp. 41–76. doi:doi:10.1201/b12160-4.

[103] C. Bellona, J.E. Drewes, The role of membrane surface charge and solute physico-chemical properties in the rejection of organic acids by NF membranes, J. Memb. Sci. 249 (2005) 227–234. doi:10.1016/j.memsci.2004.09.041.

[104] A. Maiti, M. Sadrzadeh, S. Guha Thakurta, D.J. Pernitsky, S. Bhattacharjee, Characterization of boiler blowdown water from steam-assisted gravity drainage and silica–organic coprecipitation during acidification and ultrafiltration, Energy & Fuels. 26 (2012) 5604–5612. doi:10.1021/ef300865e.

[105] M. Kyomoto, K. Ishihara, Self-initiated surface graft polymerization of 2-methacryloyloxyethyl phosphorylcholine on poly(ether ether ketone) by photoirradiation, ACS Appl. Mater. Interfaces. 1 (2009) 537–542. doi:10.1021/am800260t.

[106] V. Mévellec, S. Roussel, L. Tessier, J. Chancolon, M. Mayne-L'Hermite, G. Deniau, P. Viel, S. Palacin, Grafting polymers on surfaces: A new powerful and versatile diazonium salt-based one-step process in aqueous media, Chem. Mater. 19 (2007) 6323–6330. doi:10.1021/cm071371i.

[107] K.S. Kim, K.H. Lee, K. Cho, C.E. Park, Surface modification of polysulfone ultrafiltration membrane by oxygen plasma treatment, 199 (2002) 135–145.

[108] A. Al-jumaili, S. Alancherry, D. Grant, A. Kumar, K. Bazaka, M. V Jacob, Plasma Treatment of Polymeric Membranes, Elsevier Inc., 2019. doi:10.1016/B978-0-12-813152-

7.00008-1.

[109] B. Khorshidi, S. Abolhassan, G. Ma, M. Mcgregor, M. Sadrzadeh, Novel nanocomposite polyethersulfone- antimony tin oxide membrane with enhanced thermal , electrical and antifouling properties, Polymer (Guildf). 163 (2019) 48–56. doi:10.1016/j.polymer.2018.12.058.

[110] A. Asad, M. Sadrzadeh, D. Sameoto, Direct Micropatterning of Phase Separation Membranes Using Hydrogel Soft Lithography, 1800384 (2019) 1–8. doi:10.1002/admt.201800384.

[111] A. Karkooti, A.Z. Yazdi, P. Chen, M. McGregor, N. Nazemifard, M. Sadrzadeh, Development of advanced nanocomposite membranes using graphene nanoribbons and nanosheets for water treatment, J. Memb. Sci. (2018). doi:10.1016/j.memsci.2018.04.034.

[112] J.A. Brant, A.E. Childress, Assessing short-range membrane-colloid interactions using surface energetics, J. Memb. Sci. 203 (2002) 257–273. doi:10.1016/S0376-7388(02)00014-5.

[113] N. Subhi, A.R.D. Verliefde, V. Chen, P. Le-Clech, Assessment of physicochemical interactions in hollow fibre ultrafiltration membrane by contact angle analysis, J. Memb. Sci. 403–404 (2012) 32–40. doi:10.1016/j.memsci.2012.02.007.

[114] M. Chaudhury, G.M. Whitesides, Correlation Between Surface Free Energy and Surface Constitution, Science (80-.). 255 (1992) 1230–1232.

[115] Z. Lijian, G.M. Whitesides, Acid-Base Properties of Organic Quantifying Functional Groups at a Polyethylene-Water Interface by Photoacoustic Calorimetry, J. Am. Chem. Soc. 112 (1990) 7070.

[116] G.M. Whitesides, H.A. Biebuyck, J.P. Folkers, K.L. Prime, Acid-base interactions in wetting, 69 (n.d.) 57–69.

[117] I. Macromolecular, G.M. Whitesides, Polymer Surfaces and lntertaces - Key to High Performance Materials Organic Surface Ghemistry : Polymers and Self-Assembled Monolayers, in: Chimia (Aarau)., 1990: pp. 310–311.

[118] S. Chen, L. Li, C. Zhao, J. Zheng, Surface hydration : Principles and applications toward low-fouling / nonfouling biomaterials, Polymer (Guildf). 51 (2010) 5283–5293. doi:10.1016/j.polymer.2010.08.022.

[119] C.J. van Oss, Interfacial Forces in Aqueous Media, CRC Press, Taylor & Francis Group, 2006.

[120] A. Subramani, X. Huang, E.M.V. Hoek, Direct observation of bacterial deposition onto clean and organic-fouled polyamide membranes, J. Colloid Interface Sci. 336 (2009) 13–20. doi:10.1016/j.jcis.2009.03.063.

[121] S. Kang, A. Subramani, E.M. V Hoek, M.A. Deshusses, M.R. Matsumoto, Direct observation of biofouling in cross-flow microfiltration : mechanisms of deposition and release, 244 (2004) 151–165. doi:10.1016/j.memsci.2004.07.011.

[122] S. Lee, S. Kim, J. Cho, E.M. V Hoek, Natural organic matter fouling due to foulant-membrane physicochemical interactions, Desalination. 202 (2007) 377–384.

doi:10.1016/j.desal.2005.12.077.

[123] S. Wang, G. Guillen, E.M.V. Hoek, Direct Observation of Microbial Adhesion to Membranes †, Environ. Sci. Tecnol. 39 (2005) 6461–6469. doi:10.1021/es050188s.

[124] A.E. Contreras, Z. Steiner, J. Miao, R. Kasher, Q. Li, Studying the role of common membrane surface functionalities on adsorption and cleaning of organic foulants using QCM-D, Environ. Sci. Technol. 45 (2011) 6309–6315. doi:10.1021/es200570t.

[125] N. Abdel-Aal, K. Satoh, K. Sawada, Study of the adhesion mechanism of CaCO3 using a combined bulk chemistry/QCM technique, J. Cryst. Growth. 245 (2002) 87–100. doi:10.1016/S0022-0248(02)01657-3.

[126] P. RG, N. Yang, S. Thi, J. Fatema, M. Sadrzadeh, D. Pernitsky, Characterization and Comparison of Dissolved Organic Matter Signatures in Steam-Assisted Gravity Drainage Process Water Samples from Athabasca Oil Sands, Energy & Fuels. 31 (2017) 8363–8373. doi:10.1021/acs.energyfuels.7b00483.

[127] C.J. van Oss, Acid—base interfacial interactions in aqueous media, Colloids Surfaces A Physicochem. Eng. Asp. 78 (1993) 1–49. doi:10.1016/0927-7757(93)80308-2.

[128] Q. Wang, Z. Wang, J. Zhang, J. Wang, Z. Wu, Antifouling behaviours of PVDF/nano-TiO2 composite membranes revealed by surface energetics and quartz crystal microbalance monitoring, RSC Adv. 4 (2014) 43590–43598. doi:10.1039/C4RA07274J.

[129] D. Briggs, B.J. Briscoe, P. Science, Young-Dupre Equation Learn more about Young-Dupre Equation Polymer Properties, in: Compr. Polym. Sci. Suppl., 1989.

[130] D.Y. Kwok, The usefulness of the Lifshitz – van der Waals / acid – base approach for surface tension components and interfacial tensions, 156 (1999) 191–200.

[131] L. Gourley, M. Britten, S.F. Gauthier, Y. Pouliot, Characterization of adsorptive fouling on ultrafiltration membranes by peptides mixtures using contact angle measurements, J. Memb. Sci. 97 (1994) 283–289. doi:10.1016/0376-7388(94)00172-U.

[132] G. Wolansky, A. Marmur, The Actual Contact Angle on a Heterogeneous Rough Surface in Three Dimensions, Langmuir. 14 (1998) 5292–5297. doi:10.1021/la960723p.

[133] C.R. Bouchard, J. Jolicoeur, P. Kouadio, M. Britten, Study of Humic Acid Adsorption on Nanofiltration Membranes by Contact Angle Measurements, Can. J. Chem. Eng. 75 (1997) 339–345. doi:10.1002/cjce.5450750209.

[134] M. Greiveldinger, M.E.R. Shanahan, A critique of the mathematical coherence of acid/base interfacial free energy theory, J. Colloid Interface Sci. 215 (1999) 170–178. doi:10.1006/jcis.1999.6259.

[135] C.J. van Oss, R.J. Good, Orientation of the water molecules of hydration of human serum albumin, J. Protein Chem. 7 (1988) 179–183. doi:10.1007/BF01025248.

[136] S. Bhattacharjee, A. Sharma, P.K. Bhattacharya, Surface Interactions in Osmotic Pressure Controlled Flux Decline during Ultrafiltration, Langmuir. 10 (1994) 4710–4720. doi:10.1021/la00024a053.

[137] S. Kim, E.M. V Hoek, Interactions controlling biopolymer fouling of reverse osmosis membranes, Desalination. 202 (2007) 333–342. doi:10.1016/j.desal.2005.12.072.

[138] V.M. Mecea, Loaded vibrating quartz sensors, Sensors Actuators, A Phys. 40 (1994) 1–27. doi:10.1016/0924-4247(94)85026-7.

[139] K.K. Kanazawa, O.R. Melroy, The quartz resonator: Electrochemical applications, IBM J. Res. Dev. 37 (1993) 157–171. doi:10.1147/rd.372.0157.

[140] E. Benes, Improved quartz crystal microbalance technique, J. Appl. Phys. 56 (1984) 608–626. doi:10.1063/1.333990.

[141] E. Saljoughi, M. Amirilargani, T. Mohammadi, Effect of PEG additive and coagulation bath temperature on the morphology, permeability and thermal/chemical stability of asymmetric CA membranes, Desalination. 262 (2010) 72–78. doi:10.1016/j.desal.2010.05.046.

[142] H. Salehi, A. Shakeri, M. Rastgar, Carboxylic polyethersulfone: A novel pH-responsive modifier in support layer of forward osmosis membrane, J. Memb. Sci. 548 (2018) 641–653. doi:10.1016/j.memsci.2017.10.044.

[143] S.A. Al Malek, M.N. Abu Seman, D. Johnson, N. Hilal, Formation and characterization of polyethersulfone membranes using different concentrations of polyvinylpyrrolidone, Desalination. 288 (2012) 31–39. doi:10.1016/j.desal.2011.12.006.

[144] T.G. Tshabalala, E.N. Nxumalo, B.B. Mamba, S.D. Mhlanga, Synthesis of robust flexible polyethersulfone ultrafiltration membranes supported on non-woven fabrics for separation of NOM from water, Water SA. 42 (2016) 621–632. doi:10.4314/wsa.v42i4.13.

[145] I.M. Wienk, R.M. Boom, M.A.M. Beerlage, A.M.W. Bulte, C.A. Smolders, H. Strathmann, Recent advances in the formation of phase inversion membranes made from amorphous or semi-crystalline polymers, 113 (1996) 361–371.

[146] M. Rastgar, A. Shakeri, A. Bozorg, H. Salehi, V. Saadattalab, Highly-efficient forward osmosis membrane tailored by magnetically responsive graphene oxide/Fe3O4nanohybrid, Appl. Surf. Sci. 441 (2018) 923–935. doi:10.1016/j.apsusc.2018.02.118.

[147] H. SUSANTO, M. ULBRICHT, Influence of ultrafiltration membrane characteristics on adsorptive fouling with dextrans, J. Memb. Sci. 266 (2005) 132–142. doi:10.1016/j.memsci.2005.05.018.

[148] Y.N. Wang, C.Y. Tang, Protein fouling of nanofiltration, reverse osmosis, and ultrafiltration membranes-The role of hydrodynamic conditions, solution chemistry, and membrane properties, J. Memb. Sci. 376 (2011) 275–282. doi:10.1016/j.memsci.2011.04.036.

[149] M. Kawahigashi, N. Fujitake, H. Yajima, H. Sumida, Particle Sizes of Standard Humic Substances Calculated as Radii of Gyration , Maximum Diameter and Hydrodynamic Radii, (n.d.) 13–18.

[150] M. Kawahigashi, H. Sumida, K. Yamamoto, Size and shape of soil humic acids estimated by viscosity and molecular weight, J. Colloid Interface Sci. 284 (2005) 463–469. doi:10.1016/j.jcis.2004.10.023.

[151] M. Sadrzadeh, J. Hajinasiri, S. Bhattacharjee, D. Pernitsky, Nanofiltration of oil sands boiler feed water: Effect of pH on water flux and organic and dissolved solid rejection,

Sep. Purif. Technol. 141 (2015). doi:10.1016/j.seppur.2014.12.011.

[152] M. Hashino, K. Hirami, T. Katagiri, N. Kubota, Y. Ohmukai, T. Ishigami, T. Maruyama, H. Matsuyama, Effects of three natural organic matter types on cellulose acetate butyrate microfiltration membrane fouling, J. Memb. Sci. 379 (2011) 233–238. doi:10.1016/J.MEMSCI.2011.05.068.

[153] J. Wu, A.E. Contreras, Q. Li, Studying the impact of RO membrane surface functional groups on alginate fouling in seawater desalination, J. Memb. Sci. 458 (2014) 120–127. doi:10.1016/j.memsci.2014.01.056.

[154] M.A. Shannon, P.W. Bohn, M. Elimelech, J.G. Georgiadis, B.J. Mariñas, A.M. Mayes, Science and technology for water purification in the coming decades, Nature. 452 (2008) 301–310. doi:10.1038/nature06599.

[155] M. Elimelech, W.A. Phillip, The Future of Seawater and the Environment: Energy, Technology, and the Environment, Science. 333 (2011) 712–718. doi:10.1126/science.1200488.

[156] M. Rastgar, A.R. Zolfaghari, H.R. Mortaheb, H. Sayahi, H.R. Naderi, Photocatalytic/adsorptive removal of methylene blue dye by electrophoretic nanostructured TiO2/montmorillonite composite films, J. Adv. Oxid. Technol. 16 (2013) 292–297. doi:10.1515/jaots-2013-0211.

[157] D.-Q. He, Y.-J. Zhang, D.-N. Pei, G.-X. Huang, C. Liu, J. Li, H.-Q. Yu, Degradation of benzoic acid in an advanced oxidation process: The effects of reducing agents, J. Hazard. Mater. 382 (2020) 121090. doi:10.1016/j.jhazmat.2019.121090.

[158] Q. Xiang, Y. Nomura, S. Fukahori, T. Mizuno, H. Tanaka, T. Fujiwara, Innovative Treatment of Organic Contaminants in Reverse Osmosis Concentrate from Water Reuse: a Mini Review, Curr. Pollut. Reports. (2019). doi:10.1007/s40726-019-00119-2.

[159] P.C. Kamp, J.C. Kruithof, H.C. Folmer, UF/RO treatment plant Heemskerk: From challenge to full scale application, Desalination. 131 (2000) 27–35. doi:10.1016/S0011-9164(00)90003-1.

[160] M. Brienza, I.A. Katsoyiannis, Sulfate radical technologies as tertiary treatment for the removal of emerging contaminants from wastewater, Sustain. 9 (2017) 1604. doi:10.3390/su9091604.

[161] S. Lee, J. Kim, C.H. Lee, Analysis of CaSO4 scale formation mechanism in various nanofiltration modules, J. Memb. Sci. 163 (1999) 63–74. doi:10.1016/S0376-7388(99)00156-8.

[162] A. Bogler, S. Lin, E. Bar-Zeev, Biofouling of membrane distillation, forward osmosis and pressure retarded osmosis: Principles, impacts and future directions, J. Memb. Sci. 542 (2017) 378–398. doi:10.1016/j.memsci.2017.08.001.

[163] H. Salehi, M. Rastgar, A. Shakeri, Anti-fouling and high water permeable forward osmosis membrane fabricated via layer by layer assembly of chitosan/graphene oxide, Appl. Surf. Sci. 413 (2017) 99–108. doi:10.1016/j.apsusc.2017.03.271.

[164] M. Masuelli, J. Marchese, N.A. Ochoa, SPC/PVDF membranes for emulsified oily wastewater treatment, J. Memb. Sci. 326 (2009) 688–693.

doi:10.1016/J.MEMSCI.2008.11.011.

[165] B. Khorshidi, I. Biswas, T. Ghosh, T. Thundat, M. Sadrzadeh, Robust fabrication of thin film polyamide-TiO 2 nanocomposite membranes with enhanced thermal stability and anti-biofouling propensity, Sci. Rep. 8 (2018) 784. doi:10.1038/s41598-017-18724-w.

[166] G.V. Dizon, A. Venault, Direct in-situ modification of PVDF membranes with a zwitterionic copolymer to form bi-continuous and fouling resistant membranes, J. Memb. Sci. 550 (2018) 45–58. doi:10.1016/J.MEMSCI.2017.12.065.

[167] Z. Zeng, D. Yu, Z. He, J. Liu, F.X. Xiao, Y. Zhang, R. Wang, D. Bhattacharyya, T.T.Y. Tan, Graphene Oxide Quantum Dots Covalently Functionalized PVDF Membrane with Significantly-Enhanced Bactericidal and Antibiofouling Performances, Sci. Rep. 6 (2016) 1–11. doi:10.1038/srep20142.

[168] J. Yin, Y. Yang, Z. Hu, B. Deng, Attachment of silver nanoparticles (AgNPs) onto thin-film composite (TFC) membranes through covalent bonding to reduce membrane biofouling, J. Memb. Sci. 441 (2013) 73–82. doi:10.1016/j.memsci.2013.03.060.

[169] D. Wandera, S.R. Wickramasinghe, S.M. Husson, Stimuli-responsive membranes, J. Memb. Sci. 357 (2010) 6–35. doi:10.1016/j.memsci.2010.03.046.

[170] N. Hilal, O.O. Ogunbiyi, N.J. Miles, R. Nigmatullin, Methods Employed for Control of Fouling in MF and UF Membranes: A Comprehensive Review, Sep. Sci. Technol. 40 (2005) 1957–2005. doi:10.1081/SS-200068409.

[171] S. Darvishmanesh, X. Qian, S.R. Wickramasinghe, Responsive membranes for advanced separations, Curr. Opin. Chem. Eng. 8 (2015) 98–104. doi:10.1016/j.coche.2015.04.002.

[172] C. Trellu, B.P. Chaplin, C. Coetsier, R. Esmilaire, S. Cerneaux, C. Causserand, M. Cretin, Electro-oxidation of organic pollutants by reactive electrochemical membranes, Chemosphere. 208 (2018) 159–175. doi:10.1016/j.chemosphere.2018.05.026.

[173] F. Ahmed, B.S. Lalia, V. Kochkodan, N. Hilal, R. Hashaikeh, Electrically conductive polymeric membranes for fouling prevention and detection: A review, Desalination. 391 (2016) 1–15. doi:10.1016/j.desal.2016.01.030.

[174] A. V. Dudchenko, J. Rolf, K. Russell, W. Duan, D. Jassby, Organic fouling inhibition on electrically conducting carbon nanotube–polyvinyl alcohol composite ultrafiltration membranes, J. Memb. Sci. 468 (2014) 1–10. doi:10.1016/J.MEMSCI.2014.05.041.

[175] C.D. Vecitis, G. Gao, H. Liu, Electrochemical Carbon Nanotube Filter for Adsorption , Desorption , and Oxidation of Aqueous Dyes and Anions, (2011) 3621–3629. doi:10.1021/jp111844j.

[176] S.Y. Yang, C.D. Vecitis, H. Park, Electrocatalytic water treatment using carbon nanotube filters modified with metal oxides, Environ. Sci. Pollut. Res. 26 (2019) 1036–1043. doi:10.1007/s11356-017-8495-6.

[177] D. Rice, P. Westerhoff, F. Perreault, S. Garcia-Segura, Electrochemical self-cleaning anodic surfaces for biofouling control during water treatment, Electrochem. Commun. 96 (2018) 83–87. doi:10.1016/j.elecom.2018.10.002.

[178] C. Piyadasa, H.F. Ridgway, T.R. Yeager, M.B. Stewart, C. Pelekani, S.R. Gray, J.D.

Orbell, The application of electromagnetic fields to the control of the scaling and biofouling of reverse osmosis membranes - A review, Desalination. 418 (2017) 19–34. doi:10.1016/j.desal.2017.05.017.

[179] T.M. Qaisrani, W.M. Samhaber, Impact of gas bubbling and backflushing on fouling control and membrane cleaning, Desalination. 266 (2011) 154–161. doi:10.1016/j.desal.2010.08.019.

[180] M.A. Halali, C.-F. de Lannoy, The Effect of Cross-Linkers on the Permeability of Electrically Conductive Membranes, Ind. Eng. Chem. Res. 58 (2019) 3832–3844. doi:10.1021/acs.iecr.8b05691.

[181] X. Fan, Y. Liu, X. Quan, S. Chen, Highly Permeable Thin-Film Composite Forward Osmosis Membrane Based on Carbon Nanotube Hollow Fiber Scaffold with Electrically Enhanced Fouling Resistance, Environ. Sci. Technol. 52 (2018) 1444–1452. doi:10.1021/acs.est.7b05341.

[182] M. Rastgar, A. Bozorg, A. Shakeri, M. Sadrzadeh, Substantially improved antifouling properties in electro-oxidative graphene laminate forward osmosis membrane, Chem. Eng. Res. Des. 141 (2019) 413–424. doi:10.1016/j.cherd.2018.11.010.

[183] Y. Liu, J.H. Dustin Lee, Q. Xia, Y. Ma, Y. Yu, L.Y. Lanry Yung, J. Xie, C.N. Ong, C.D. Vecitis, Z. Zhou, A graphene-based electrochemical filter for water purification, J. Mater. Chem. A. 2 (2014) 16554–16562. doi:10.1039/c4ta04006f.

[184] Y. Zhang, W. Yu, R. Li, Y. Xu, L. Shen, H. Lin, B.Q. Liao, G. Wu, Novel conductive membranes breaking through the selectivity-permeability trade-off for Congo red removal, Sep. Purif. Technol. 211 (2019) 368–376. doi:10.1016/j.seppur.2018.10.008.

[185] K. Wang, L. Xu, K. Li, L. Liu, Y. Zhang, J. Wang, Development of polyaniline conductive membrane for electrically enhanced membrane fouling mitigation, J. Memb. Sci. 570–571 (2019) 371–379. doi:10.1016/j.memsci.2018.10.050.

[186] P. Wang, K.. Tan, E.. Kang, K.. Neoh, Preparation and characterization of semi-conductive poly(vinylidene fluoride)/polyaniline blends and membranes, Appl. Surf. Sci. 193 (2002) 36–45. doi:10.1016/S0169-4332(01)01031-5.

[187] L. Liu, J. Liu, G. Bo, F. Yang, J. Crittenden, Y. Chen, Conductive and hydrophilic polypyrrole modified membrane cathodes and fouling reduction in MBR, J. Memb. Sci. 429 (2013) 252–258. doi:10.1016/J.MEMSCI.2012.11.066.

[188] S. Ohmori, T. Saito, Electrochemical durability of single-wall carbon nanotube electrode against anodic oxidation in water, Carbon N. Y. 50 (2012) 4932–4938. doi:10.1016/J.CARBON.2012.06.023.

[189] A. Mirmohseni, A. Oladegaragoze, Anti-corrosive properties of polyaniline coating on iron, Synth. Met. 114 (2000) 105–108. doi:10.1016/S0379-6779(99)00298-2.

[190] X. Feng, N. Chen, J. Zhou, Y. Li, Z. Huang, L. Zhang, Y. Ma, L. Wang, X. Yan, Facile synthesis of shape-controlled graphene–polyaniline composites for high performance supercapacitor electrode materials, New J. Chem. 39 (2015) 2261–2268. doi:10.1039/C4NJ01843E.

[191] B. Mi, M. Elimelech, Chemical and physical aspects of organic fouling of forward

osmosis membranes, J. Memb. Sci. 320 (2008) 292–302. doi:10.1016/j.memsci.2008.04.036.

[192] C.J. Van Oss, W. Wu, A. Docoslis, R.F. Giese, The interfacial tensions with water and the Lewis acid-base surface tension parameters of polar organic liquids derived from their aqueous solubilities, Colloids Surfaces B Biointerfaces. 20 (2001) 87–91. doi:10.1016/S0927-7765(00)00169-7.

[193] M. Hayatbakhsh, M. Sadrzadeh, D. Pernitsky, S. Bhattacharjee, J. Hajinasiri, Treatment of an in situ oil sands produced water by polymeric membranes, Desalin. Water Treat. 57 (2016) 14869–14887. doi:10.1080/19443994.2015.1069216.

[194] R. Beckett, N.P. Le, The role or organic matter and ionic composition in determining the surface charge of suspended particles in natural waters, Colloids and Surfaces. 44 (1990) 35–49. doi:10.1016/0166-6622(90)80185-7.

[195] J.S. Park, H.J. Lee, S.J. Choi, K.E. Geckeler, J. Cho, S.H. Moon, Fouling mitigation of anion exchange membrane by zeta potential control, J. Colloid Interface Sci. 259 (2003) 293–300. doi:10.1016/S0021-9797(02)00095-4.

[196] S. Mclaughlln, Electrostatic Potentials at Membrane-Solution Interfaces, Interfaces.Curr. Top. Membr. Transp. 9 (1977) 71–144.

[197] G.C.C. Yang, C.J. Li, Electrofiltration of silica nanoparticle-containing wastewater using tubular ceramic membranes, Sep. Purif. Technol. 58 (2007) 159–165. doi:10.1016/j.seppur.2007.07.019.

[198] G.C.C. Yang, T.Y. Yang, S.H. Tsai, Crossflow electro-microfiltration of oxide-CMP wastewater, Water Res. 37 (2003) 785–792. doi:10.1016/S0043-1354(02)00388-3.

[199] M. Razmkhah, F. Moosavi, M.T.H. Mosavian, A. Ahmadpour, Does electric or magnetic field affect reverse osmosis desalination?, Desalination. 432 (2018) 55–63. doi:10.1016/j.desal.2017.12.062.

[200] M. Panizza, G. Cerisola, Direct and mediated anodic oxidation of organic pollutants, Chem. Rev. 109 (2009) 6541–6569. doi:10.1021/cr9001319.

[201] E. Brillas, I. Sirés, M. a. Oturan, Electro-Fenton Process and Related Electrochemical Technologies Based on Fenton's Reaction Chemistry, Chem. Rev. 109 (2009) 6570–6631. doi:10.1021/cr900136g.

[202] E. BRILLAS, A. MAESTRO, M. MORATALLA, J. CASADO, Electrochemical extraction of oxygen from air via hydroperoxide ion, J. Appl. Electrochem. 27 (1997) 83–92. doi:10.1023/A:1026475117836.

[203] G V Buxton, C.L. Greenstock, W.P. Helman, A.B. Ross, Critical Review of rate constants for reactions of hydrated electrons, hydrogen atoms and hydroxyl radicals (·OH/·O − in Aqueous Solution, J. Phys. Chem. Ref. Data. 17 (1988) 513–886. doi:10.1063/1.555805.

[204] I. Sirés, E. Brillas, M.A. Oturan, M.A. Rodrigo, M. Panizza, Electrochemical advanced oxidation processes : today and tomorrow . A review, Env. Sci Pollut Res. 21 (2014) 8336–8367. doi:10.1007/s11356-014-2783-1.

[205] A.R.F. Pipi, I. Sirés, A.R. De Andrade, E. Brillas, Application of electrochemical

advanced oxidation processes to the mineralization of the herbicide diuron, Chemosphere. 109 (2014) 49–55. doi:10.1016/j.chemosphere.2014.03.006.

Appendix A

A1. Magnified C1s and O1s from XPS survey spectra

Magnified survey spectra (Figure A1) clearly show that C1s peak of GNP is more intense than other nanofillers. Other nanofillers almost show the same intensity of C1s. On the other hand, O1s peak is more prominent for more hydrophilic GONR-H and GONR-L nanofillers.

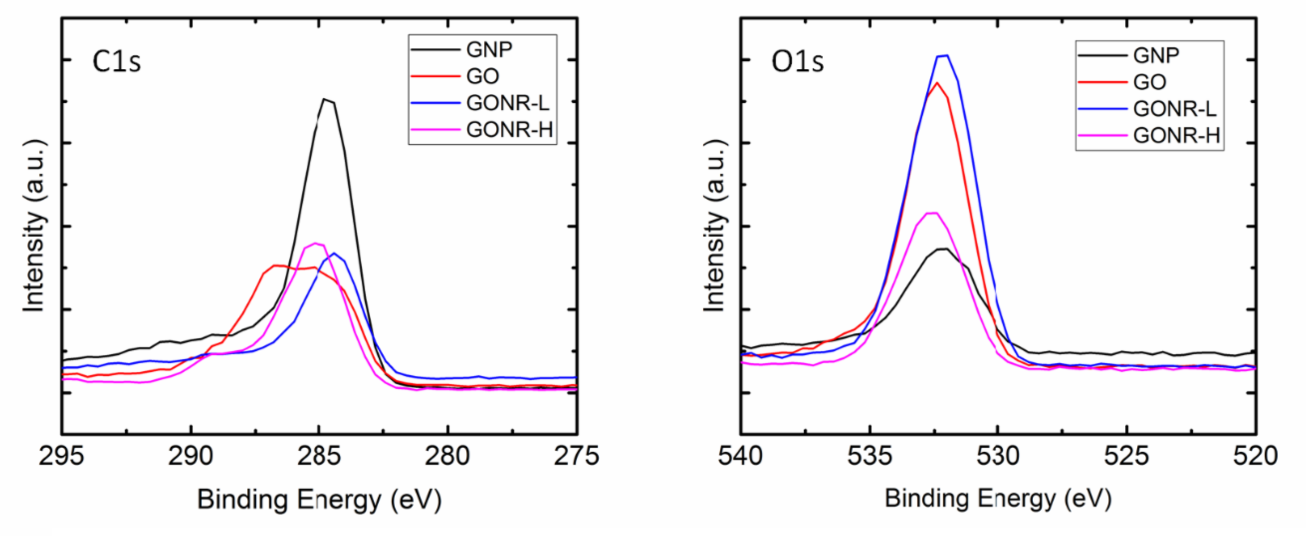

Figure A1. Magnified C1s and O1s of XPS survey spectra of GNP, GO, GONR-L, and GONR-H. Carbon to oxygen ratio (C/O) for GO, GONR-L, GONR-H, and GNP is 2.04, 1.05, 3.10 and 8.01, respectively.

A2. Casting solution viscosity at different shear rates

As shown in Fig. A2, the viscosity of casting solution increased by increasing the GO content in the casting solution which caused a delay in solvent/nonsolvent demixing and thus suppressed the formation of large pores. The delayed demixing also increased the thickness of skin layer in the synthesized phase inversion membranes.

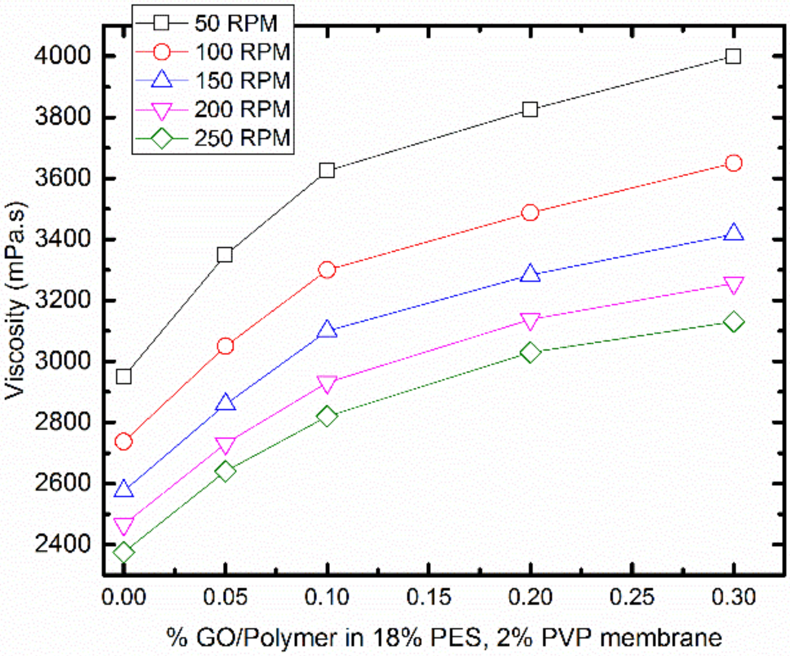

Figure A2. Viscosity of casting solution vs. loading of GO nanofillers at different shear rates

A3. Water flux vs. pressure for different concentration of nanofillers

The slope of lines in Figure A3 is the hydraulic permeability (LMH/psi) of membranes. As can be observed in this figure, the addition of nanofillers up to 0.1 wt.% first increased the hydraulic permeability then decreased it when the nanofiller content increased to 0.2 wt.%.

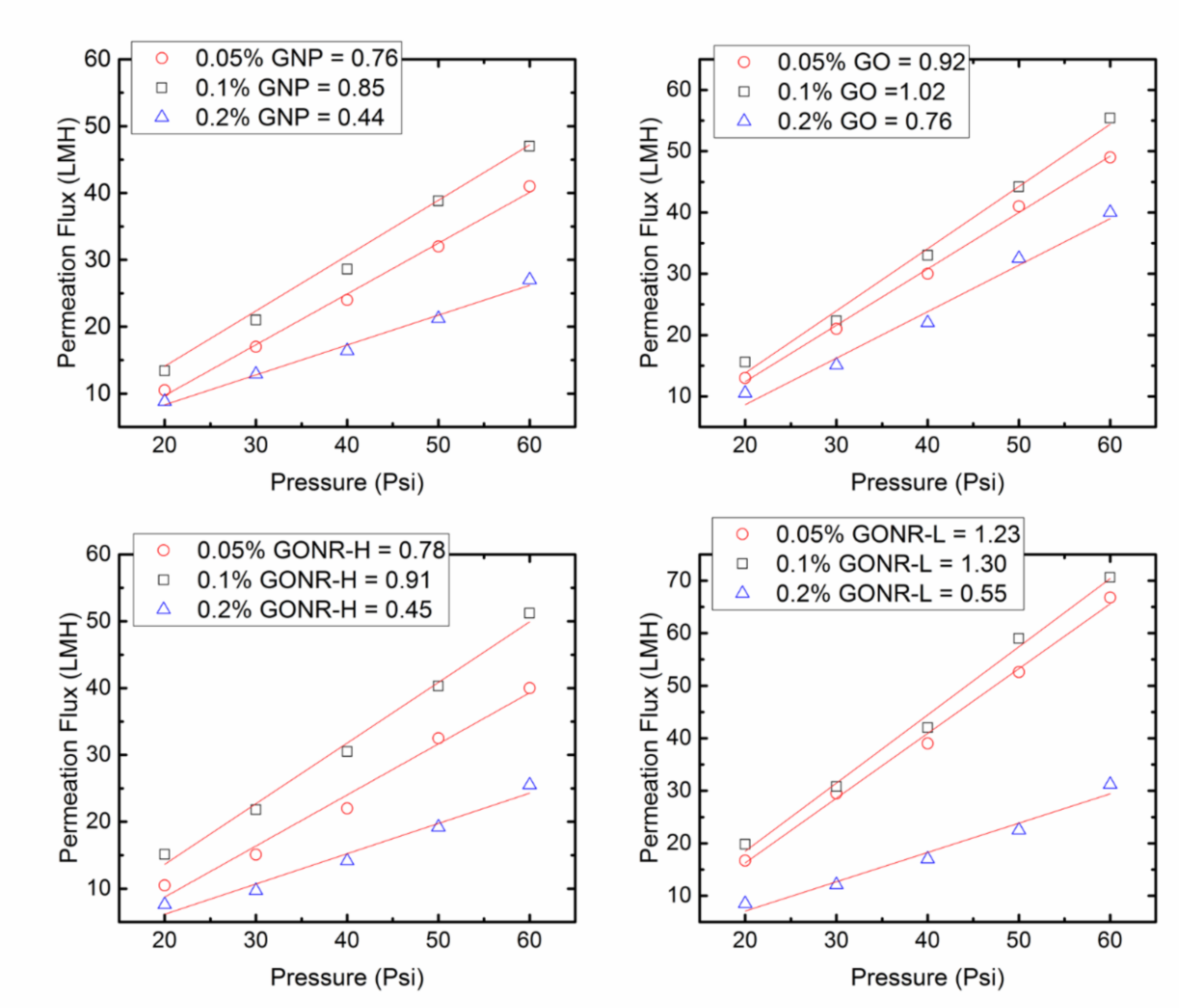

Figure A3. Pure water flux and permeability for different loading of graphene-based nanofillers in PES membranes

A4. Mean pore radius of the membrane as a function of nanofiller concentration

Figure A4 shows that the addition of nanofillers decreased the pore size of membranes. By increasing the nanofiller loading to 0.2 wt.% the mean pore size of membrane reduced significantly from 8.4 nm for pristine PES membrane to 6.2, 6.0, 5.8, and 5.2 nm for GO, GONR-H, GONR-L, and GNP, respectively.

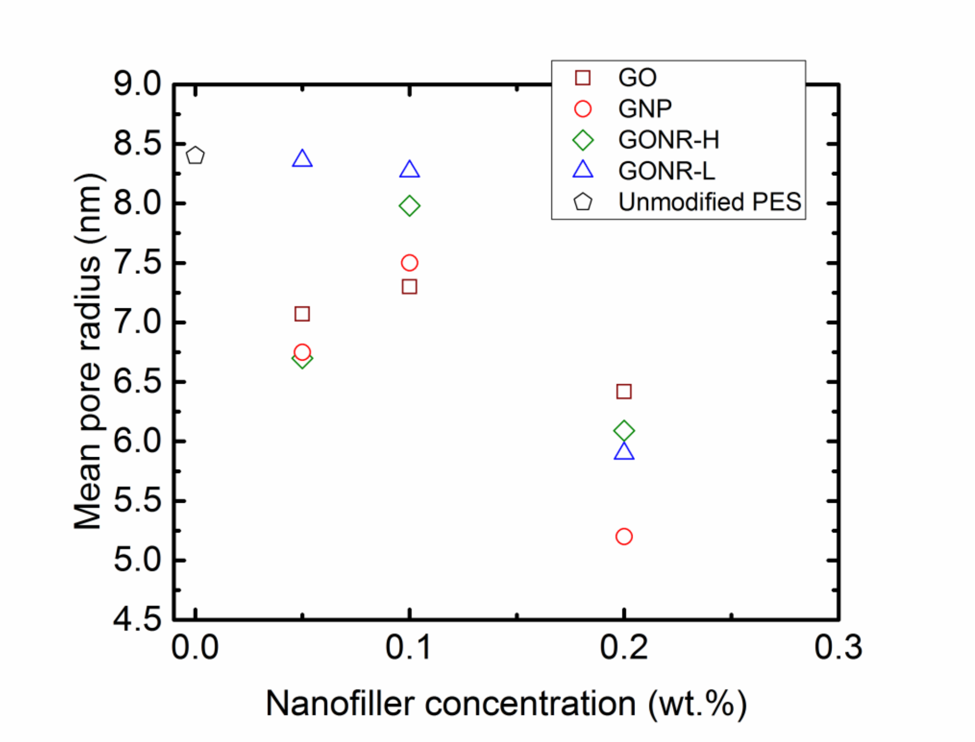

Figure A4. Mean pore radius of membrane as a function of nanofiller concentration

Appendix B

B1. The Process flow diagram of the filtration setup

The setup consists of a stainless steel feed tank, custom-designed membrane cell, a constant flow diaphragm pump, a bypass valve and a back pressure regulator to control applied pressure and cross-flow velocities (Swagelok). A digital weighing balance (Mettler Toledo) was used to measure the permeate flow rate and the data were directly collected in a computer using Mettler Toledo data acquisition software.

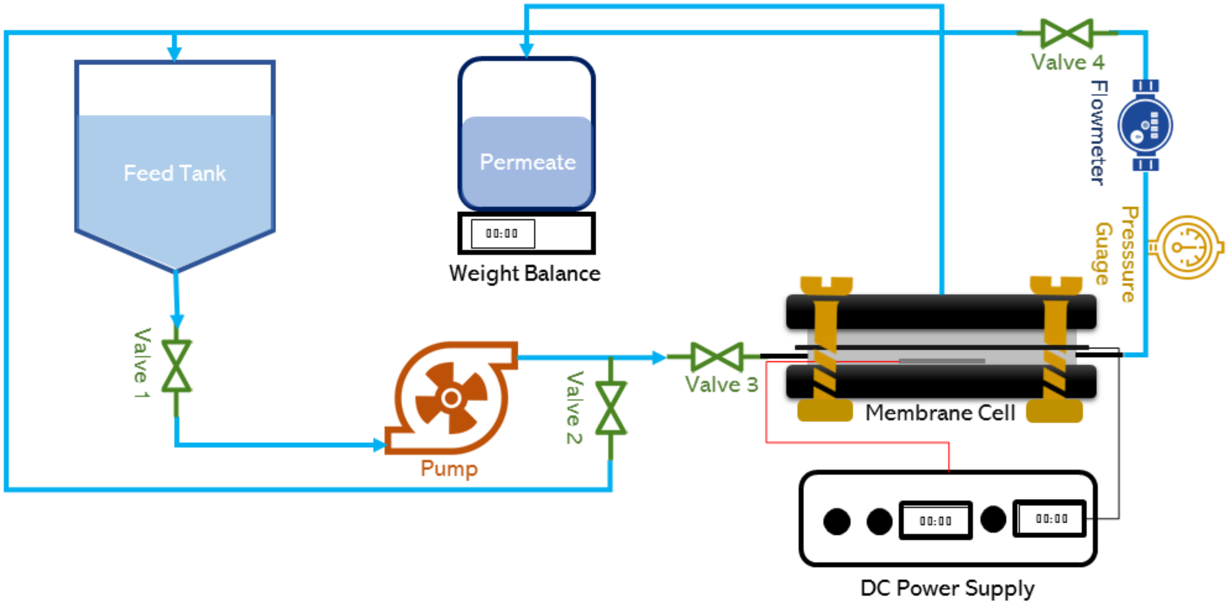

Figure B1. Process flow diagram used for conducting membrane fouling tests

B2. The optical images of the membranes

The optical images of the membranes before leaching tests and after leaching tests. Neither visible defect on the membrane surface nor a change in the turbidity of the aqueous solution was detected for all three membranes, implying that the coated thin films were sufficiently stable under harsh conditions.

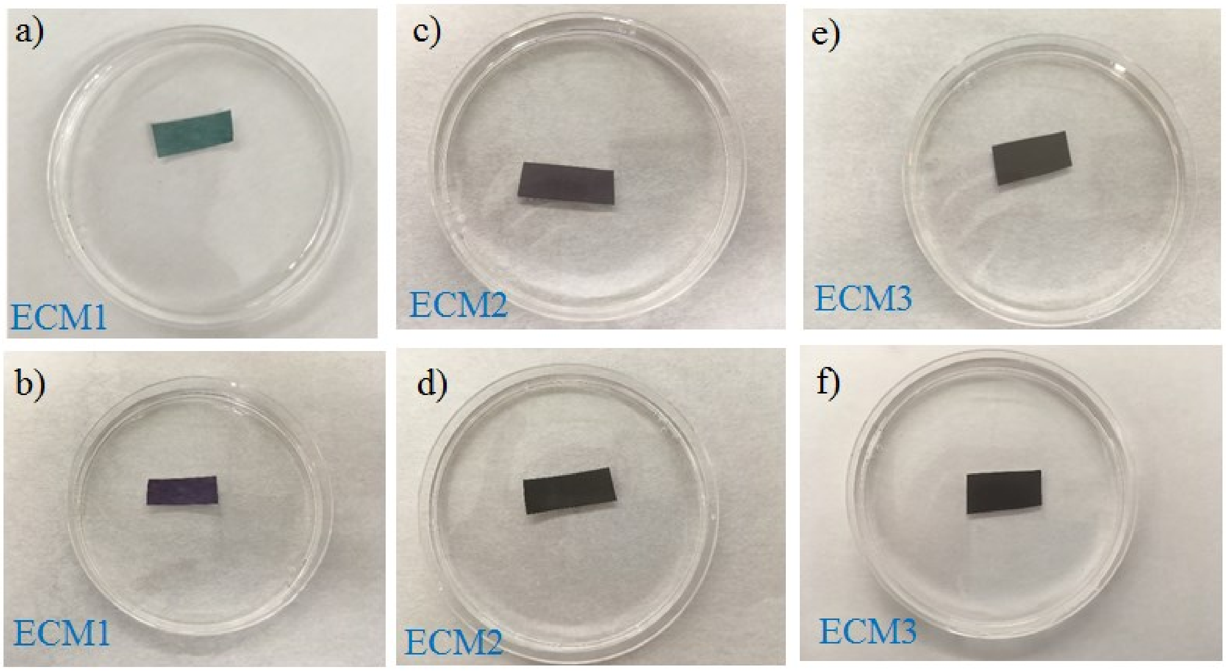

Figure B2. Optical photographs of membranes with surrounding solutions: a), c), e) before and b), d), f) after two weeks immersing in vigorously stirred DI water.

B3. XPS analysis

The characteristic bonding energy of C1s, N1s, and O1s. The atomic percentage of these three elements shows that ECM1 possessed the highest contents of nitrogen and oxygen atoms.

Table B1. Experimental results obtained by XPS analysis.

Membrane	XPS elemental analysis			Deconvoluted N1s		
	C 1S	**N 1S**	**O 1S**	**-NH-**	**=N-**	**$N^{+\bullet}$**
ECM1	73.53	9.28	17.19	84.91	11.00	4.08
ECM2	84.53	5.92	9.56	87.10	8.61	4.29
ECM3	91.88	2.73	5.40	86.06	8.50	5.44